Unique Surface Enhanced Raman Scattering Induced by Plasmon-Nanocavity Coupling and its Application to Elucidating the Mechanism of Enhanced Water Oxidation Under the Strong Coupling Conditions

Thesis by

Xiaoqian Zang

In Partial Fulfillment of the Requirements

for the Degree of

Doctor of Philosophy

GRADUATE SCHOOL OF INFORMATION SCIENCE AND

TECHNOLOGY

HOKKAIDO UNIVERSITY

SAPPORO, JAPAN

2023

Dedication

To my parents and family who gave me my life and strength,

To my friends who accompanied me through the last 30 years,

and to the stories that filled my dreams.

Table of Contents

Acknowledgements

I would like to express my sincere gratitude to all of those who had provided me with their support and assistance during my doctoral journey at Hokkaido University. Without their generous support, this thesis could not be possible.

I am overwhelmed with gratitude as I reflect upon the completion of this journey, and my deepest gratitude goes foremost to my advisor, Professor Hiroaki Misawa, for his unwavering support and guidance. Being an excellent teacher educator as well as a teacher-researcher, in the past six years, it was he who guided me to pinpoint me research focus and inspired me to choose this research topic when I was confused; it was he who helped me solve the problems when my research stalled, it was also he who guide me in making right decisions when I disorientated. His mentorship has been a beacon of light, illuminating my path and infusing my work with depth and purpose. His insightful feedbacks have been instrumental in shaping my research into what it is today.

I am truly appreciative of Prof. Tomoya Oshikiri and Prof. Kosei Ueno for dedicating their time and patience to enrich my learning. Their wealth of insightful discussions, constructive comments, and refined writing skills have not only enriched my current research but will also greatly contribute to my future career. I would like to extend my special gratitude to Prof. Xu Shi for his invaluable support in not only my studies, but also my life in Hokkaido. His extensive knowledge in the field and his guidance on experimental techniques have been instrumental in my research. Despite his busy schedule, he generously assisted me in revising my manuscripts and provided me with a wealth of scientific insights. Prof. Shi has consistently shown kindness and patience whenever I needed assistance, making it a genuine pleasure to study with him.

I am deeply grateful to Ms. Yumiko Yamaguchi for her unwavering support in document preparation throughout my academic journey. Her exceptional patience and meticulous attention to detail have been invaluable to me. Without Ms. Yamaguchi's

dedicated assistance, my experience at Hokkaido University would not have been as enriching, both in terms of my studies and personal life.

I would like to express my great appreciation to all my colleagues and fellow graduates in Misawa Lab. Their assistance, camaraderie, and support have been invaluable to me. I would like to express my sincerest thanks to Ms. Yanfeng Cao for her great help and warm company with my life in both Hokkaido and Shanghai. I would never have enjoyed the first few years of study and life in Hokkaido without her company. I would like to express my thanks to Mr. Yaguang Wang, Mr. En Cao, Mr. Yen-En Liu, and Ms. Xin Fan for their help and company during the difficult time. I would like to express my thanks to Mr. Yoshiki Suganami, Mr. Hiroki Yamada, Mr. Kazuki Furuya, Ms. Azusa Onishi for their kindness help and assistants in my experiment and life. I would like to express my heartfelt appreciation to Mr. Yocefu Hattori for the companionship and encouragement I received during my last year in Hokkaido. His presence illuminated my most challenging year. I will forever cherish every path we tread and every moon we gazed upon during that period. All of them, my colleagues and partners, demonstrated incredible kindness and provided invaluable assistance, not only in my scientific experiments but also in making my life in Hokkaido enjoyable and fulfilling.

To my family, your unyielding support has been my foundation. Your belief in me, even during moments of self-doubt, has pushed me to strive for excellence. Your encouragement and love have been my driving force.

Lastly, I am indebted to Hokkaido University for providing an environment conducive to learning and growth. The resources, facilities, and opportunities offered have been invaluable in the pursuit of my goals.

In closing, I dedicate this accomplishment to the guidance of my advisor and the tireless assistance of the teaching assistants. To all those who have contributed to my academic journey, your impact resonates deeply in my heart, and I am eternally grateful.

Thesis Abstract

Noble metal nanoparticles (NPs) such as gold and silver, are of great interest due to their unique optical, magnetic, and electronic properties based on the plasmon resonance. The localized surface plasmon resonance (LSPR) is the collective oscillation of the conduction band electrons at the surface of metal NPs which induces significant electromagnetic field enhancement at the metal NPs surface. Recently, it has been reported that the modal coupling between an LSPR and a Fabry-Pérot (FP) nanocavity mode can enhance the photochemical reactions taking place near the metal NPs. It is great interesting and critical to investigate the enhancement mechanism of plasmon-induced photoelectrochemical (PEC) reaction under the plasmon-nanocavity coupling. In this thesis, the effect of plasmon-nanocavity coupling on the near-field distribution was investigated by a measure of surface-enhanced Raman scattering (SERS). Besides, the plasmon-nanocavity coupling structure was applied to investigate the plasmon-induced water oxidation reaction, which affected by the plasmon-nanocavity coupling, using *in situ* electrochemical surface-enhanced Raman scattering (EC-SERS) measurements.

A plasmon-nanocavity coupling structure consist of Au NPs/TiO_2/Au-film (ATA) was fabricated to investigate the spatial coherence effect by SERS measurements. Compared to the Au NPs/TiO_2 (AT) structures without FP nanocavity, the SERS signal collected on ATA was enhanced by 11 times because of the dramatic near-field enhancement causing by the coupling between LSPR of Au NPs and FP nanocavity resonance. Besides the large near-field enhancement, a spatially homogeneous near-fi eld intensity was observed on ATA, which can be attributed to the coherent coupling between the LSPR of each Au NP and the FP nanocavity. Simulations also showed the homogeneous near-field distribution under the plasmon-nanocavity coherent coupling, which supports our experiment observations (Chapter 2).

To investigate the effect of plasmon-nanocavity coupling on the plasmon-induced

water oxidation reaction, an Au-Ag alloy NPs/TiO_2/Au-film (AATA) structure was employed, and *in situ* EC-SERS measurements were performed to detect the intermediate species of plasmon-induced water oxidation. The Au-Ag alloy NPs were deposited on TiO_2/Au-film to create a modal strong coupling between the LSPR of Au-Ag alloy NPs and the FP nanocavity resonance. A large splitting energy was observed on the AATA structure which was derived from the large oscillator strength of the LSPR of Au-Ag alloy NPs. The Raman intensity of the Au-O and Au-OH stretching vibrations, which are characterized intermediate species of the plasmon-induced water oxidation on Au-based NPs, were systematically studied at a wide range of electrochemical potentials. Compared with Au-Ag alloy NPs/TiO_2 (AAT) structure without FP nanocavity, the *in situ* EC-SERS measurement of the intermediate species on AATA electrode showed higher sensitivity. More interestingly, the Raman signals on AATA showed a more negative onset potential than the AAT structures, indicating a much more efficient charge separation on AATA structures that facilitates water oxidation reaction. This enhanced water oxidation efficiency on AATA is likely attributed to the quantum coherence between the Au-Ag alloy NPs through the nanocavity, leading to the accumulation of a large number of holes (Chapter 3).

In summary, the near-field intensity distribution, and the water oxidation reaction intermediate on the plasmon-nanocavity coherent coupling structure were investigated by means of SERS measurements. The SERS measurements revealed a large near-fi eld enhancement and spatially homogeneous near- fi eld distribution under the plasmon-nanocavity coherent coupling. Furthermore, the intermediates of plasmon-induced water oxidation were investigated using the plasmon-nanocavity coherent coupling structure by *in situ* EC-SERS measurement. From the EC-SERS measurements, a more negative onset potential of the water oxidation intermediates was observed on AATA, which was attributed the higher near-field enhancement and the e ffi cient plasmon-induced charge separation in the coherent aera under the plasmon-nanocavity coherent coupling.

Keywords: localized surface plasmon resonance, Fabry-Pérot nanocavity, coherent coupling, surface-enhanced Raman scattering, near-field enhancement, water oxidation.

Chapter 1 Introduction

1.1 Background and Motivation

To ensure the efficient and sustainable production of the essential resources that we heavily depend on, it is imperative to develop methods that harness energy and resources readily available in nature.[1] Visible-light-driven photoelectrochemistry (PEC) has attracted heightened interest because of the capacity to harvest the solar energy efficiently, which shows promising potential to solve the global energy crisis.[2-5] Certain semiconductors, particularly those wide bandgap oxide semiconductors like TiO_2 (with an energy bandgap of ~3.2 eV), exhibit limited solar energy absorption abilities.[6] Those limitations that cannot efficiently use visible and near-infrared light hinder their performance in various applications. At present, integrating semiconductors with plasmonic metal nanostructures has emerged as a highly effective strategy for addressing these limitations. In recent decades, noble metal nanoparticles (NPs), notably gold (Au) and silver (Ag), have garnered significant interest in the field of PEC reactions. This interest is primarily due to their remarkable optical, electronic, and magnetic properties. Nobel metal NPs, which exhibit localized surface plasmon resonance (LSPR) and allows them to concentrate and enhance the local electromagnetic field, can significantly improve the separation of electrons from holes in semiconductor materials. [7-9] Moreover, these NPs exhibit a wide range of colors in the visible spectrum, which can be probed using LSPR. Among these noble metals, Au and Ag, in particular, exhibit outstanding LSPR characteristics that enhance PEC performance in the visible light range.[10-11] As a result, the combination of plasmonic metal nanostructures with semiconductors enhances their light absorption and photoelectrochemical performance.[12-15] Despite the numerous studies that have explored the photoelectrochemical performance of metal nanostructure-decorated semiconductor systems, the practical PEC efficiency is still

limited because of its poor light harvesting properties, fast charge recombination and low chemical stability. There is still a critical need to extend our understanding of the mechanisms behind these physical phenomena. Thus, offers us a convenient and promising approach to designing cost-effective, efficient, environmentally friendly, and lightweight energy conversion systems.

1.2 Localized Surface Plasmon Resonance (LSPR)

Surface plasmons have garnered considerable attention due to their widespread applications in fields such as light generation, electronics, optical sensing, and biomedicine. Noble metal nanostructures, known for their distinct optical properties, provide effective manipulation and guidance of light at nanometer scales. Plasmonic is intimately connected to the fundamental principles and practical applications of surface plasmon resonance (SPR), which arises from the interaction between electromagnetic radiation and conduction electrons in noble metals. This interaction leading to both localized optical near-field and far-field scattering effects. The utilization of optical properties exhibited by noble metal NPs can be dated back to the ancient times and boasts a remarkable historical background. A striking illustration of this phenomenon is evident in the Lycurgus Cup, an ancient artifact displaying plasmonic effects. When the cup is illuminated from the front or back, the glass shows different colors due to the SPR phenomenon in the Au NPs embedded glass, as illustrated in **Figure 1.1**. Over recent years, significant advancements in nanotechnology have led to fresh insights into controlling diverse properties of nanomaterials, thus enabling the tailoring of their support for surface plasmons, catering to specific applications. As a result of these advancements, the potential for harnessing surface plasmons in modern technologies has expanded considerably, making plasmonic research a promising avenue for future technological innovations.

Figure 1.1 The Lycurgus Cup viewed in reflected (left) and transmitted (right) light.[16]

1.2.1 Basis of LSPR

When a photon of incident light strikes an electrically conducting surface, the surface plasmon resonances (SPRs) could be excited at a certain condition. There are two types of SPRs—propagating surface plasmon polariton (SPP) and localized surface plasmon resonance (LSPR), as shown in **Figure 1.2**. The SPPs are electromagnetic excitations that propagate along the interface between a dielectric and a conductor. This interaction occurs at a specific angle of incidence, enabling a fraction of the light energy to couple with the electrons present in the metal surface layer. The excitation of these electrons induces their collective motion, giving rise to what is known as plasmon. These plasmons are evanescently confined in the perpendicular direction to the interface and propagate parallel to the metal surface.[17] The LSPR on the other hand are non-propagating excitations, which constitutes an optical phenomenon that occurs when a light wave is confined within conductive NPs smaller than the wavelength of light. This unique phenomenon emerges due to the interactions between surface electrons and incident light within a conduction band.

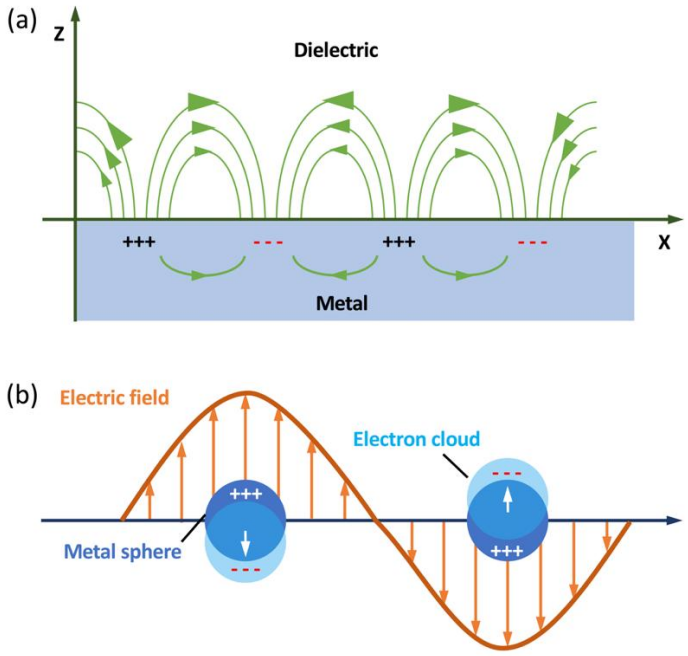

Figure 1.2 Schematic diagrams illustrations of (a) propagating plasmons (SPPs) and (b) a localized surface plasmon (LSPR).

The LSPR effect can be described by employing a simplified model known as the quasi-static approximation, as depicted in **Figure 1.3**.[17]

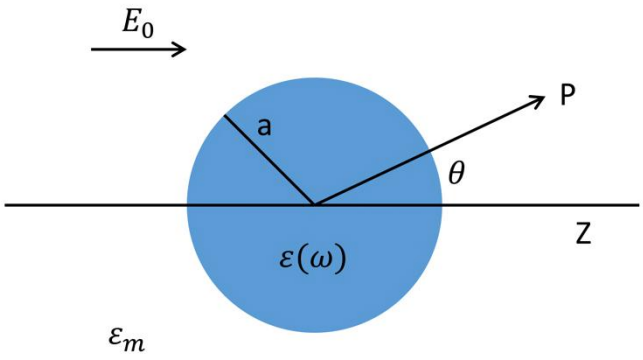

Figure 1.3 Schematic illustrations of mental sphere model into electrostatics field.

In this model, $\varepsilon(\omega)$ represents the dielectric function of the metal sphere; a stands for the radius of the homogeneous sphere; $P_l(\cos\theta)$ corresponds to the Legendre Polynomials of an order of l, and θ is the angle between vector r at point

P_l and the z-axis. In line with the principles of electrostatics, the solution for the Laplace equation ($\nabla^2\Phi = 0$) can be expressed as follows:

$$\Phi(r,\theta) = \sum_{l=0}^{\infty} \left[A_l r^l + B_l r^{-(l+1)}\right] P_l(\cos\theta) \tag{1.1}$$

To ensure that the potentials remain finite at the origin, the solutions for the potentials inside $\Phi_{in}(r,\theta)$ and outside $\Phi_{out}(r,\theta)$ the sphere can be expressed as follows:

$$\Phi_{in}(r,\theta) = \sum_{l=0}^{\infty} A_l r^l P_l(\cos\theta) \tag{1.2}$$

$$\Phi_{out}(r,\theta) = \sum_{l=0}^{\infty} \left[B_l r^l + C_l r^{-(l+1)}\right] P_l(\cos\theta) \tag{1.3}$$

The coefficients A_l, B_l, and C_l can be determined by applying the boundary conditions at $r \to \infty$ and at surface of the sphere $r = a$. When these conditions are applied, it leads to $A_l = C_l = 0$ for $l \neq 1$. Through the calculation of the remaining coefficients A_l and C_l, the potentials are evaluated as follows:

$$\Phi_{in} = -\frac{3\varepsilon_m}{\varepsilon + 2\varepsilon_m} E_0 r\cos\theta \tag{1.4}$$

$$\Phi_{out} = -E_0 r\cos\theta + \frac{\varepsilon - \varepsilon_m}{\varepsilon + 2\varepsilon_m} E_0 a^3 \frac{\cos\theta}{r^2} \tag{1.5}$$

To provide a physical interpretation for equation 1.5: Φ_{out} describes the superposition of the applied field and the field generated by a dipole located at the center of the particle. This can be expressed by rewriting Φ_{out} with the introduction of the dipole moment P as follows:

$$\Phi_{out} = -E_0 r\cos\theta + \frac{P\cdot r}{4\pi\varepsilon_0\varepsilon_m r^3} \tag{1.6}$$

$$\mathrm{P} = 4\pi\varepsilon_0\varepsilon_m a^3 \frac{\varepsilon - \varepsilon_m}{\varepsilon + 2\varepsilon_m} E_0 \tag{1.7}$$

Hence, we observe that the applied field induces a dipole moment within the sphere, and its magnitude is directly proportional to $|E_0|$. To formalize this relationship, we introduce the polarizability α, which is defined as $\mathrm{P} = \varepsilon_0\varepsilon_m\alpha E_0$. We could then obtain the polarizability from the solution equation that:

$$\alpha = 4\pi a^3 \frac{\varepsilon - \varepsilon_m}{\varepsilon + 2\varepsilon_m} \tag{1.8}$$

Consequently, we obtain the Frohlich condition, which signifies the circumstances under which the polarizability experiences a resonant enhancement, as follows:

$$Re[\varepsilon(\omega)] = -2\varepsilon_m \quad (1.9)$$

In this scenario, when metal NPs are treated as electric dipoles, they exhibit a significant influence on the absorption and scattering of incident light. It's important to note that the LSPR frequency of these NPs is inversely related to the dielectric constant of the surrounding medium. This fundamental principle allows for the design of plasmonic systems tailored to achieve specific LSPR frequencies.

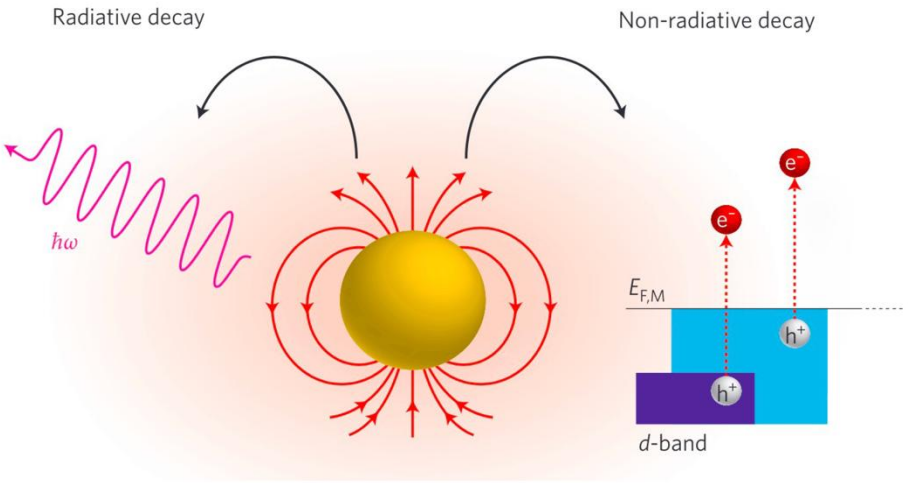

Figure 1.4 Schematic of radiative and non-radiative decay processes for LSPR energy.[18]

The damping processes affecting the LSPR energy of noble metal NPs can be categorized into two main types: radiative and non-radiative processes, as illustrated in **Figure 1.4**.[19]

Radiative Decay (Scattering): This process primarily dominates in larger particles and involves the direct transformation of the plasmonic energy into photons. As particle size increases, this radiative decay or scattering process becomes more prominent. This is why the dipole resonance tends to weaken with larger particle sizes.

Non-Radiative Decay (Landau Damping): This process primarily dominates in smaller particles and results from absorption, which generates electron-hole pairs through Landau damping.[20] The plasmonic energy is rapidly transferred to the "hot carriers" within a timescale ranging from 1 to 100 femtoseconds.[21] During the

absorption process, single-electron states are initially excited by the surface plasmons. There are two channels for electron excitation: intraband transitions within the conduction band and transitions from the d band to the sp band, known as interband excitation. These excited electrons can be elevated above the Fermi level as hot carriers.[22] Understanding these non-radiative decay mechanisms is crucial for various applications of LSPR in noble metal nanoparticles across optical and photoelectric fields. These processes have a significant impact on the efficiency and behavior of plasmonic systems.[23]

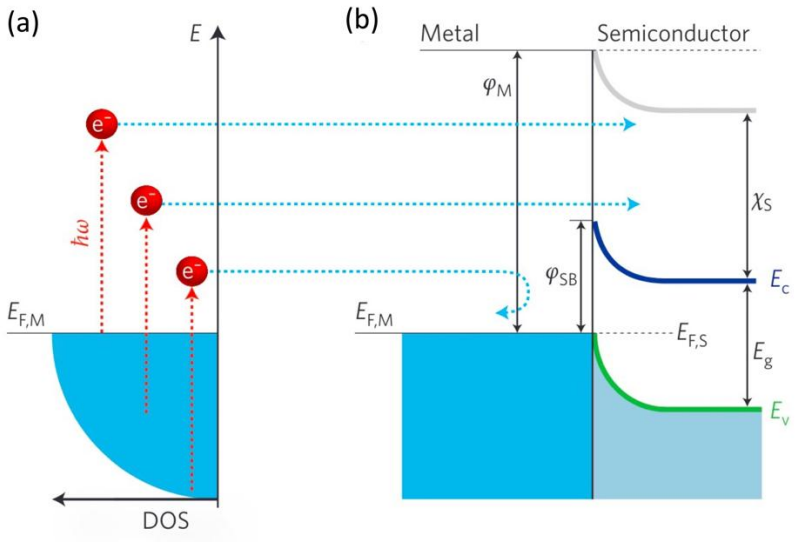

Figure 1.5 (a) Generation of plasmonic hot electrons: electrons on the d-band are excited and come across the Fermi level via a non-radiative process. (b) Injection of hot electrons into the conduction band of semiconductors.[23]

The emission of radiation and non-radiative damping by Landau leads to the creation of high-energy electrons and holes, known as hot electrons and hot holes, respectively. When incident photons with sufficient energy are absorbed by the free electrons within metal nanostructures, these electrons are excited to higher energy levels $E_f + hv$ (**Figure 1.5a**). However, the majority of these high-energy electrons lose their energy rapidly, typically within about 100 fs, due to electron-electron scattering interactions (**Figure 1.5a**). Simultaneously, a small fraction of these

high-energy electrons can be transferred to neighboring species, such as organic molecules or semiconductors (**Figure 1.5b)**. This transfer process is crucial in various applications, as these hot electrons can participate in chemical reactions, drive charge carrier dynamics, or contribute to energy conversion processes.

1.2.2 Fabrication of LSPR Nanostructures

Numerous techniques, such as chemical synthesis and physical preparation, have been investigated to produce noble metal-NPs or nanostructures with diverse sizes and shapes. The fabrication techniques of nanostructures can be categorized into two fundamental methods: top-down and bottom-up methods.[24] The top-down technique is based on physical participation approaches, such as lithography, physical vapor deposition (PVD), and thermal evaporation pyrolysis. The bottom-up technique consists of chemical and biological approaches, where the fine particles are assembled through co-precipitation or self-assembly methods to fabricate the nanomaterials. The chemical vapor deposition (CVD), sol-gel method, chemical co-precipitation, and hydrothermal method pertain to the bottom-up chemical approaches.

Here, some frequently used techniques for creating metal NPs and nanostructures will be introduced in the section.

1. Lithography

In the realm of nanotechnology, lithography draws its fundamental principles from traditional printing lithography but adapts them to the intricate demands of fabricating structures at the nanoscale.[25] In its contemporary application, nanotechnology-oriented lithography entails the meticulous formation of intricate patterns on a substrate, often composed of a thin film of semiconducting materials, like silicon. Typically, this substrate is coated with a light-sensitive substance known as a photoresist. Through precise control of where the photoresist is exposed to light or alternative forms of energy, like electrons or ions, specific patterns can be meticulously crafted. These patterns serve as the foundational elements for a myriad of micro- and nanoscale structures, which find utility across a diverse spectrum of

devices.[26] Various types of lithography are employed for surface patterning, including photolithography,[27-28] UV-lithography,[29-31] electron beam (EB) lithography,[32-36] soft lithography,[37-38] scanning probe lithography,[39-41] and nanosphere lithography (NSL).[42-44]

EB lithography offers meticulous control over size, shape, and spatial distribution, facilitating the creation of highly monodisperse NP populations exceeding 99% due to its exceptional resolution (less than 100 nm).[32] The EB lithography process, as shown in **Figure 1.6**, entails applying an electron-sensitive photoresist, such as poly(methyl methacrylate) (PMMA), onto a glass substrate that supports a conductive film such as indium tin oxide (ITO). Subsequently, an electron beam is deployed to selectively remove the polymer in the desired pattern, followed by chemical development of the exposed surface. For finalization, Au or Ag is deposited via thermal evaporation at a controlled rate of 1–2 nm/s, and then the PMMA is eliminated using acetone, leaving behind the intended pattern.[33]

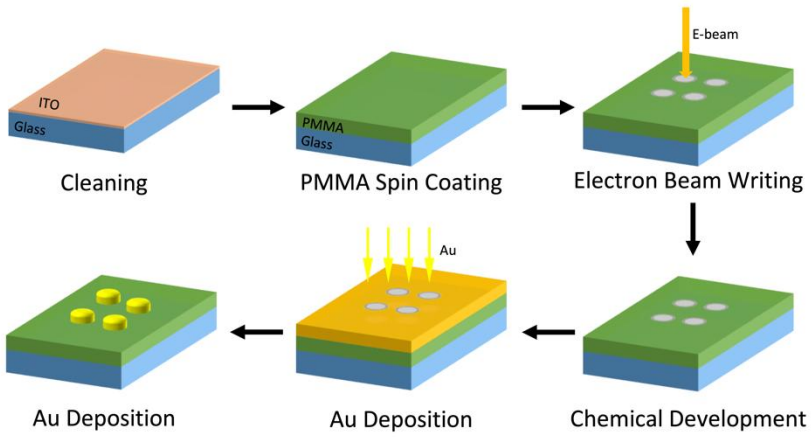

Figure 1.6 EB lithography technique used to fabricate Au nanostructures on an ITO glass substrate.

NSL technique stands out because of its cost-effective, yielding 2D periodic arrays and metal films-over-nanosphere (FON) structures. FON structure, renowned for its substantial roughness, serves as remarkably effective substrates for surface-enhanced

Raman spectroscopy (SERS). The NSL process, depicted in **Figure 1.7**, relies on the self-assembly of polymer nanospheres that are arranged in a tightly compressed hexagonal pattern. This assembly is subsequently coated with a metal layer.[45] Following the removal of the mask, the metal deposited with a thickness ranging from 15 to 100 nm generates honeycomb lattices comprising triangular islands. The size of these islands can be fine-tuned by adjusting the gap size of the spheres. [46]

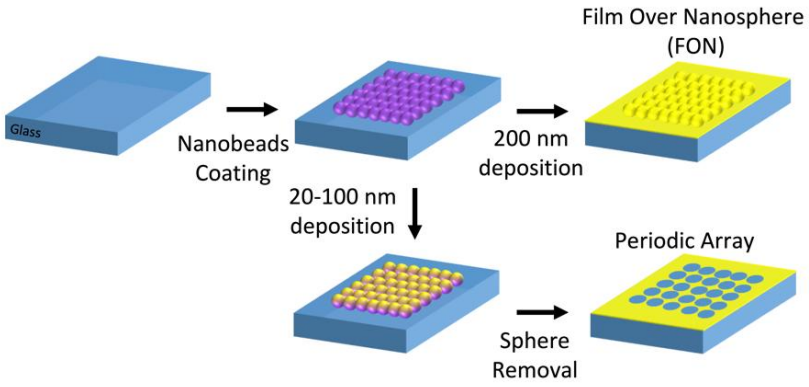

Figure 1.7 NSL lithography technique used to generate FON with 200 nm thickness Au deposition and NP arrays with 20–100 nm Au deposition.

2. Physical vapor deposition (PVD)

PVD is a method employed in the creation of extremely thin films and surface coatings. As shown in the **Figure 1.8**, the PVD technique involves generating metal vapor that is subsequently deposited onto a conductive layer as ultra-thin films and alloy coatings. The entire process is conducted within a vacuum environment, maintained at a pressure of about 10^{-6} torr, within a vacuum chamber featuring a cathodic-arc source. In an air-free setting, vacuum deposition occurs within the chamber, resulting in the deposition of metals over a specific area through either condensation or sputtering.[47-49] The PVD method encompasses both evaporation and sputtering procedures for thin film fabrication. This includes a sputtering process where the vapor phase is maintained under supersaturation conditions. Within an inert atmosphere, metal vapors are encouraged to condense, subsequently undergoing

thermal treatment to yield nanocomposites.[50] The PVD techniques offer several advantages, including: (i) enhanced properties relative to the substrate material; (ii) utilization of primarily inorganic and some organic materials, rendering it an environmentally friendly alternative compared to electroplating methods.[51-52]

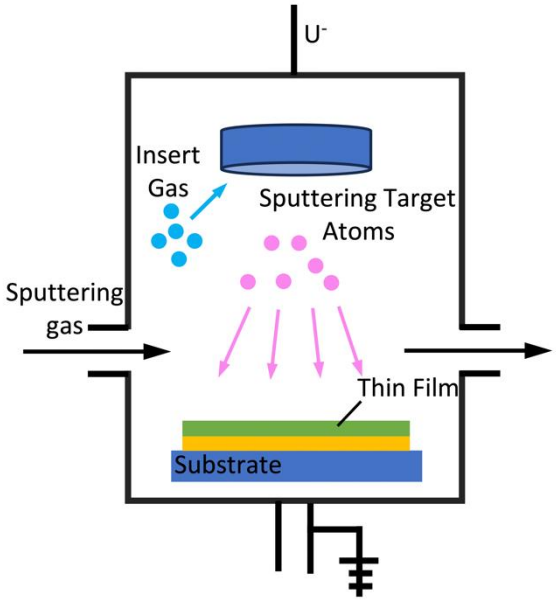

Figure 1.8 A schematic illustration of physical vapor deposition (PVD) process.

3. Chemical Vapor Deposition Method (CVD)

CVD technique emerges as a vacuum-based deposition technique employed to yield solid materials of superior quality and enhanced performance.[53] As shown in the **Figure 1.9**, this approach involves the deposition of thin films onto a substrate, engaging in chemical reactions among various species, including organometallic and other gases.[54] Notably, CVD possesses a distinctive feature that it employs a multidirectional deposition approach for coating substrates, diverging from the line-of-sight impingement method of PVD.[55] CVD finds widespread use in depositing materials in diverse forms such as amorphous, crystalline, and epitaxial growth within microfabrication processes.[56] In CVD, a mixture of gases engages in chemical interactions across the surface of bulk materials, leading to chemical decomposition and the creation of a dense coating on the material's surface.[57] The advantages of the

CVD process encompass the generation of high-purity thin films and the creation of abrupt junctions. However, drawbacks encompass the dependence of the final product on precursor properties and issues regarding uniformity.[53]

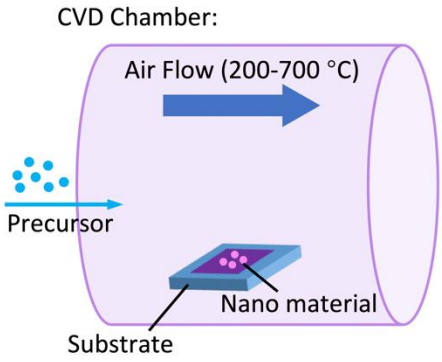

Figure 1.9 A schematic illustration of chemical vapor deposition (CVD) process.

4. Sol-Gel Method

The sol-gel method stands as a widely employed approach for NP fabrication, involving condensation and hydrolysis reactions. During the NP fabrication process, depicted in **Figure 1.10,** an intermediate synthesis step incorporates heat treatment, crucial for achieving nanoparticle crystallinity.[58] Oxide NPs are derived from alkoxides, serving as precursors. These alkoxides interact via molecular forces, such as van der Waals forces or hydrogen bonding, and are dispersed within a sol through processes like evaporation or condensation.[59] The alkoxide precursor undergoes hydrolysis in the presence of either a base or an acid, leading to the formation of a polymeric gel. The end product characteristics are governed by the kinetics of both condensation and hydrolysis reactions.[60] An illustrative instance is that the hydrolysis rate diminishes as the size of nanoparticles reduces. This method aptly produces oxides, composites, and ceramic nanoparticles with a homogenous distribution of high purity.[61-62] The sol-gel method boasts high purity, yielding a smooth nanostructure under the influence of a capping agent ligand and at low temperatures. Nonetheless, a key drawback lies in the heightened presence of impurities stemming from reaction by-products, necessitating post-treatment.[63]

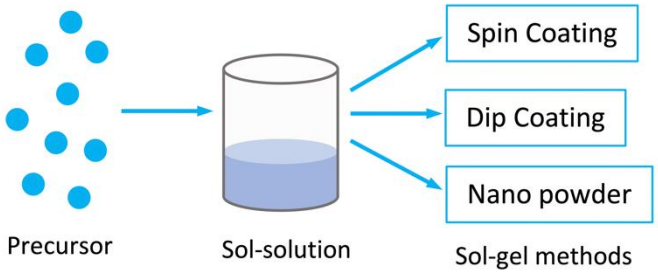

Figure 1.10 Schematic of different stages of sol-gel process: from precursor to aerogel.

1.2.3 Applications of LSPR

1. LSPR Spectroscopy

LSPR spectroscopy in metal NPs is a potent technique for conducting biological sensing and chemical experiments and has significant applications in various areas particularly in enhancing the sensitivity of surface-enhanced techniques, such as surface-enhanced Raman scattering (SERS) and surface-enhanced fluorescence (SEF).[64]

SERS is a powerful analytical technique for sensing trace molecules in the field of biochemical and chemical analytics.[65] When plasmonic NPs are excited at their LSPR frequency, strong localized electromagnetic fields near the NPs surfaces generated, which can substantially enhance the Raman signal of nearby molecules.[66-67] By precisely tuning the LSPR wavelength of nanoparticles to match the excitation laser, SERS can provide ultrasensitive and label-free detection of molecules, even at low concentrations.[68] For instance, W. Lee and his team outlined a procedure of fabricating SERS substrates through the self-assembly of Au NPs, guided by a chemically-modified PS-b-P4VP block copolymer template. The plasmon resonances of the substrate were adjusted by controlling the size of the anchored nanospheres. The SERS substrate enhancement factor was optimized for a specific input laser.[69] As shown in **Figure 1.11**, SERS intensity observed from the substrate with a 7-minute overgrowth period was the highest. This could be attributed to the fact that the

wavelength of the LSPR peak closely matched both the incident light wavelength and the Stokes Raman shift of 4-aminobenzenethiol, resulting in enhanced SERS signal intensity.[70]

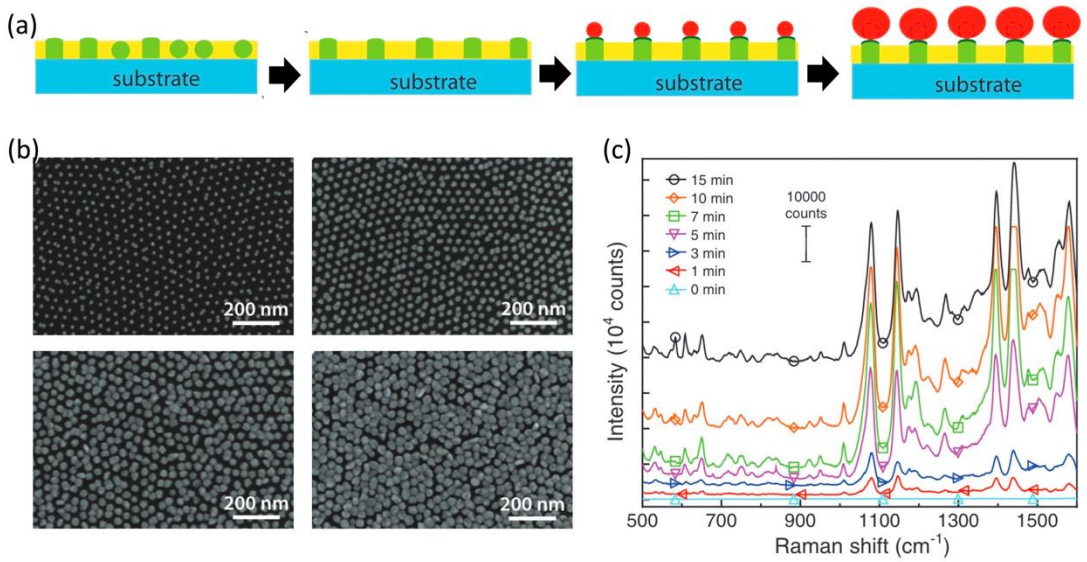

Figure 1.11 (a) Schematic diagrams illustrating the procedures used to fabricate a block copolymer-assisted SERS substrate. (b) SEM images of gold nanoparticle arrays prepared with different overgrowth times of 1, 3, 7, or 15 min. (c) SERS spectra of 4-aminobenzenethiol, obtained from gold nanoparticles with different overgrowth times.[69]

SEF is quickly emerging as a primary spectroscopic technique for detecting a wide range of biomolecules and biomarkers.[71] This trend is primarily driven by the exceptional sensitivity, selectivity, durability, and rapid analytical capabilities of SEF technique.[72] LSPR can enhance the fluorescence emission of nearby fluorophores. When fluorophores are placed in the vicinity of plasmonic nanostructures, the enhanced local electromagnetic fields lead to increased fluorescence intensity and improved detection limits. LSPR spectroscopy plays a key role in optimizing the wavelength and intensity of excitation light to maximize SEF effects.[73] For example, Dr. Knoll's research group successfully detected *E. coli* O157:H7 (**Figure 1.12**).[74] They employed a Au surface that had been modified with a mixed thiol self-assembly monolayer of carboxylic acid terminated thiol and Poly(ethylene) glycol thiol as a

substrate and measured by using the long-range SEF spectroscopy. They have achieved a detection limit below 10 CFU/ml, the detection time of 40 minutes, and the analyte concentration range from 10 to 10^6 CFU/ml. Overall, their work highlighted the capabilities of this innovative biosensor, showcasing a 3~4 orders of magnitude lower detection limit and a higher specificity for the detection of specific strains of *E. coli* bacteria, compare with other methods.

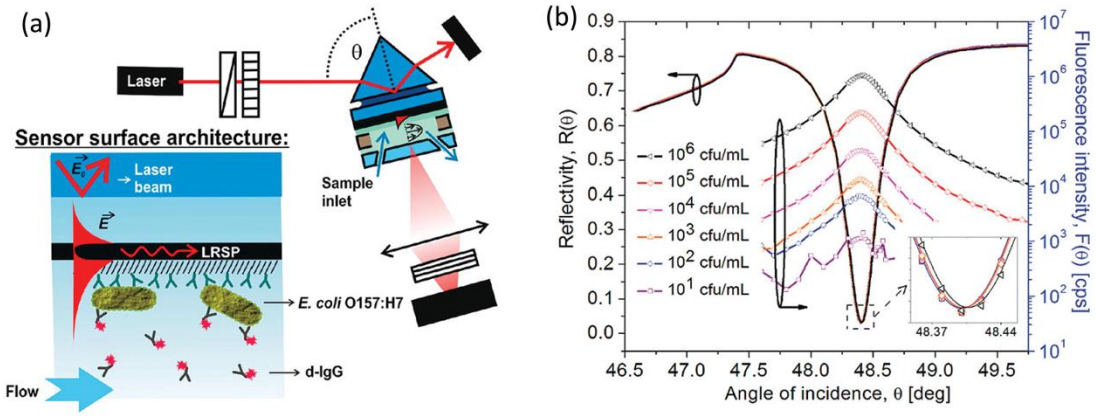

Figure 1.12 (a) Optical setup of a LRSP-SFS biosensor, surface architecture, and detection assay. (b) The angular reflectivity (left axis) and fluorescence (right axis) spectra measured after the analysis of *E. coli* O157:H7 at the concentrations between $10^1$and 10^6 CFU/mL (curves clearly indicated in the graph).[74]

LSPR spectroscopy serves as the foundation for surface-enhanced techniques like SERS, SEF, and MEF. It's ability to enhance the interaction between matters and light at the nanoscale has revolutionized analytical chemistry, enabling highly sensitive and specific detection of molecules and biomolecules. These techniques find applications in fields such as materials science, biology, and environmental monitoring.

2. Photovoltaic devices

The remarkable light-trapping and electromagnetic field-concentrating characteristics of surface plasmons have paved the way for diverse applications in the realm of plasmonic.[75] LSPR can occur in meticulously engineered nanostructures and generate powerful, extremely enhanced electromagnetic fields. Consequently, such

nanostructures have garnered attention as effective light-trapping elements, which can be seamlessly integrated into photovoltaic cells to substantially enhance the efficiency of conventional designs,[76] such as organic solar cells,[77] silicon solar cells,[78] dye-sensitized solar cells (DSSC),[79] Perovskite Solar Cells,[80] and so on.

Researchers for example Spyropoulos et al. and collaborators have shown that the addition of surfactant-free Au NPs in the active layer of organic photovoltaic (OPV) devices can significantly increase the device performance by up to 40%, thanks to the LSPR and scattering effects, as shown in **Figure 1.13**. It has been determined that the spectral range in which there is an increase in photon-to-electron conversion efficiency (IPCE) aligns with the theoretically predicted extinction spectrums of Au NPs present in the active medium. The results imply that the LSPR effect is the primary reason for the efficiency increase.[81]

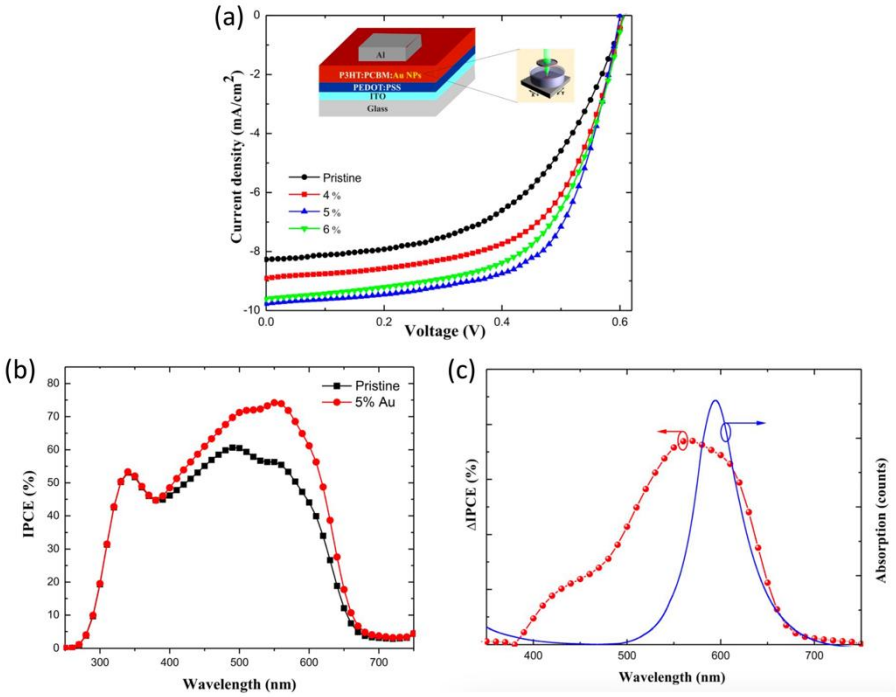

Figure 1.13 (a) J-V characteristics of the OPV devices with Au NPs embedded in the active layer. (b) Corresponding IPCE curves of these OPV devices. (c) Comparison between the curve of the increase in IPCE after incorporating Au NPs and the calculated extinction spectrum of the Au NPs.[81]

3. Photoelectrochemical water splitting

The integration of plasmonic nanostructures with nanostructured photoactive semiconductors has proven highly advantageous in the context of photoelectrochemical water splitting.[82-83] Plasmon-enhanced photoelectrochemical water splitting was first experimentally proposed by Yoko et al. in 1996.[84] This phenomenon arises due to LSPR, which occurs within nanostructures at a specific wavelength determined by their geometry, metal composition, and surrounding dielectric environment. Additionally, the LSPR induces several beneficial effects, such as hot carrier generation and near-field enhancement, which can greatly improve charge generation and transfer processes during the photoelectrochemical water splitting reaction. This distinctive behavior is absent in bulk metals and underscores the advantages of using nanostructured metals. notably, recent theoretical studies have indicated that plasmons have the potential to surpass the maximum classical theoretical efficiency for water splitting.[85]

TiO_2 has emerged as a highly appealing semiconductor material for PEC water splitting over the past few decades. This is primarily resulted from the strong interaction between the noble metals and TiO_2, resulting in a phenomenon known as LSPR that enhances light absorption properties of the TiO_2, extending the range from the ultraviolet to the visible light region.[86-87] Recent studies have demonstrated the effectiveness of plasmonic metal NPs, such as Au and Ag, in enhancing the PEC water splitting capabilities of TiO_2.

For example, Zhang et al. investigated a TiO_2/Au photoanode for PEC water splitting reaction, as is shown in **Figure 1.14**. Their results indicated that the LSPR effect of Au NPs significantly increased the PEC activity of TiO_2, especially in the visible light region.[88] The achievement can be attributed to the strategic alignment of the LSPR wavelength of Au NPs with the photonic band gap of the photonic crystal layer. This alignment enhances the intensity of the LSPR significantly, leading to a substantial improvement in PEC performance.

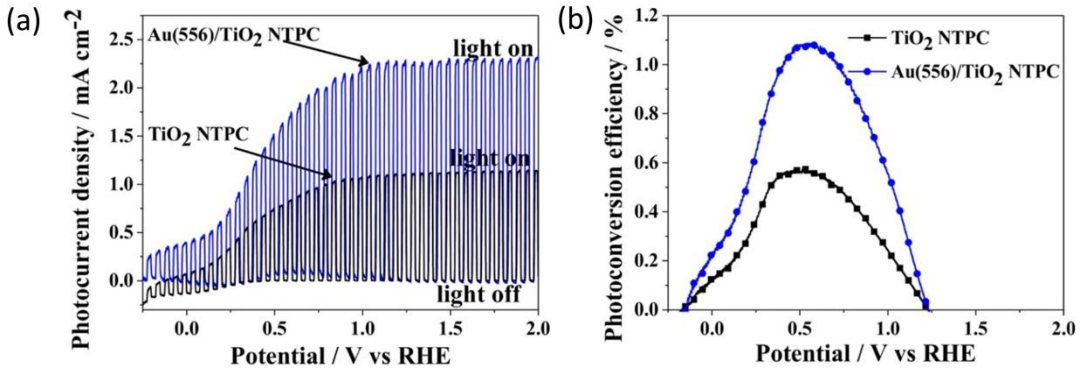

Figure 1.14 (a) PEC performance of the TiO2 nanotube photonic crystal (TiO_2 NTPC) and Au/TiO_2 NTPC under entire solar light irradiation: (a) linear-sweep voltammograms under chopped illumination, collected with a scan rate of 5 mV/s; (b) photoconversion efficiency as a function of applied potential.[88]

Singh et al. reported on a TiO_2 photoanode supported by plasmonic Ag NPs, as shown in **Figure 1.15**. In this investigation, effective plasmon-induced hot-electron production and subsequent transfer have been witnessed in a solution processing system encompassing the real-time development of an Ag-TiO_2 thin films. This innovative approach has been successfully employed to enhance the production of solar H_2. This study revealed that this configuration exhibited a substantially higher photo response in the visible light spectrum compared to a pristine TiO_2 electrode for PEC water splitting, owing to the LSPR effect of the Ag NPs.[89]

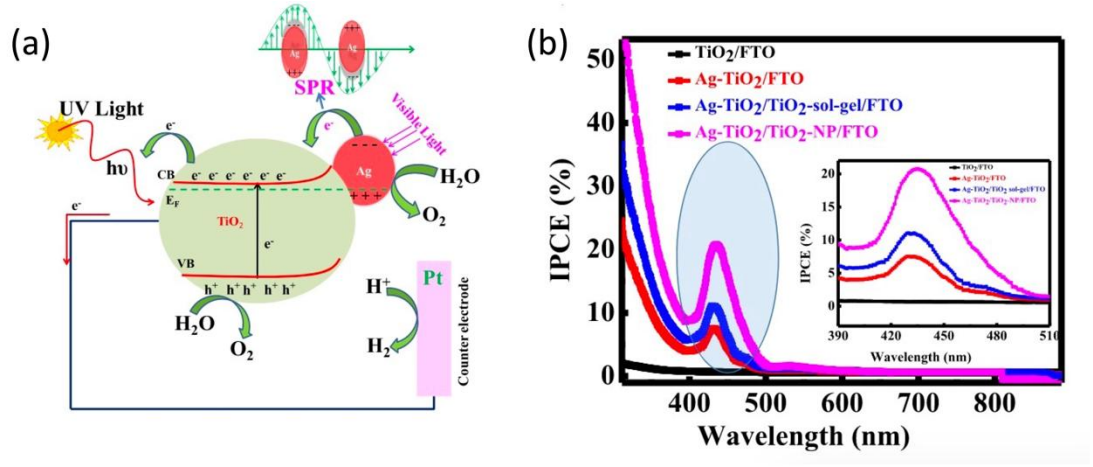

Figure 1.15 (a) Schematic diagram of the PEC water splitting mechanism by the Ag-TiO_2-based

photoanode due to the LSPR effect of Ag NPs. (b) IPCE data for different photoanodes in the range of 350 ~ 800 nm under −1.0 V external bias with 1 mol/L KOH electrolyte solution. The inset shows the magnified IPCE data in the wavelength range of 390 ~ 510 nm.[89]

1.3 Modal Strong Coupling

Plasmonic photocatalysis has received considerable attention over the past few decades due to the attractive plasmonic enhancement effects in improving the visible light absorption. However, the light-harvesting capability of a single layer of metal NPs remains limited. To enhance the light harvesting efficiency of metal nanostructures, considerable attention has been directed towards the utilization of advanced nanofabrication technologies. [90-94] This has led to the exploration of coupled plasmon systems characterized by tunable spectra and intensified near-fields, aimed at achieving improved performance. Among these strategies, the utilization of plasmonic in metal nanostructures be coupled with optical modes, for instance, waveguide and cavity, [95-99] have demonstrated remarkable effectiveness in achieving efficient light absorption. Notably, this approach has been recently extended to applications involving photocurrent generation and water splitting.[100-101]

The development of a strong coupling system between the LSPR of metal NPs and an optical cavity has been devised to achieve a highly responsive and adaptable optical behavior.[102-103] These optical nanocavities consist of a thin absorber layer (approximately several tens of nanometers in thickness) positioned atop a transparent spacer layer, with a highly reflective layer situated at the rear. When specific conditions are met, particularly for a specific wavelength, the thicknesses of these layers can be chosen to achieve optical impedance matching. This leads to complete elimination of overall reflectance through the destructive interference of partially reflected waves. With rearward transmission being obstructed, virtually all incident light is directed into the absorber layer.[104-109] Such nanocavities possess the capability to sustain an antisymmetric FP resonance. This resonance is characterized by being

spectrally broadband and relatively insensitive to variations in the angle of incidence.[104-105] This strategy shows great potential in integrating plasmonic nanostructures with FP nanocavities, resulting in plasmonic photocatalysis systems with substantial and extensive absorption capabilities.[102-103]

For example, Yinsheng Guo and the coworkers[103] experimentally investigated the sandwich structure, which consist of Au NPs/TiO_2/Ag-film, can harvest light across a broad wavelength range with highly efficient to achieve a signal enhancement of the limited Raman photons. (**Figure 1.14**).

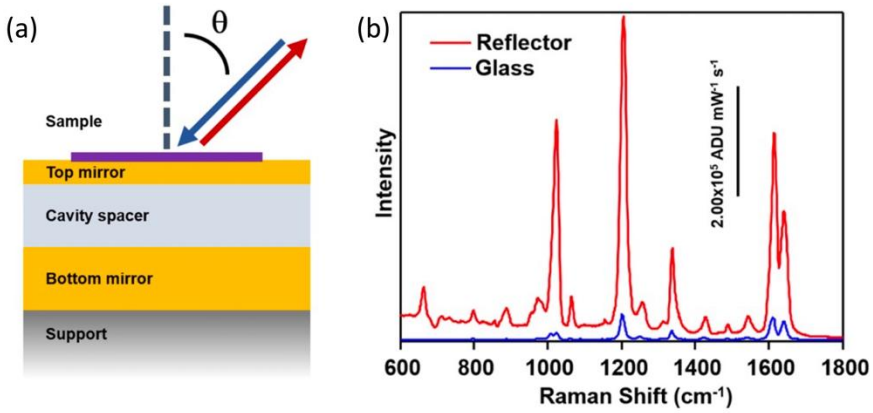

Figure 1.14 (a) Schematic of the F-P cavity substrate. The F-P cavity is fabricated by depositing stacks of thin films on a flat solid support. The bottom mirror is fully reflective, with its thickness larger than the optical skin depth. The cavity spacer is made of a transparent dielectric material of predetermined thickness. The top mirror is semitransparent for coupling the cavity mode to the incidence and scattered light. Sample molecules are deposited onto the top mirror just outside of the F-P cavity. Raman excitation laser is focused onto the sample surface at an angle θ. Collection of Raman scattered light is done using the same focusing optics at the identical angle θ. (b) Experimental observation of the enhanced Raman scattering of BPE. The enhancement factor (EF) on the F-P cavity substrate was typically ~12 times larger than on glass, bringing the overall EF into the 10^9 regime.

In the previously mentioned Au NPs/TiO_2/Ag-film nanostructures, Au NPs are placed on the surface of the TiO_2 film, contributing to a weak interaction between the

LSPR and cavity mode. To overcome the limitation, our research group exploited an Au NPs/TiO_2/Au-film nanostructure that capitalizes on the modal strong coupling between LSPR of Au NPs and FP nanocavity within TiO_2/Au-film to achieve efficient broad-spectrum light absorption and enhance the water splitting reaction (**Figure 1.15**). To reinforce the interaction between the LSPR and FP nanocavity, Au NPs are partially embedded within an additional thin TiO_2 film. This structural design enables the absorption of over 98% of visible light and significantly improves the IPCE compared to structures without any strong couplings.

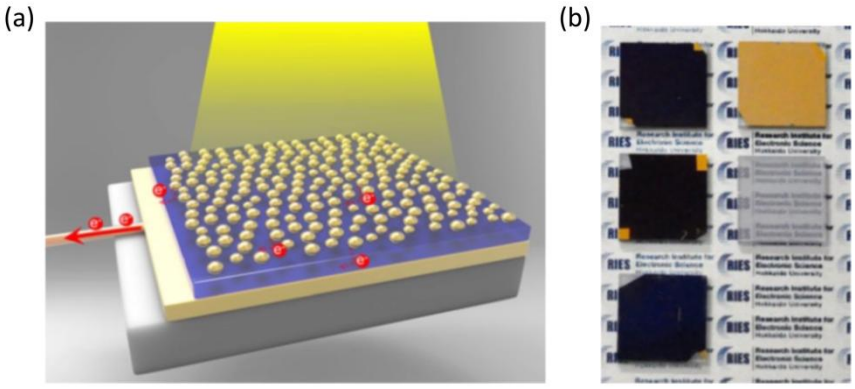

Figure 1.15 (a) Schematic and (b) Photographs of Au NP/TiO_2/Au-film (ATA) with partially inlaid Au NPs.[85]

The coupled harmonic oscillator model,[111-112] usually employed to illustrate the fundamental principle of strong coupling between a nanocavity modes and an emitter, could be utilized to compute the energy separation of those plasmon and cavity systems. When applied to the coupled LSPR-cavity system, the strength of field coupling in the LSPR is linked to both the dipole moment of LSPR and the cavity electric field. This system can be represented by the Hamiltonian equation as follows:

$$\begin{pmatrix} E_c & \frac{\hbar\Omega}{2} \\ \frac{\hbar\Omega^*}{2} & E_p \end{pmatrix} \tag{1.10}$$

where E_p is the resonance energy of the LSPR, and E_C is resonance energy of the the cavity mode. $\hbar\Omega$, which determines the energy splitting of an observed resonance, is a potential describing the strength of the coupling between the two oscillators.

We excluded the consideration of cross-damping terms, which factor in the incoherent transfer of energy between the subsystems that are not coupled. The solution to the equation is as follows:

$$H\psi = \begin{pmatrix} E_c & \frac{\hbar\Omega}{2} \\ \frac{\hbar\Omega^*}{2} & E_p \end{pmatrix} \begin{pmatrix} \psi_c \\ \psi_p \end{pmatrix} = E \begin{pmatrix} \psi_c \\ \psi_p \end{pmatrix} \tag{1.11}$$

The polariton's eigenstate, which composed of the eigenstates of the LSPR and the cavity, results in the dispersing of the coupled system:

$$E_{\pm}(\delta) = \frac{E_C + E_P}{2} \pm \frac{1}{2}\sqrt{(E_C - E_P)^2 + |\hbar\Omega|^2} \tag{1.12}$$

When $E_C = E_P$, the coupling system will lead to the mode splitting of $\hbar\Omega$, as shown in **Figure 1.16**.

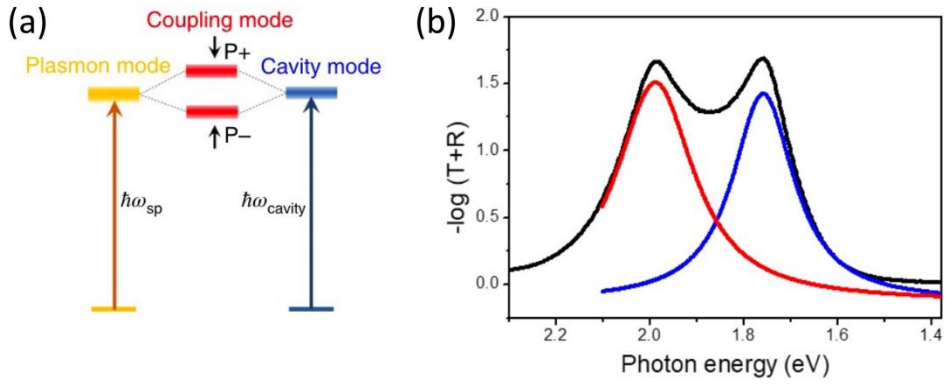

Figure 1.16 (a) Energy-level diagram of the strong coupling between the cavity mode in the TiO_2 film and the plasmon resonance of the Au NPs. The ω_{sp} and ω_{cavity} are the resonant frequencies of plasmon and FP nanocavity modes, respectively. (b) A representative absorption spectrum of the Au -NP/TiO_2/Au-film structure with an inlaid depth of 7 nm and its spectral separation by a Lorentz fitting.

Moreover, the conditions of the strong coupling, as determined by the splitting energy and the linewidth, can be depicted as follows:

$$\hbar\Omega > \sqrt{\frac{\gamma_{UB}^2 + \gamma_{LB}^2}{2}} = \sqrt{\frac{\gamma_{caviy}^2 + \gamma_{LSPR}^2}{2}} \tag{1.13}$$

where $\hbar\Omega$ is the splitting energy. γ_{UB} and γ_{LB} are the linewidths of the upper and

lower branches, respectively. γ_{cavity} and γ_{LSPR} are the linewidths of the nanocavity and LSPR modes, respectively.[85] For example, **Figure 1.16b** exhibits the absorption spectrum of the Au NPs/TiO_2/Au-film structure with the Au NPs inlaid of 7 nm, the separation of which is determined by a Lorentz fit. In this context, the values γ_{UB} and γ_{LB} in **Figure 1.16b** are calculated to be 0.20 eV and 0.16 eV, respectively. Consequently, the calculation of $\sqrt{\frac{\gamma_{UB}^2+\gamma_{LB}^2}{2}}$ yields 0.18 eV, which is found to be smaller than the splitting energy of 0.22 eV. This result validates that the Au NPs/TiO_2/Au-film structure examined in this study indeed meets the criteria for strong coupling conditions.[85]

Hence, to advance the creation of efficient plasmonic photocatalysis systems integrating nanocavity and LSPR modes for enhanced visible light performance, Equation 1.6 can be utilized to assess whether the structures satisfy the criteria for strong coupling.

Recently, there have been significant advancements and breakthroughs in the field of strong coupling. Researchers have been particularly focused on achieving strong coupling between optical cavities and emerging materials like semiconductors[113-117], two-dimensional materials[118], and quantum dots[119]. These investigations have led to exciting applications, such as resonance-enhanced Raman and infrared spectra, the development of nanolayers, and the enhancement of cavity-based sensing technologies. Moreover, the field holds great potential for the future development of quantum information and quantum optical devices, making it an area of intense interest and exploration.

1.4 Outlook of this Thesis

In this thesis, the monodispersed metal NPs decorated on TiO_2/Au-film have been applied to investigate the effect of the coherent coupling between nanocavity and LSPR on the near-field distribution. Moreover, the plasmon-nanocavity coupling structure have been regulated by means of controlling the NPs component, NPs size

and film thickness, to apply to investigate the effect of LSPR-nanocavity coupling on the plasmon-induced water oxidation reactions using *in situ* electrochemical surface-enhanced Raman scattering (EC-SERS) measurements. Those studies will provide valuable insights into the exploitation of the plasmon-induced photochemical reactions with high efficiency, contributing to advancements in renewable energy technologies.

This doctoral thesis consists of four distinct chapters. In Chapter 1, an overview is provided, encompassing the fundamentals and practical applications of surface plasmon resonance, along with an exploration of the associated plasmon-induced charge separation process. Chapter 2 mainly narrated the investigation of the spatial coherence effect on the near-field distribution by SERS measurements under the plasmon-nanocavity coupling condition. The SERS spectra of the crystal violet (CV) decorated plasmon-nanocavity structure at series of CV concentrations are explored. And the spatial homogeneity of the near-field intensity is investigated through SERS mapping. Chapter 3 mainly narrated the study of the impact of LSPR-nanocavity coupling on the plasmon-induced water oxidation reactions by *in situ* EC-SERS measurements. A LSPR-nanocavity coupling structure consist of Au-Ag alloy NPs/TiO_2/Au-film (AATA) was regulated and employed to investigate the intermediates of plasmon-induced water oxidation. The intensities of the SERS signals of ν(Au-O) and ν(Au-OH), which represent the reaction intermediate species of water oxidation, were methodically examined over a wide-ranging electrochemical potential. Chapter 4 serves as the concluding section of this thesis. It summarizes the key findings and insights presented throughout the research, discusses their implications within the broader context of the study, and offers a comprehensive conclusion based on the outcomes of the investigations conducted.

1.5 Reference

[1] Dincer, *Renewable and Sustainable Energy Reviews* **2000**, 4, 157.

[2] D. M. Schultz, T. P. Yoon, *Science* **2014**, 343, 1239176.

[3] Horváth, Z. Valicsek, M. A. Fodor, M. M. Major, M. Imran, G. Grampp, A. Wankmüller, *Coordination Chemistry Reviews* **2016**, 325, 59.

[4] Dandia, P. Saini, R. Sharma, V. Parewa, *Current Research in Green and Sustainable Chemistry* **2020**, 3, 100031.

[5] B. Djurišić, Y. He, A. M. C. Ng, *APL Materials* **2020**, 8, 030903.

[6] R. Zha, R. Nadimicherla, X. Guo, J. *Mater. Chem. A* **2015**, 3, 6565.

[7] Boerigter, U. Aslam, S. Linic, *ACS Nano* **2016**, 10, 6108.

[8] S. Li, P. Miao, Y. Zhang, J. Wu, B. Zhang, Y. Du, X. Han, J. Sun, P. Xu, *Advanced Materials* **2021**, 33, 2000086.

[9] S. Linic, U. Aslam, C. Boerigter, M. Morabito, *Nature Mater* **2015**, 14, 567.

[10] Peng, W. Wang, W. Zhang, Y. Liang, L. Zhuo, *Applied Surface Science* **2017**, 420, 286.

[11] Y.-C. Pu, G. Wang, K.-D. Chang, Y. Ling, Y.-K. Lin, B. C. Fitzmorris, C.-M. Liu, X. Lu, Y. Tong, J. Z. Zhang, Y.-J. Hsu, Y. Li, *Nano Lett.* **2013**, 13, 3817.

[12] W. Hou, S. B. Cronin, *Adv. Funct. Mater.* **2013**, 23, 1612.

[13] Zhang, F. Jia, Z. Li, X. Huang, G. Lu, *Nano Res.* **2020**, 13, 3183.

[14] S. W. Lee, *TRECHEM* **2023**, 5, 561.

[15] M. Kim, M. Lin, J. Son, H. Xu, J.-M. Nam, *Advanced Optical Materials* **2017**, 5, 1700004.

[16] https://www.amusingplanet.com/2016/12/lycurgus-cup-piece-of-ancient-roman.html

[17] Maier, S. A., *Plasmonics: Fundamentals and Applications. Springer: New York* **2007**.

[18] C. Clavero, *Nature Photon* **2014**, 8, 95.

[19] M. Thangamuthu, T. V. Raziman, O. J. F. Martin,; J. Tang, Review-Origin and Promotional Effects of Plasmonics in Photocatalysis. *Journal of The Electrochemical Society,* **2022**, 169, 036512.

[20] X. Li, D.Xiao, Z. Zhang, Landau Damping of Quantum Plasmons in Metal Nanostructures. *New Journal of Physics,* **2013**, 15, 023011.

[21] M. L. Brongersma, N. J. Halas, P. Nordlander, Plasmon-Induced Hot Carrier Science and Technology. *Nat Nanotechnol,* **2015**, 10, 25-34.

[22] Wang, N. A. Melosh, Plasmonic Energy Collection through Hot Carrier Extraction. *Nano Lett,* **2011**, 11, 5426-5430.

[23] C. Jian, J. Zhang, W. He, X. Ma, Au-Al Intermetallic Compounds: A Series of More Efficient Lspr Materials for Hot Carriers-Based Applications Than Noble Metal Au. *Nano Energy,* **2021**, 82, 105763.

[24] C. Daraio, S. Jin, in Nanotechnology for Biology and Medicine, ed. by Gabriel A. Silva, Vladimir Parpura, *Springer New York, New York, NY,* **2012**, pp. 27–44.

[25] 1 S. Kim, H. Sojoudi, H. Zhao, D. Mariappan, G. H. McKinley, K. K. Gleason, A. J. Hart, *Sci. Adv.* **2016**, 2, e1601660.

[26] 1 A. Pimpin, W. Srituravanich, *EJ* **2012**, 16, 37.

[27] N. Herzer, S. Hoeppener, U. S. Schubert, *Chem. Commun.* **2010**, 46, 5634.

[28] Revzin, R. J. Russell, V. K. Yadavalli, W.-G. Koh, C. Deister, D. D. Hile, M. B. Mellott, M. V. Pishko, *Langmuir* **2001**, 17, 5440.

[29] L. Montelius, B. Heidari, M. Graczyk, I. Maximov, E.-L. Sarwe, T. G. I. Ling, *Microelectronic Engineering* **2000**, 53, 521.

[30] M. Han, W. Lee, S.-K. Lee, S. S. Lee, *Sensors and Actuators A: Physical* **2004**, 111, 14.

[31] W. Bogaerts, V. Wiaux, D. Taillaert, S. Beckx, B. Luyssaert, P. Bienstman, R. Baets, *IEEE Journal of Selected Topics in Quantum Electronics* **2002**, 8, 928.

[32] M. Altissimo, *Biomicrofluidics* **2010**, 4, 026503.

[33] Hutter, J. H. Fendler, *Adv. Mater.* **2004**, 16, 1685.

[34] W. Cao, H. E. Elsayed-Ali, *Materials Letters* **2009**, 63, 2263.

[35] Dial, C. C. Cheng, A. Scherer, *Journal of Vacuum Science & Technology B: Microelectronics and Nanometer Structures Processing, Measurement, and Phenomena* **1998**, 16, 3887.

[36] A. Tseng, K. Chen, C. D. Chen, K. J. Ma, *IEEE Transactions on Electronics Packaging Manufacturing* **2003**, 26, 141.

[37] X.-M. Zhao, Y. Xia, G. M. Whitesides, *Journal of Materials Chemistry* **1997**, 7, 1069.

[38] D. Qin, Y. Xia, G. M. Whitesides, *Nat Protoc* **2010**, 5, 491.

[39] T. Das, J. D. Smith, M. H. Uddin, R. R. Dagastine, *ACS Appl. Mater. Interfaces* **2022**, 14, 19878.

[40] S. Chen, S. Kim, W. Chen, J. Yuan, R. Bashir, J. Lou, A. M. van der Zande, W. P. King, *Nano Lett.* **2019**, 19, 2092.

[41] M. Kaholek, W.-K. Lee, B. LaMattina, K. C. Caster, S. Zauscher, *Nano Lett.* **2004**, 4, 373.

[42] D. S. Ginger, H. Zhang, C. A. Mirkin, *Angewandte Chemie International Edition* **2004**, 43, 30.

[43] Noy, A. E. Miller, J. E. Klare, B. L. Weeks, B. W. Woods, J. J. DeYoreo, *Nano Lett.* **2002**, 2, 109.

[44] Zhang, N. A. Amro, S. Disawal, R. Elghanian, R. Shile, J. Fragala, *Small* **2007**, 3, 81.

[45] P. L. Stiles, J. A. Dieringer, N. C. Shah, R. P. Van Duyne, *Annual Rev. Anal. Chem.* **2008**, 1, 601.

[46] Kosiorek, W. Kandulski, H. Glaczynska, M. Giersig, *Small* **2005**, 1, 439.

[47] S. Fox-Rabinovich, I. S. Gershman, S. Veldhuis, *Nanomaterials* **2020**, 10, 1720.

[48] M. S. El-Eskandarany, S. M. Al-Salem, N. Ali, *Nanomaterials* **2020**, 10, 1826.

[49] A. Venables, G. D. T. Spiller, *in Surface Mobilities on Solid Materials, ed. by Vu Thien Binh, Springer US, Boston, MA,* **1983**, pp. 341–404.

[50] Oluwatosin Abegunde, E. Titilayo Akinlabi, O. Philip Oladijo, S. Akinlabi, A.

Uchenna Ude, *AIMS Materials Science* **2019**, 6, 174.

[51] Knotek, F. Löffler, G. Krämer, *Surface and Coatings Technology* **1993**, 59, 14.

[52] D. M. Mattox, *Metal Finishing* **1999**, 97, 417.

[53] L. Sun, G. Yuan, L. Gao, J. Yang, M. Chhowalla, M. H. Gharahcheshmeh, K. K. Gleason, Y. S. Choi, B. H. Hong, Z. Liu, *Nat Rev Methods Primers* **2021**, 1, 5.

[54] S. E. Koponen, P. G. Gordon, S. T. Barry, *Polyhedron* **2016**, 108, 59.

[55] F. Kara, B. Öztürk, *SR* **2019**, 39, 24.

[56] R. Müller, O. Gelme, J.-P. Scholz, F. Huber, M. Mundszinger, Y. Li, M. Madel, A. Minkow, U. Kaiser, U. Herr, K. Thonke, *Crystal Growth & Design* **2020**, 20, 6170.

[57] L. Mochalov, A. Logunov, A. Kitnis, V. Vorotyntsev, *Plasma Chem Plasma Process* **2020**, 40, 407.

[58] V. Rane, K. Kanny, V. K. Abitha, S. Thomas, *in Synthesis of Inorganic Nanomaterials, Elsevier,* **2018**, pp. 121–139.

[59] M. Oubaha, *in World Scientific Series in Nanoscience and Nanotechnology, World Scientific,* **2019**, Vol. 3, pp. 1–36.

[60] S. H. Hakim, B. H. Shanks, *Chem. Mater.* **2009**, 21, 2027.

[61] A. Rahman, V. Padavettan, *Journal of Nanomaterials* **2012**, 2012, 1.

[62] Gdula, A. Dąbrowski, E. Skwarek, *Adsorption* **2016**, 22, 681.

[63] T. M. Tillotson, A. E. Gash, R. L. Simpson, L. W. Hrubesh, J. H. Satcher, J. F. Poco, *Journal of Non-Crystalline Solids* **2001**, 285, 338.

[64] A. Willets, R. P. Van Duyne, *Annu. Rev. Phys. Chem.* **2007**, 58, 267.

[65] B. Sharma, R. R. Frontiera, A.-I. Henry, E. Ringe, R. P. Van Duyne, *Materials Today* **2012**, 15, 16.

[66] Q. Han, C. Zhang, W. Gao, Z. Han, T. Liu, C. Li, Z. Wang, E. He, H. Zheng, *Sensors and Actuators B: Chemical* **2016**, 231, 609.

[67] Blanco-Formoso, N. Pazos-Perez, R. A. Alvarez-Puebla, *ACS Omega* **2020**, 5, 25485.

[68] W. Li, R. Zamani, P. Rivera Gil, B. Pelaz, M. Ibáñez, D. Cadavid, A. Shavel, R. A.

Alvarez-Puebla, W. J. Parak, J. Arbiol, A. Cabot, *J. Am. Chem. Soc.* **2013**, 135, 7098.

[69] W. Lee, S. Y. Lee, R. M. Briber, O. Rabin, *Adv. Funct. Mater.* **2011**, 21, 3424.

[70] T. Y. Jeon, D. J. Kim, S.-G. Park, S.-H. Kim, D.-H. Kim, *Nano Convergence* **2016**, 3, 18.

[71] E. Fort, S. Grésillon, *J. Phys. D: Appl. Phys.* **2007**, 41, 013001.

[72] R. Lakowicz, C. D. Geddes, I. Gryczynski, J. Malicka, Z. Gryczynski, K. Aslan, J. Lukomska, E. Matveeva, J. Zhang, R. Badugu, J. Huang, *Journal of Fluorescence* **2004**, 14, 425.

[73] Sultangaziyev, R. Bukasov, *Sensing and Bio-Sensing Research* **2020**, 30, 100382.

[74] C.-J. Huang, J. Dostalek, A. Sessitsch, W. Knoll, *Anal. Chem.* **2011**, 83, 674.

[75] H. A. Atwater, *SIGDA Newsl.* **2007**, 37, 1.

[76] J. Mendes, A. Luque, I. Tobías, A. Martí, *Applied Physics Letters* **2009**, 95, 071105.

[77] Yeh, P. Yeh, *Renewable Sustainable Energy Rev.,* **2013**, 21, 421-431.

[78] W. Wang, S. Wu, K. Reinhardt, Y. Lu, S. Chen, *Nano Lett.,* **2010**, 10, 2012-2018.

[79] Qi, X. Dang, P. T. Hammond, A. M. Belcher, *ACS Nano,* **2011**, 5, 7108-7116.

[80] D. W. Zhao, M. Y. Yu, L. L. Zheng, M. Li, S. J. Dai, D. C. Chen, T. C. Lee, D. Q. Yun, *ACS Appl. Energy Mater.,* **2020**, 3, 9568-9575.

[81] G. D. Spyropoulos, M. M. Stylianakis, E. Stratakis, E. Kymakis, *Applied Physics Letters* **2012**, 100, 213904.

[82] C. W. Moon, G. Kim, J. K. Hyun, *J. Mater. Chem. C* **2021**, 9, 1764.

[83] Kristensen, J. K. W. Yang, S. I. Bozhevolnyi, S. Link, P. Nordlander, N. J. Halas, N. A. Mortensen, *Nat Rev Mater* **2016**, 2, 16088.

[84] G. Zhao, H. Kozuka, T. Yoko, *Thin Solid Films* **1996**, 277, 147.

[85] S. K. Cushing, A. D. Bristow, N. Wu, Phys. *Chem. Chem. Phys.* **2015**, 17, 30013.

[86] Ueno, H. Misawa, *NPG Asia Mater* **2013**, 5, e61.

[87] G. Zhao, H. Kozuka, T. Yoko, *Thin Solid Films* **1996**, 277, 147.

[88] Z. Zhang, L. Zhang, M. N. Hedhili, H. Zhang, P. Wang, *Nano Lett.* **2013**, 13, 14.

[89] S. V. Singh, M. P. Kumar, S. Anantharaj, B. Mukherjee, S. Kundu, B. N. Pal, *ACS Appl. Energy Mater.* **2020**, 3, 1821.

[90] C. Ng, J. J. Cadusch, S. Dligatch, A. Roberts, T. J. Davis, P. Mulvaney, D. E. Gómez, *ACS Nano* **2016**, 10, 4704.

[91] K. Hedayati, M. Javaherirahim, B. Mozooni, R. Abdelaziz, A. Tavassolizadeh, V. S. K. Chakravadhanula, V. Zaporojtchenko, T. Strunkus, F. Faupel, M. Elbahri, *Adv. Mater.* **2011**, 23, 5410.

[92] Z. Zhang, L. Zhang, M. N. Hedhili, H. Zhang, P. Wang, *Nano Lett.* **2013**, 13, 14.

[93] Y. Lu, W. Dong, Z. Chen, A. Pors, Z. Wang, S. I. Bozhevolnyi, *Sci Rep* **2016**, 6, 30650.

[94] R. Takakura, T. Oshikiri, K. Ueno, X. Shi, T. Kondo, H. Masuda, H. Misawa, *Green Chem.* **2017**, 19, 2398.

[95] X. Shi, K. Ueno, T. Oshikiri, Q. Sun, K. Sasaki, H. Misawa, *Nat. Nanotechnol.*, **2018**, 13, 953-958.

[96] K. T. Lin, H. L. Chen, Y. S. Lai, C. C. Yu, *Nat. Commun.*, **2014**, 5, 3288-3288.

[97] Y. H. Lu, W. Dong, Z. Chen, A. Pors, Z. L. Wang, S. I. Bozhevolnyi, *Scientific Reports*, **2016**, 6, 30650.

[98] Christ, S. G. Tikhodeev, N. A. Gippius, J. Kuhl, H. Giessen, *Phys. Rev. Lett.*, **2003**, 91, 183901.

[99] Ng, J. J. Cadusch, S. Dligatch, A. Roberts, T. J. Davis, P. Mulvaney, D. E. Gómez, *ACS Nano*, **2016**, 10, 4704-4711.

[100] Ng, J. J. Cadusch, S. Dligatch, A. Roberts, T. J. Davis, P. Mulvaney, D. E. Gómez, *ACS Nano* **2016**, 10, 4704.

[101] Y. Lu, W. Dong, Z. Chen, A. Pors, Z. Wang, S. I. Bozhevolnyi, *Sci Rep* **2016**, 6, 30650.

[102] Y. Guo, S. Jiang, X. Chen, M. Mattei, Jon. A. Dieringer, J. P. Ciraldo, R. P. Van Duyne, *J. Phys. Chem. C* **2018**, 122, 14865.

[103] D. Chanda, K. Shigeta, T. Truong, E. Lui, A. Mihi, M. Schulmerich, P. V. Braun, R. Bhargava, J. A. Rogers, *Nat Commun* **2011**, 2, 479.

[104] C. Wu, B. Neuner, G. Shvets, J. John, A. Milder, B. Zollars, S. Savoy, *Phys. Rev. B* **2011**, 84, 075102.

[105] C. Hägglund, S. P. Apell, Opt. *Express* **2010**, 18, A343.

[106] C. Hägglund, G. Zeltzer, R. Ruiz, I. Thomann, H.-B.-R. Lee, M. L. Brongersma, S. F. Bent, *Nano Lett.* **2013**, 13, 3352.

[107] H. Song, L. Guo, Z. Liu, K. Liu, X. Zeng, D. Ji, N. Zhang, H. Hu, S. Jiang, Q. Gan, *Adv. Mater.* **2014**, 26, 2737.

[108] J. R. Tischler, M. S. Bradley, V. Bulović, *Opt. Lett.* **2006**, 31, 2045.

[109] V. Steenhoff, M. Theuring, M. Vehse, K. Von Maydell, C. Agert, *Advanced Optical Materials* **2015**, 3, 182.

[110] A. Kats, R. Blanchard, P. Genevet, F. Capasso, *Nature Mater* **2013**, 12, 20.

[111] Christ, T. Zentgraf, J. Kuhl, S. G. Tikhodeev, N. A. Gippius, H. Giessen, *Phys. Rev. B* **2004**, 70, 125113.

[112] Christ, S. G. Tikhodeev, N. A. Gippius, J. Kuhl, H. Giessen, *Phys. Rev. Lett.* **2003**, 91, 183901.

[113] F. Vaianella, J. M. Hamm, O. Hess, B. Maes, *ACS Photonics* 2018, 5, 2486.

[114] R. Houdré, *physica status solidi (b*) **2005**, 242, 2167.

[115] Paulillo, J.-M. Manceau, L. H. Li, A. G. Davies, E. H. Linfield, R. Colombelli, *Applied Physics Letters* **2016**, 108, 101101.

[116] Y.-S. Lee, *Opt. Lett., OL* **2016**, 41, 4550.

[117] J.-G. Rousset, B. Piętka, M. Król, R. Mirek, K. Lekenta, J. Szczytko, J. Borysiuk, J. Suffczyński, T. Kazimierczuk, M. Goryca, T. Smoleński, P. Kossacki, M. Nawrocki, W. Pacuski, *Applied Physics Letters* **2015**, 107, 201109.

[118] X. Liu, T. Galfsky, Z. Sun, F. Xia, E. Lin, Y.-H. Lee, S. Kéna-Cohen, V. M. Menon, *Nature Photon* **2015**, 9, 30.

[119] R. Ameling, H. Giessen, *Laser & Photonics Reviews* **2013**, 7, 141.

Chapter 2 Plasmon-Nanocavity Coherent Coupling

2.1 Introduction

The unique LSPR in metal NPs is the collective oscillation of the conduct band electrons on the metal NPs surface which makes the electromagnetic field significantly enhanced, leading to SERS and further surface-enhanced spectroscopic processes.[1-6] Great advances have been made in SERS through the development of various SERS-active substrates, which involve modifications in both nanoparticle materials and geometrical parameters with the purpose of improving the near-fields.[7-15] However, developing a chip for SERS measurement that can achieve significant amplification and homogeneity across larger areas continues to be a formidable challenge.

Based on to the findings presented in chapter 1.3, a significant interaction occurs between the FP nanocavity mode and the LSPR of Au NPs, resulting in a pronounced phenomenon known as strong coupling.[16] This unique strong coupling model leads to a notably enhanced and broadened absorption within the visible light wavelength range.[16-19] Notably, apart from the substantial near-field enhancement, this coupling between LSPR and FP nanocavity resonance, which can coherently interact and organize a coherent area in a finite two-dimensional area nearby the Au NP, is reported to have contributed to spatially homogeneous near-field intensity.[20] The estimated coherence area, equivalent to a 1 μm-diameter area,[16] offers exciting possibilities for achieving high spatial homogeneity in SERS intensity, thereby advancing practical applications in sensing and analytical technologies. Overall, the combination of F-P nanocavities and LSPR in the strong coupling structure holds great promise for achieving highly efficient SERS enhancement and promoting photochemical reactions, offering exciting possibilities for various applications in sensing and renewable energy technologies.

In this chapter, the effect of LSPR-nanocavity coupling on the near-field

distribution was investigated by a measure of SERS. Herein, a novel plasmon-nanocavity coupling structure, consisting of a monolayer Au NPs, a several nanometers TiO_2 thin film and a Au-film (ATA), was developed to amplify the intensity of the SERS signals and achieve spatial homogeneity simultaneously. Crystal violet (CV) dye molecules, which is intensively used as an analyte for Raman measurements especially the single molecule detection,[21-24] adhered on the Au NPs of ATA structures were used to validate the effectiveness of this approach and certify the significant intensity enhancement and spatial homogeneity of the SERS signals. Our findings emphasize the crucial role played by the coherent coupling between the LSPR and FP nanocavity in determining the near-field distribution of the ATA structure. Furthermore, understanding the interplay between plasmon-nanocavity coupling and the spatial distribution of the SERS signals paves the way for designing and fabricating SERS substrates to investigate the effects of LSPR-nanocavity coupling on plasmon-induced water oxidation reactions.

2.2 Experimental Section

2.2.1 Fabrication of Au NPs/TiO_2/Au-film (ATA) Structures

Figure 2.1 shows the fabrication of the ATA structure, which was carried out on a silex glass substrate measuring 10×10×1.0 mm^3. To prepare the substrate, thorough cleaning was performed using an ultrasonic bath with acetone, methanol, and deionized water for 5 minutes each, and then dried with pure nitrogen flow. The next step involved depositing a Au-film layer (~100 nm) on the silex glass substrate by a Helicon sputtering system (ULVAC, MPS-4000C1/HC1), in which a 3-nm titanium adhesion layer was added for better adhesion. Additionally, a titanium layer (3 nm) was introduced onto the Au-film surface for facilitating the subsequent deposition of the TiO_2 thin film. A 30-nm TiO_2 film was then deposited onto the Au-film using the atomic layer deposition system (ALD) (Picosun, SUNALETM R series) at temperature of 300°C. The precursors used for the deposition were titanium

tetrachloride ($TiCl_4$) and water. To complete the ATA structure, a Au thin film, with the thickness of 3 nm, was evaporated onto the TiO_2 film sequentially using an electron-beam (EB) evaporator (EIKO, EB-580) with the deposition rate of 0.1 Å/s. Lastly, the samples were then annealed under a N_2 atmosphere at temperature of 300°C for 2 hours, resulting in the appearance of Au NPs on the surfaces of the TiO_2 film.

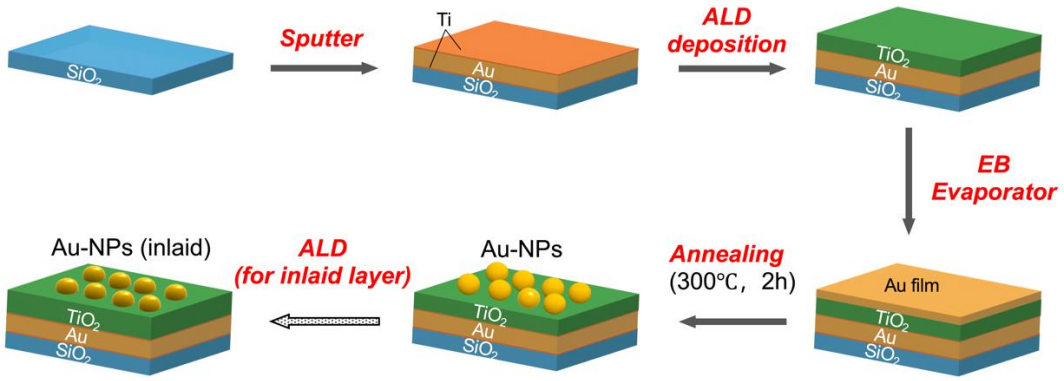

Figure 2.1 (a) Schematic fabrication of ATA structure.

2.2.2 Characterizations

The reflectance (*R*) and transmittance (*T*) spectra were measured using a photonic multichannel analyzer (Hamamatsu Photonics, PMA C7473) assembled with an optical microscope (Olympus, BX-51). To calculate the absorption spectrum as a function of wavelength, the formula 1-*T*-*R* was utilized, in which *T* demonstrate the transmittance and *R* demonstrate the reflectance.

The morphology of the surface was examined using high-resolution scanning electron microscopy (HITACHI, SU-8230) operating with the electron acceleration voltage of 10 kV, providing the maximum resolution of 1 nm.

2.2.3 Raman Measurements

For SERS measurements, the Raman microscope system (Renishaw, inVia Reflex)

equipped with a 50× objective lens (0.75 NA, Leica) was utilized. The wavelength of the excitation source laser is 532 nm. Raman spectra were acquired with a wavenumber range between 200-2000 cm^{-1}, of which the resolution is 1.5 cm^{-1}. The Raman mappings were conducted over the area of 20×20 μm^2 with Raman shift of 1617 cm^{-1}. The laser beam's spots size during mappings was calculated to be about 800 nm. Each mapping comprised a total with 625 measurements, and the exposure time used for all Raman mapping measurements was 0.5 s.

2.2.4 Simulations

The finite-difference time domain (FDTD) simulations were conducted by Lumerical, Inc. software to analyze the far-field spectra, near-field spectra, and the near-field intensity distribution of both the ATA and AT substrates. FDTD simulations were implemented on an incontiguous and homogeneously spaced mesh of which the size is 0.1 nm. The specific FDTD simulation models were created to match the dimensions of the ATA and AT substrates. The optical properties of Au were derived from Johnson and Christy's data.[25] The average refractive index of the TiO_2 was n=2.4, which served as the dielectric material in this study.[26]

The finite element method (FEM) simulations were conducted by the COMSOL Multiphysics software package to analyze near-field enhancement and deviation. The models of Au NPs in the simulations were partially truncated spheres with the radii of 10 and 15 nm, arranged on the surface of TiO_2 substrate and a nanocavity comprising a TiO_2 film with thickness of 30 nm on top of the Au-film. The gap distances between two Au NPs were varied from 2.5 to 30 nm. The simulations were conducted in air with periodic boundary conditions. The mesh size was 0.2 nm. The average refractive index of the TiO_2 was n=2.4, which served as the dielectric material in this study. [26] The enhancement and deviation of the near-field distribution were recorded under a excitation wavelength of 532 nm, which corresponds to the wavelength used for the Raman measurements. To capture the near-field characteristics, a circular ring-shaped near-field monitor, which the diameter is 2 nm larger than the cross-section of the Au

NPs at that plane, was positioned at the interface plane of Au NPs/TiO_2.

2.3 Results and Discussions

2.3.1 Structural Optimizations and Characterizations of ATA

1. Size distribution of the Au NPs

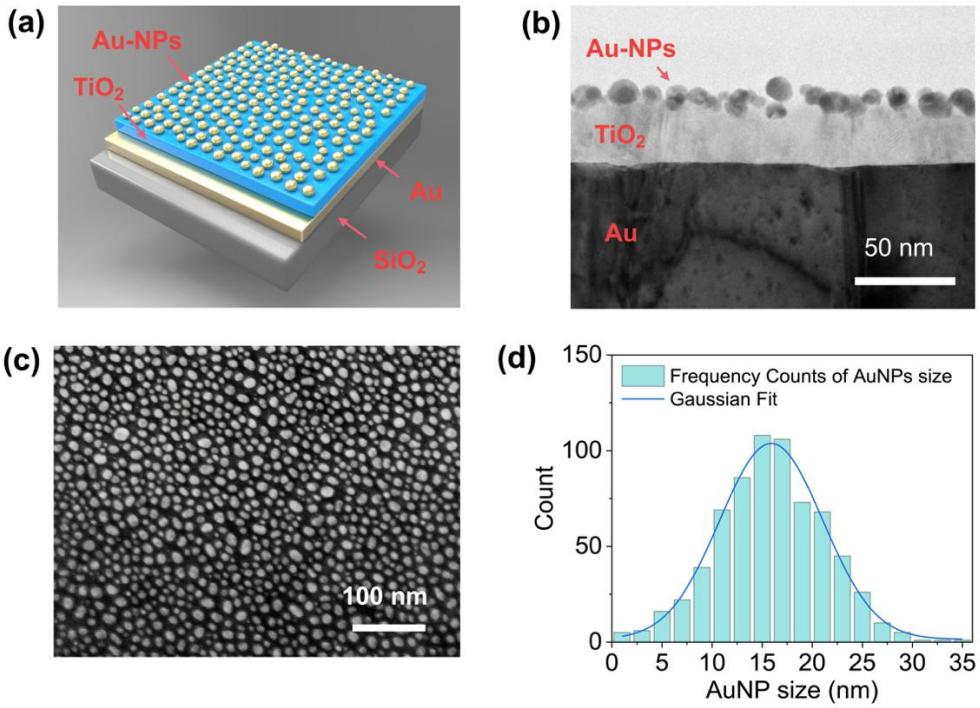

Figure 2.2 (a) Schematic of the ATA structure. (b) cross-section view STEM image of ATA structure, which consist of Au NPs, TiO_2 film (~30 nm) and Au-film. (c) SEM image of Au NPs on the ATA substrate. (d) Particle size distribution histogram and Gaussian fitting of Au NPs from the SEM image.

Figure 2.2a illustrates our SERS substrates, which consist of a single-layer Au NPs fabricated on the TiO_2/Au-film with a nanocavity made. The several tens of nanometers-thick TiO_2 film enables the formation of a cavity mode, with the lowest-order, in visible range of light. This phenomenon was attributed to the phase change of reflected light at the boundary surface of the TiO_2/Au-film and the high refractive index of TiO_2 (~2.4 at 600 nm).[22] **Figure 2.2b,c** presented the cross-section

and top view images of ATA substrate, depicting the surface morphology of the Au NPs and the structure of the ATA. The size distribution histogram of the Au NPs, obtained from the SEM image and its Gaussian fit, are displayed in **Figure 2.2d**. The average size of the Au NPs is 16.0 ± 5.4 nm, and the surface coverage is approximately 31.3%, calculated by dividing the covered area of Au NPs by the entire substrate area.

2. Optimization of the TiO_2 thickness

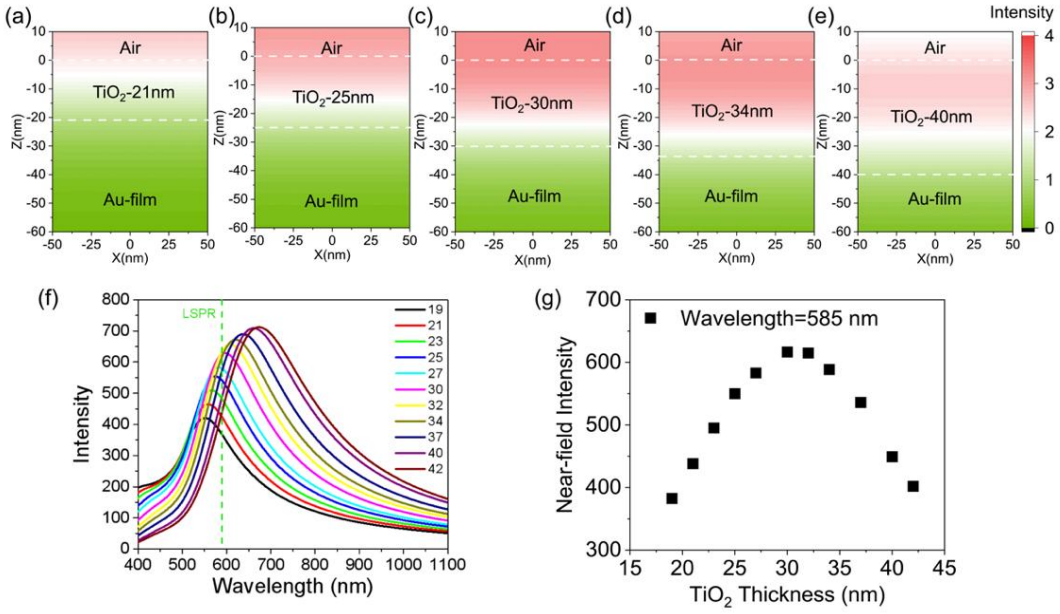

Figure 2.3 FDTD simulation of the electromagnetic near-field of TiO_2/Au-film. (a)-(e) Cross-sectional near-field distributions of TiO_2/Au-film structures at wavelength of 585 nm with TiO_2 thickness of 21, 25, 30, 34 and 40 nm, respectively. (f) Electromagnetic near-field spectra at the surface of TiO_2 with various thickness. The LSPR of Au NPs was marked by the green dash line. (g) Near-field intensity at the LSPR wavelength of 585 nm as a function of TiO_2 thickness.

To achieve an optimal coupling between nanocavity resonance and LSPR, it is essential to ensure that their resonance wavelengths are closely matched. we conducted FDTD simulations to calculate the electromagnetic near-field of TiO_2/Au-film. The cross-section view of the electromagnetic near-field distribution at the LSPR wavelength of 585 nm with various TiO_2 thicknesses is presented in **Figure 2.3a-e**. Remarkably, a enhanced near-field at the TiO_2 surface was observed for the 30-nm TiO_2 thickness. Further analysis of the near-field spectra at TiO_2 surface with

different thicknesses (**Figure 2.3f)** and the plot of near-field intensity at LSPR wavelength as a function of TiO_2 thickness (**Figure 2.3g**) revealed that the TiO_2/Au-film nanocavity substrate with 30 nm TiO_2 exhibits the highest near-field intensity at LSPR wavelength. For this reason, we focused on the ATA with 30 nm TiO_2 for our study.

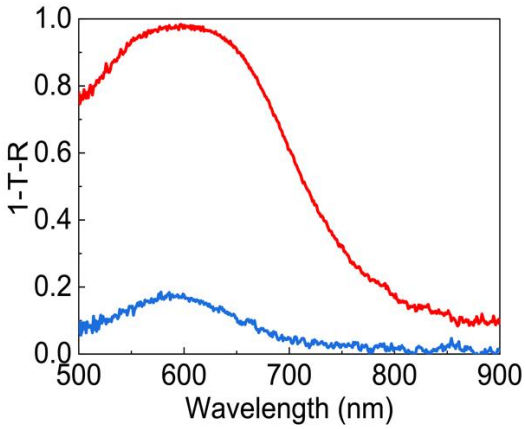

Figure 2.4 Absorption spectra of ATA and AT structures calculated by 1-*T*-*R*. *R* and *T* represent the reflectance and transmittance, respectively.

The AT substrates without FP nanocavities were also fabricated in this work for investigating the impact of the nanocavity mode on light absorption. **Figure 2.4** displays the absorption spectra of both ATA and AT substrates. The absorption spectra were calculated using 1-*T*-*R*, in which *R* and *T* represent the reflectance and transmittance, respectively. On the AT substrates without cavities, a distinct plasmonic band of Au NPs appears at around 585 nm with an absorption of approximately 0.2. In contrast, the ATA sample exhibits a significant enhancement in absorption, nearly reaching 1.0, and a broadened absorption band width. This remarkable increase in absorption efficiency close to the plasmon resonance is because of the coupling between the LSPR of Au NPs and the nanocavity resonance of the TiO_2/Au-film, demonstrating the beneficial effect of the nanocavity structure.

3. Effects of inlaying Au NPs

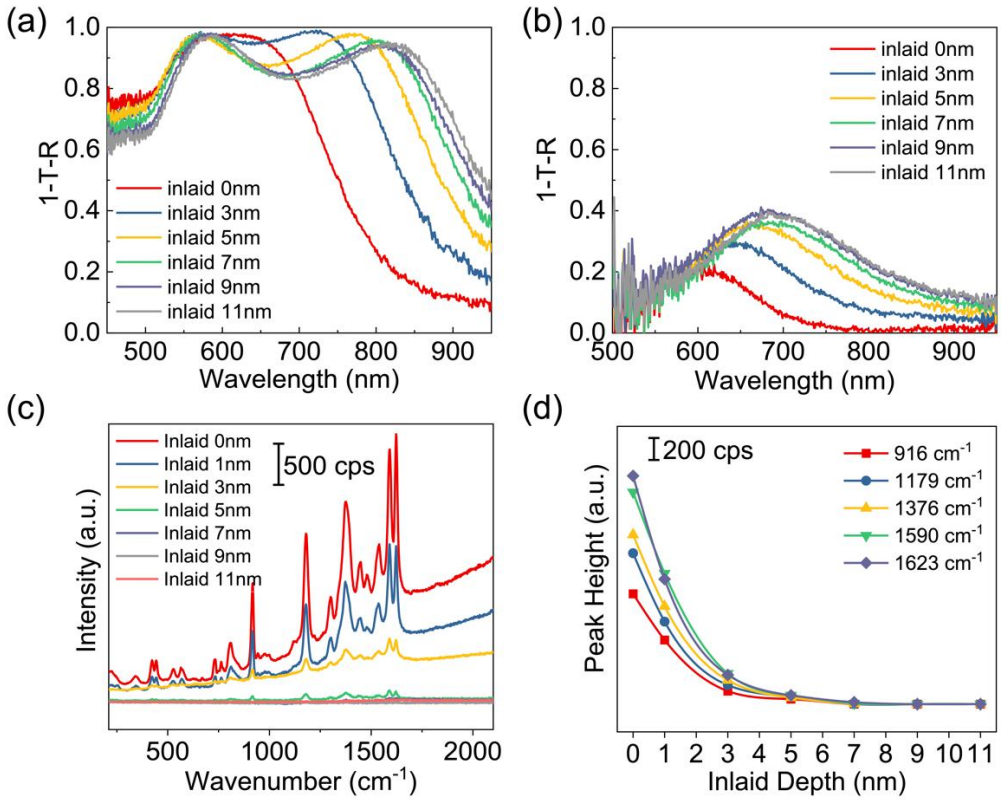

Figure 2.5 (a, b) Absorption spectra, calculated by 1-*T*-*R*, of ATA (a) and AT (b) structures with the inlaid thickness from 0 to 11 nm. (c) SERS spectra of ATA structures with the inlaid thickness from 0 to 11 nm. (d) Raman peak intensity as a function of inlaid depth calculated from the Raman spectra in (c).

In the previous study, we successfully demonstrated a strong coupling between the LSPR of Au NPs and the nanocavity resonance by employing the ATA structure, which the Au NPs was partially inlaid in the TiO_2, resulting in the generation of hybrid states.[17-19] To investigate the impact of partially inlaid Au NPs on the coupling condition and near-field distribution, absorption spectra and SERS spectra of ATA structures with varying inlaid depths were measured and subsequently illustrated in **Figure 2.5**. **Figure 2.5a and b** depict a notable trend where the LSPR bands show a progressive red shift and the absorption divide into two distinct peaks as inlaid depth of Au NPs increases. Intriguingly, as partial inlaid depth of Au NPs is heightened, the bandwidth of the absorption spectra of ATA experiences augmentation. Notably, the absorption spectra with distinct dual-band distinctly appear when the inlaid depth

surpasses 7 nm. Furthermore, a noteworthy observation is made for the ATA configuration featuring 7 nm inlaid Au NPs, where over 99% of incident light is effectively absorbed within the visible light spectrum.

However, the SERS intensity, which can be seen from **Figure 2.5c and d**, exhibits an attenuation trend as the inlaid depth increases. When utilizing the partially inlaid Au NPs, the near field is primarily confined to the surface boundary between nanocavity of the TiO_2 and the Au NPs, resulting in limited presence in the contact surface between the Au NPs and TiO_2. Consequently, when dye molecules are adsorbed on such partially inlaid Au NPs, they cannot enjoy an enhanced near field. This phenomenon was also confirmed by FDTD simulation, as shown in **Figure 2.6**.

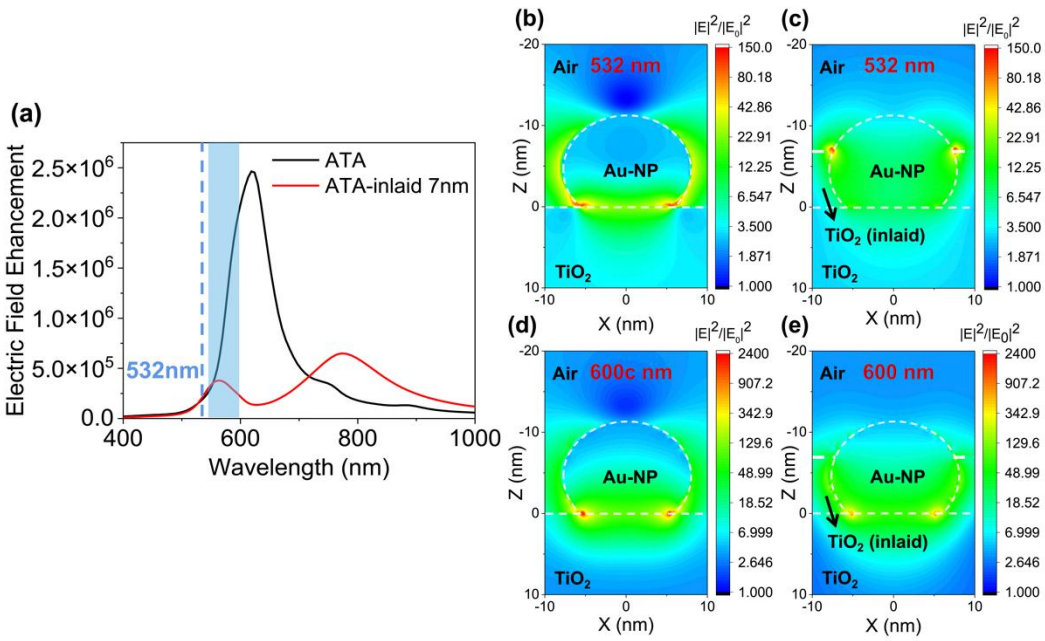

Figure 2.6 (a) Integrated near-field enhancement of ATA and ATA with 7-nm inlaid Au NPs substrates calculated by FDTD simulation. Near-field monitors were set at the interface between air and the TiO_2 film (TiO_2-inlaid film, if present). The wavelength of the excitation laser and Raman scattering wavelength region are indicated by the blue vertical line and green shaded area, respectively. (b-e) show the cross-sectional near-field distributions of ATA and ATA with inlaid Au NPs substrates at wavelengths of 532 nm and 600 nm.

Hence, in this research we introduced the ATA structure without partially inlaid Au

NPs for our coupling-enhanced SERS measurements.

4. Coupling condition between the LSPR and nanocavity resonance

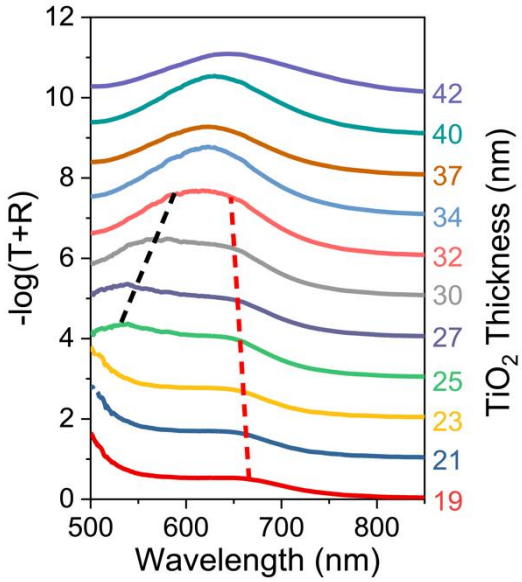

Figure 2.7 Absorption spectra calculated by -log(*T*+*R*) of the ATA structure decorated by CV (10^{-6} mol/L) with various TiO_2 film thicknesses.

In our investigation, we conducted absorption spectrum measurements of ATA decorated with CV under plasmon-nanocavity coupling conditions with varying TiO_2 thicknesses, as depicted in **Figure 2.7**. The obtained absorption spectra exhibited two distinct bands at wavelengths shorter than 700 nm. However, for the thin TiO_2 film with a thickness under 23 nm, the two absorption peaks were not attributed to the model weak or strong coupling between the nanocavity and LSPR. The absorption band below 550 nm could be put down to the cavity-enhanced interband transition of Au, as reported by our previous study.[16]

According to **Figure 2.7**, we did not observe any anti-crossing behavior in the absorption spectra. Although peak-fitting method could separate the spectra into two absorption peaks, these separated peaks did not meet the strong coupling criterion as shown in equation 1.13.[16]

These results suggest that the model coupling of the cavity and LSPR in this study is not in strong coupling regime. Despite exhibiting relatively weak coupling with a small coupling strength, as illustrated in **Figure 2.7**, we can still anticipate coherent

coupling between the FP nanocavity and LSPR due to the presence of the same phase on the cavity.

2.3.2 SERS Enhancement Effect

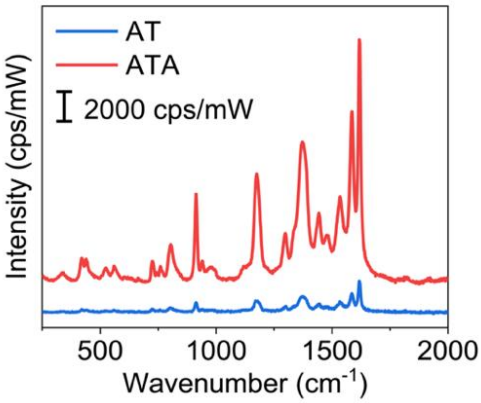

Figure 2.8 Raman spectra of CV (10^{-4} mol/L) at a laser power of 30 μW obtained from the ATA substrate (red line) and AT substrate (blue line).

The SERS performance of the substrates was evaluated using CV molecules, which are known for low fluorescence quantum yield and distinct Raman bands. **Figure 2.8** illustrates the Raman spectra of CV molecules on ATA and AT substrates (without Au-film). Control samples, including TiO_2/Au-film without Au NPs and TiO_2 film substrates, were also assessed (data not shown). To load CV molecules, we immersed the samples in the CV molecules solution with the concentration of 10^{-4} mol/L, then subsequently dried them using an air flow. Without Au NPs, the SERS signals were barely detectable due to the diminutive Raman scattering cross-section of the substrate. In contrast, the SERS spectra of CV on AT substrate displayed distinct Raman peaks, consistent with previous reports.[21,27-28] The Raman bands assignments of CV can be found in **Table 2.1**. Notably, the SERS spectrum on the ATA substrate exhibited an 11-fold enhancement in peak intensity compared to that on the AT substrate, showcasing a significant SERS enhancement effect arising from the weak coupling between the LSPR of Au NPs and the nanocavity resonance.

Table 2.1. Assignments of Raman bands of CV in SERS.

Raman shift (cm^{-1})	Wavelength (nm)	Band assignment
337	542	C-phenyl in-plane bending vibration
441	545	Phenyl-C-phenyl out-of-plane antisymmetric bending
527	547	C-N-C antisymmetric bending
725	553	C-N-C symmetric stretching
805	556	Phyenyl-H out-of-plane antisymmetric bending
913	559	Phyenyl ring breathing mode
1175	568	C-phenyl, C-H in-plane antisymmetric stretching
1371	574	C-N, Phyenyl-C-phyenyl antisymmetric stretching
1534	579	Phenyl in-plane antisymmetric stretching
1585	581	C-phenyl in-plane antisymmetric stretching
1617	582	C-phenyl in-plane antisymmetric stretching

2.3.3 Excitation Intensity Dependence

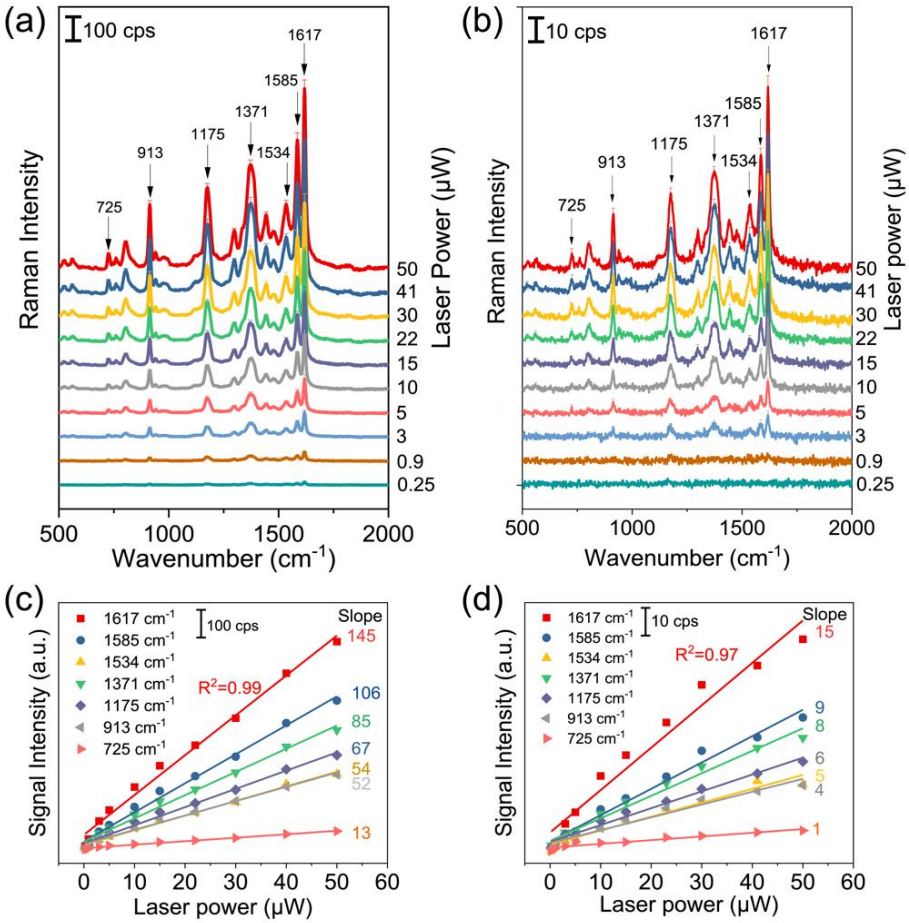

Figure 2.9 (a, b) SERS spectra of CV (10^{-4} mol/L) on ATA (a) and AT (b) substrates under series of excitation power. The results represent the average of 5 measurements, and the signals are normalized by the laser power and acquisition time. (c, d) Characteristic Raman signal intensity on ATA (c) and AT (d) structures plotted as a function of laser power, calculated from (a) and (b), respectively.

Figure 2.9 shows the excitation power-dependent SERS spectra of ATA and AT substrates decorated with 10^{-4} mol/L CV solution. The excitation power was adjusted from 50 μW to 0.25 μW by an optical attenuator. Low laser power was used in this experiment to avoid heating in the nanostructure. To show the relationship between the SERS and the laser power, the SERS intensities of several Raman peaks were plotted as a function of the excitation power, as shown in the **Figure 2.9c and d**. The

SERS intensity increased linearly with increasing the excitation laser power, which indicates it possible to carry out quantitative analysis.

2.3.4 Concentration Dependence and Limit of Determination

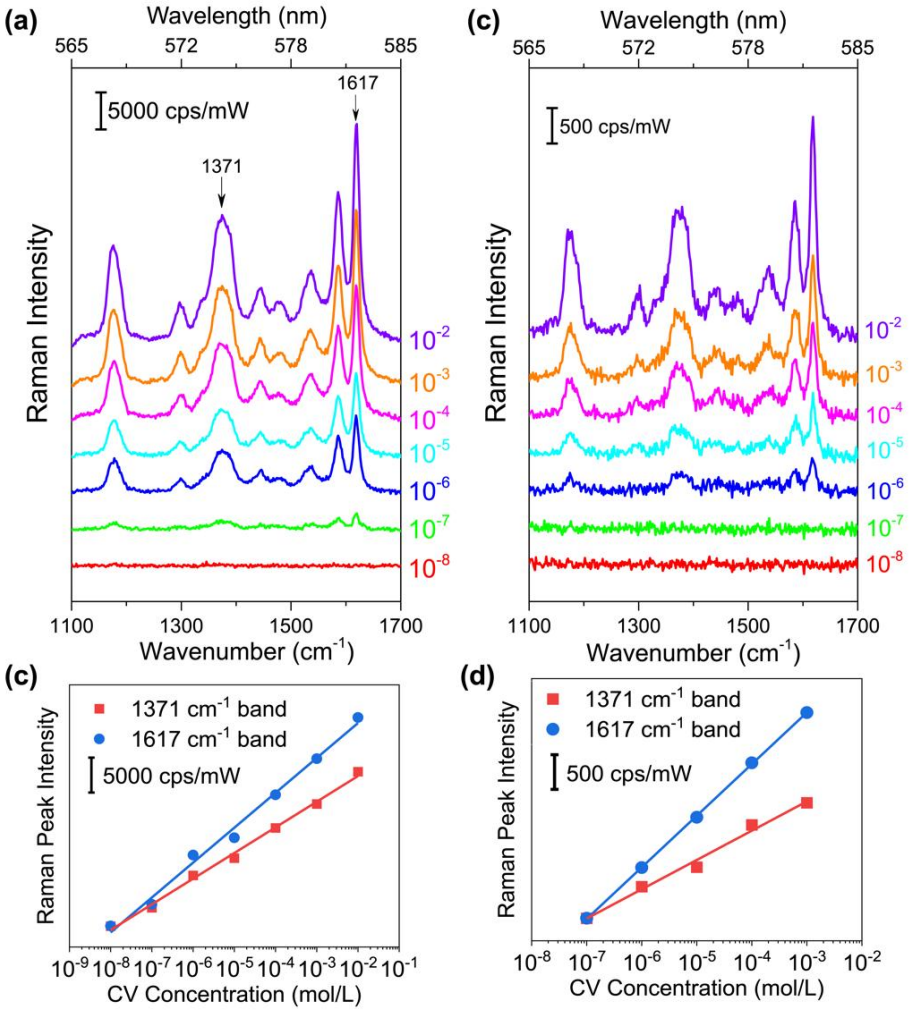

Figure 2.10 (a, b) SERS spectra of CV with different concentrations on ATA (a) and AT (b) substrates, measured under an excitation laser power of 30 μW. The results represent the average of 5 measurements, and the signals are normalized by the laser power and acquisition time. (c, d) Characteristic Raman signal intensity on ATA (c) and AT (d) structures plotted as a function of CV concentration, calculated from (a) and (b), respectively.

To investigate the limit of the determination on the ATA structure, SERS measurements of CV on ATA substrates with different concentrations were performed.

The CV molecules were decorated on ATA structures surface using a series of concentrations of CV solutions. The detection limit was defined as the concentration of the CV solution used in preparing the CV-decorated ATA and AT, since the amount of CV molecules adsorbed on Au NPs are difficult to be precisely determined. **Figure 2.10a** shows the SERS spectra of CV adsorbed on the ATA surface with a series of concentrations. Distinct characteristic peaks of CV were detected even at 10^{-7} mol/L, which is one order of magnitude lower compared with that of AT without cavities, where the distinct peaks were measured as 10^{-6} mol/L (**Figure 2.10c**). This indicates that the ATA substrate exhibits superior sensitivity and lower detection limits for SERS measurements compared to AT without cavities.

By calculating the limit of determination (LOD) using the signal-to-noise ratio (S/N) method, we confirmed that the S/N of the Raman signals of CV molecules at a concentration of 10^{-7} mol/L is 8.8, which is more than two times higher larger the standard S/N of 3. Furthermore, from the linear plot of the Raman signals as a function of the logarithm of CV concentration as shown in **Figure 2.10b**, it can be estimated that the LOD of CV on the ATA is 4×10^{-8} mol/L. The remarkably low detection limit on ATA structure could be attributed to the highly enhanced near-field intensity under the coupling between the LSPR and nanocavity on the ATA. The modal coupling condition between the nanocavity and LSPR in ATA contributes to the enhanced sensitivity and superior performance for SERS measurements, allowing for the extremely low concentration detections of CV.

When Au NPs with plasmon resonance frequency matching with that of the FP nanocavity are placed in the TiO_2/Au-film, a coupling effect occurs between the FP nanocavity and LSPR, leading to increased absorption intensity and broaden absorption band in the visible range wavelength. Additionally, this coupling results in high near-field enhancement, which is beneficial for SERS measurements.

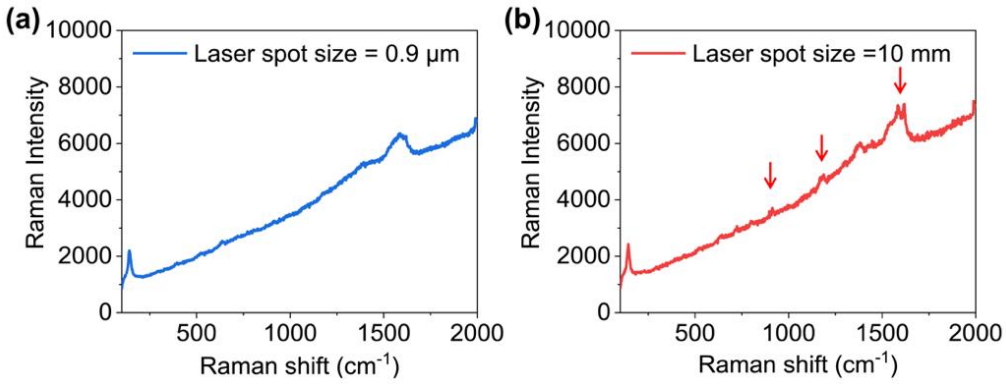

Figure 2.11 Raman spectra of CV on the ATA structure with laser spot sizes of (a) 0.9 μm and (b) 10 mm. The laser power is 120 μW. The CV concentration is 10^{-8} mol/L.

Lowering the CV molecules concentration to 10^{-8} mol/L results in a reduction of the SERS intensity, which because there are very few CV molecules present in the measuring area. To prove this, we performed the SERS measurements using an increased laser spot size and raised power or the excitation laser. The Raman signals corresponding to the CV bands could still be recognized, as shown in **Figure 2.11b**. This suggests that even at very low concentrations, the SERS effect is still detectable under optimized experimental conditions.

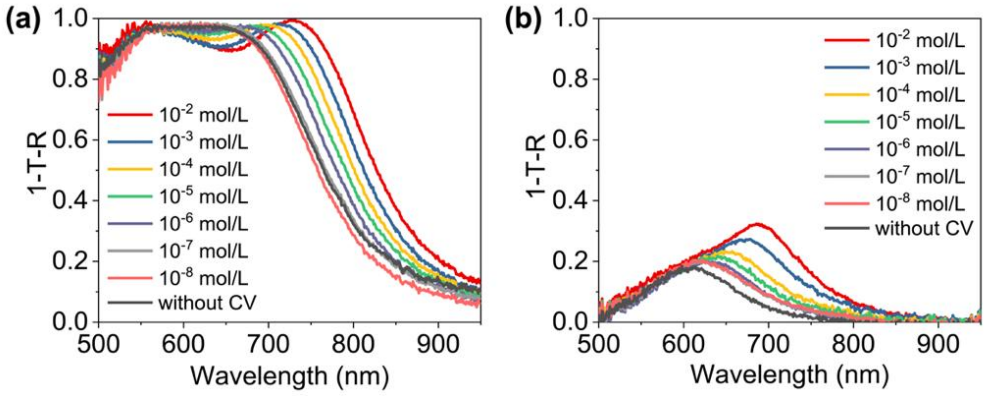

Figure 2.12 Absorption spectra of ATA (a) and AT (b) structures decorated by CV with concentrations from 0 to 10^{-2} mol/L.

To investigate the impact of CV concentration on the Raman signal, the ATA and AT samples were decorated using CV solutions with concentrations ranging from 10^{-8}

to 10^{-2} mol/L. The absorption spectra of CV-decorated ATA and AT are shown in **Figure 2.12**. From the plasmon band of the Au NPs shown in the **Figure 2.12b**, a significant red shift from ~610 to ~700 nm can be observed as the CV concentration increases from 10^{-8} to 10^{-2} mol/L. This significant band redshift of the absorption spectra could be due to the charge transfer effect occured between CV molecules and Au NPs.

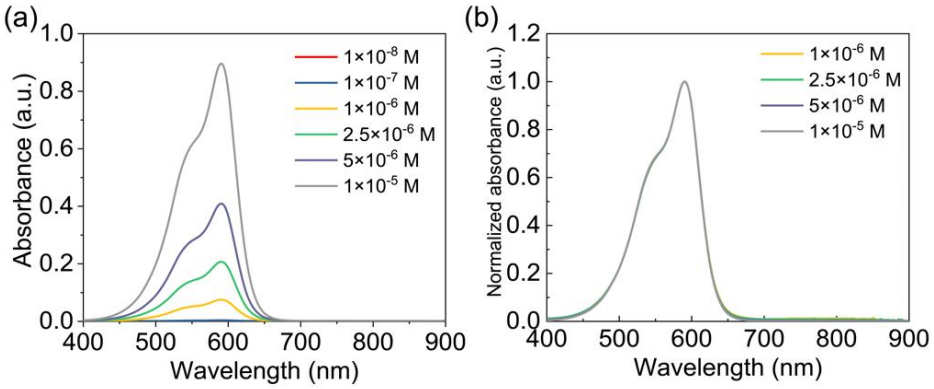

Figure 2.13 Absorbance (a) and normalized absorbance spectra (b) of CV solution with a series of concentrations from 10^{-8} to 10^{-5} mol/L.

The absorbance spectra of CV solution with different concentration are presented in **Figure 2.13**. From the normalized absorbance, we confirmed the absence of any aggregation of CV molecules in the solution, even at the highest concentration in this experiment, due to their almost identical absorption bands. In addition, the absorption band of CV molecules at 590 nm is far from the absorption enhancement region.

In **Figure 2.10b and d**, the SERS intensities at Raman shift of 1617 and 1371 cm^{-1} on ATA and AT structures, respectively, are shown as a function of the CV concentration, with the concentration axis expressed as a logarithmic scale. The Raman signals exhibit a logarithmic increase as the CV concentration is increased, in line with findings in existing reports.[30-31] According to this relationship between the SERS intensity and the concentration of adsorbed CV molecules, the quantitative detection can be facilitated.

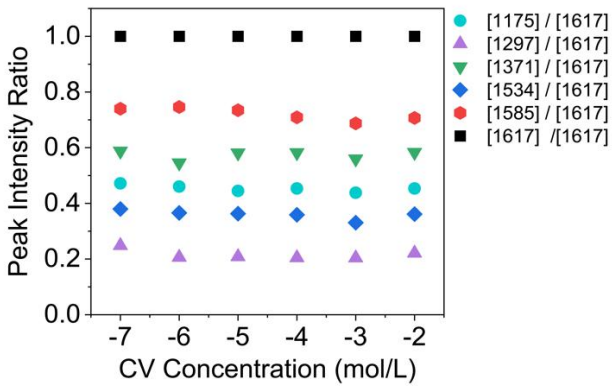

Figure 2.14 Normalized peak intensity as a function of CV concentration. All selected Raman peak intensities were normalized to the peak intensity at 1617 cm^{-1}.

Notably, despite the increasing Raman intensity with higher CV concentrations, the ratio of the Raman signals at every CV concentration remains nearly constant (**Figure 2.14**). This observation suggests that the charge transfer at the interface between the molecule and metal has minimal impact on the SERS spectrum.

2.3.5 Spatial Homogeneity Effect

Under the modal coupling condition, the LSPR of multiple Au NPs which are located in the coherence area oscillate coherently, leading to a spatial-distribution smoothing of the near-field intensity over each Au NP. Consequently, the intensity of the SERS signal of CV on the Au NPs is expected to exhibit spatial homogeneity. In contrast, in the absence of modal coupling, the LSPR of every individual Au NP is incoherent, resulting in non-smoothed near-field intensities and spatial inhomogeneity of the SERS signal intensity of CV on the Au NPs.

In our previous study, we determined the dephasing time of the LSPR on ATA to be approximately 4.5 fs using time-resolved photoemission electron microscopy (TR-PEEM) measurements.[22] Based on this value, we calculated the coherence area to be approximately 1 μm in diameter. While the coherence area and coherence length are not directly correlated, we anticipate that the coherence area would not greatly deviate from our calculation.

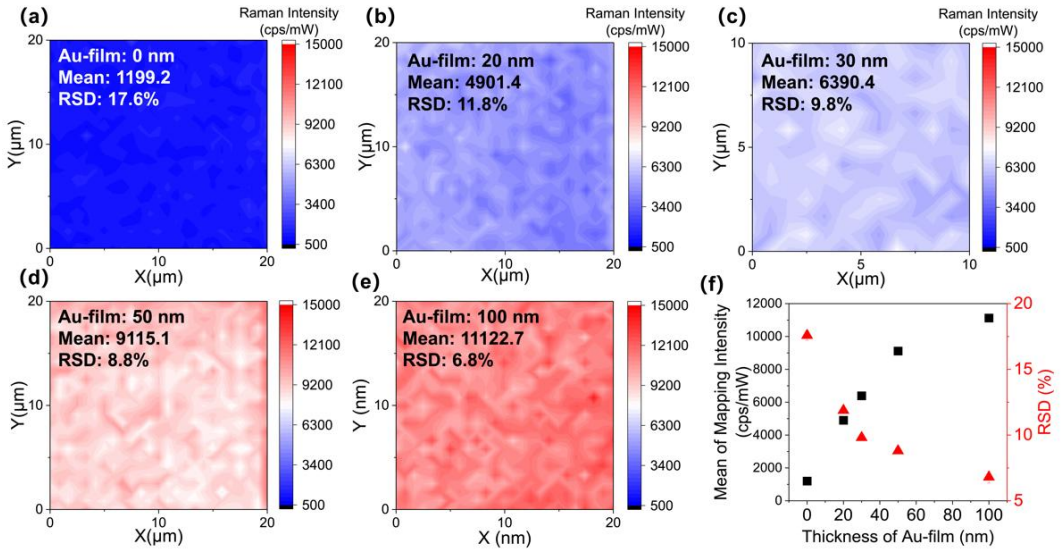

Figure 2.15 Raman intensity mapping images of ATA structures with varying Au-film thicknesses: (a) 0 nm, (b) 20 nm, (c) 30 nm, (d) 50 nm, and (e) 100 nm, with a wavenumber of 1617 cm^{-1}. The CV solution concentration used here is 10^{-6} mol/L. The Raman signal intensity mean value and relative standard deviation (RSD) are indicated on the images, showing the spatial distribution of the SERS signal. (f) The mean (represented by black squares) and RSD (indicated by red triangles) of the Raman intensity plotted against the thickness of the Au-film, obtained from the Raman mappings shown in (a-e). The error bars on the graph represent the uncertainty in the measurements.

For validating our prospection, we performed Raman mapping on both ATA and AT over a 20×20 μm^2 area, as shown in **Figure 2.15e and a**, respectively. The substrates are decorated with CV molecules by the solution concentration of 10^{-6} mol/L. To obtain the relative standard deviation (RSD), which we used to assess the spatial homogeneity, the standard deviation value was divided by the mean value obtained from the Raman mapping images. The mean value and RSD are indicated in the figures.

The Raman mapping mean intensity value on ATA is approximately 10 times higher compared with that on AT under the same laser intensity irradiation, which is comply with the results shown in **Figure 2.8**. Furthermore, the RSD of Raman

mapping on ATA is only 6.8%, significantly smaller than that on AT, which is 17.6%.

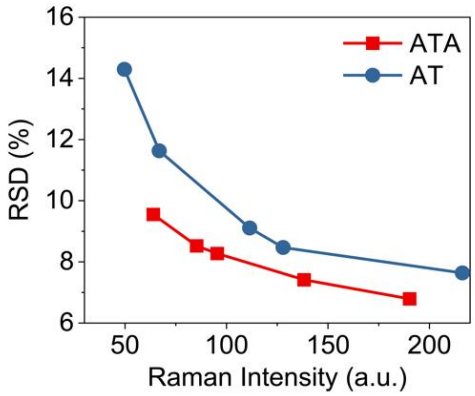

Figure 2.16 RSD as a function of the Raman intensity. The excitation laser intensities range from 4.5 μW to 30 μW on ATA and 0.1 mW to 4.0 mW on AT structures.

To account for detect noise and any other detect errors, the RSD values of ATA and AT with same SERS intensities was compared. **Figure 2.16** shows the RSD as a function of Raman intensity. The result demonstrates that the RSD of ATA is about 10 ~ 20% smaller than that of AT. These findings show that SERS signals measured on ATA exhibit higher spatial homogeneity compared with that detected on AT.

To gain further insight into the homogeneous Raman intensity on the ATA structure, we manipulated the optical quality of the FP nanocavity by varying the thickness of the Au-film (ranging from 0 to 100 nm) to study the effect on spatial homogeneity of the cavity. The Raman mapping on a 20×20 μm^2 area was conducted on ATA structure with different Au-film thicknesses (0, 20, 30, 50, and 100 nm), as shown in **Figure 2.15a-e**. The mean and RSD values of the Raman intensities for each case in the three different experiments are plotted in **Figure 2.15f**, along with the corresponding error bars. The mean value of Raman intensity increases rapidly with the thickness of the Au-film and saturates when the Au-films is thicker. In contrast, the RSD exhibits a sharp decline from 17.6% to 6.8% as the thickness of the Au-film increases from 0 to 100 nm. This finding shows that the intensity at each point on the ATA with a thicker Au-film thickness exhibits excellent homogeneity. The controlled variation in Au-film thickness provides evidence that the optical quality of the FP

nanocavity plays a crucial role in achieving spatial homogeneity in the Raman intensity on ATA.

As discussed earlier, when the LSPR of Au NPs is in resonance with the FP nanocavity, they undergo coherent coupling and form a coherence area surrounding the Au NPs. This coherent coupling leads to a smoothing effect on the near-field intensity distribution on each Au NP in the coherence area. As the thickness of the Au-film in ATA increases, the coherent coupling between the FP nanocavity and LSPR is enhanced, resulting in a larger coherence area around each Au NP. Consequently, the near-field smoothing effect caused by the plasmon-nanocavity coupling is further promoted on ATA with a thicker Au-film, leading to the generation of spatially homogeneous Raman mapping. The improved optical quality of the nanocavity plays a pivotal role in achieving this enhanced spatial homogeneity.

2.3.6 Effect on the Near-Field Distribution

1. FDTD simulation

To gain insights into the remarkable SERS enhancement, we conducted near-field distribution calculations around individual Au NPs on both ATA and AT substrates under 532 nm light excitation using the FDTD method. It should be noted that the simulated structures in this study represent a single Au NP.

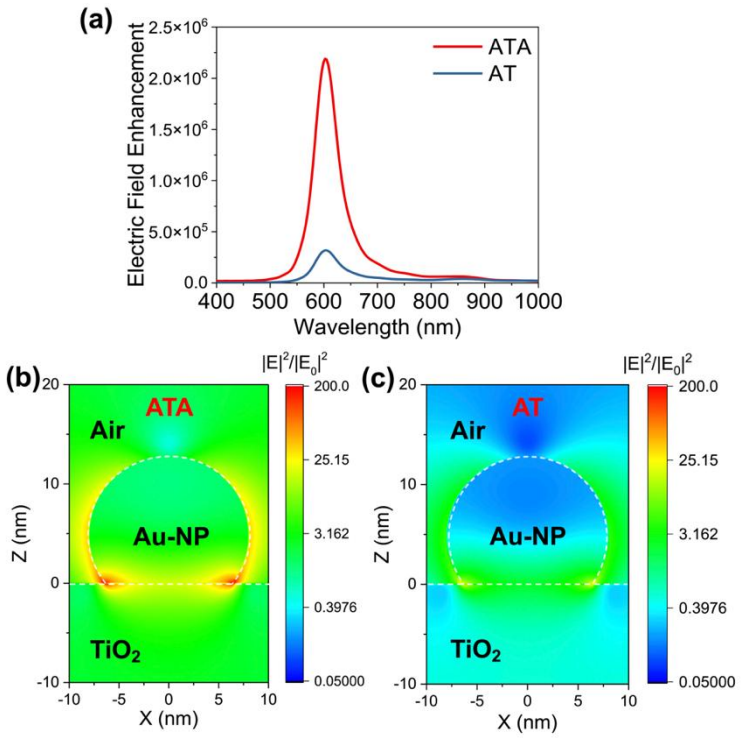

Figure 2.17 (a) Integrated near- field enhancement on ATA and AT structures calculated by integration of the 1.0 nm region at the surface of the substrates, which is obtained by FDTD simulation. (b, c) The cross-sectional near-field distribution on ATA and AT structures, respectively.

As shown in **Figure 2.17**, the near-field spectra of ATA exhibited an approximately 7-fold higher intensity compared to that of AT at a wavelength of 532 nm. The cross-section near-field distribution on ATA (**Figure 2.17b**) clearly showed much stronger near-field intensity compared to that of AT (**Figure 2.17c**). Particularly, the maximum near-field, known as "hot spots", appeared at the boundary corner between the Au NP and TiO_2 in the ATA structure. These results indicate that the ATA substrate exhibits significantly enhanced near-field intensity, especially at the "hot spots", which is likely responsible for the observed remarkable SERS enhancement.

2. FEM simulation

The electromagnetic field simulation based on the FEM using the COMSOL Multiphysics software package further supports the smoothing effect of the near-field intensity of each Au NP in the coherence area.

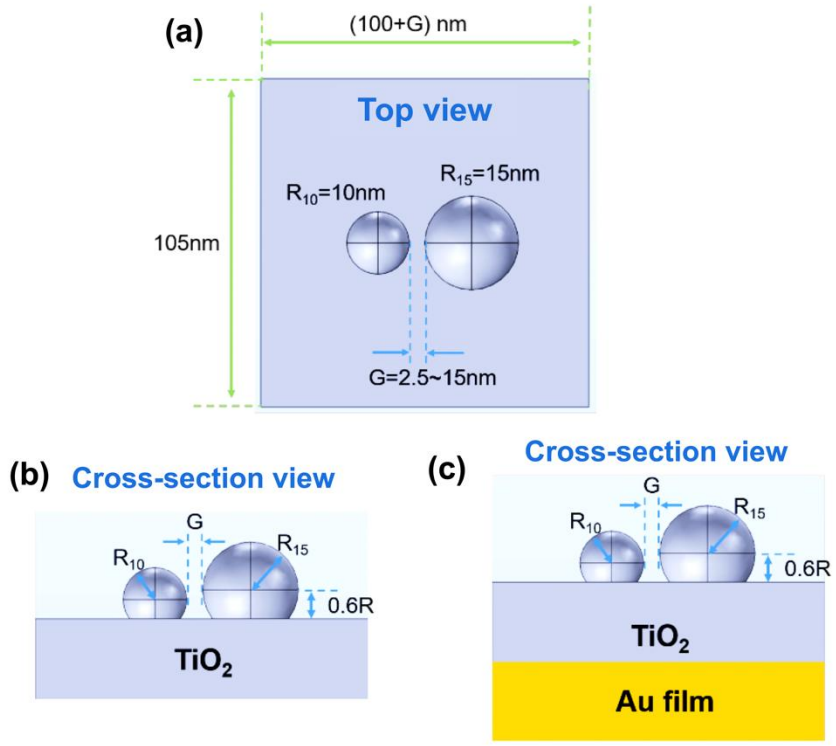

Figure 2.18 FEM simulation models of AT and ATA. (a) Top view schematic; (b) and (c) cross-section views of AT and ATA structures, respectively. The radius (R) of the Au NPs was set as 10 and 15 nm, R_{10} and R_{15} represent radii of 10 and 15 nm, respectively, and the gap (G) ranged from 2.5 to 30 nm.

The simulation models of ATA and AT were shown in **Figure 2.18,** the Au NPs were modeled as partially truncated spheres with specific radii and positioned on a TiO_2 substrate and a nanocavity to mimic the coherent coupling effect on the homogeneity of the near-field distribution. The gap distance between the two Au NPs was varied to explore different coupling scenarios.

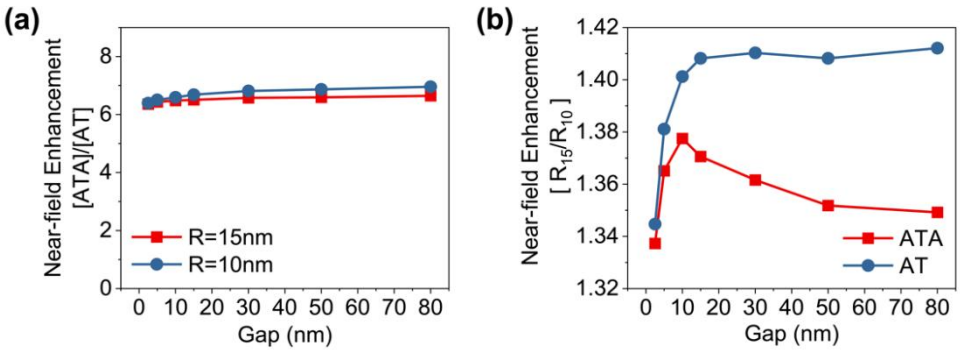

Figure 2.19 (a) Near-field enhancement ratio between AT and ATA, which was calculated by dividing the near-field intensity of Au NPs on ATA by that on AT. The black and red plots represent Au NPs with radii of 15 and 10 nm, respectively. (b) Near-field deviation of Au NPs with radii of 15 and 10 nm on AT and ATA substrates. The near-field deviation of Au NPs was calculated by dividing the deviation of their individual near-field intensity by the mean value of their near-field intensity.

The simulation results in **Figure 2.19a** demonstrate that the near-field intensity on ATA is increased by approximately 7 times compared to that on AT, which is consistent with the experimental observations shown in **Figure 2.17**. More importantly, the near-field deviation on ATA is smaller than that on AT, as illustrated in **Figure 2.19b**, providing further evidence that ATA exhibits a smaller deviation in the Raman intensity, as shown in **Figure 2.15f** and **Figure 2.16**. These simulation findings reinforce the idea that the plasmon-nanocavity coupling in ATA promotes a more spatially homogeneous near-field intensity distribution, resulting in the enhanced spatial homogeneity observed in the Raman measurements.

Indeed, the near-field deviations of the two Au NPs on both AT and ATA increase as the gap between them increases, and this deviation tends to become saturated after reaching a certain gap distance. In the case of AT, when the gap becomes large, the two Au NPs behave as individual particles with negligible interaction, resulting in a relatively large near-field deviation. On the other hand, as discussed earlier, the coherent coupling between the LSPR of the Au NPs and the cavity on the ATA structure smoothens the near-field intensity deviation on each Au NP, leading to a relatively small near-field deviation even at smaller gap distances.

As the gap distance between the Au NPs decreases, the near-field interaction between them becomes stronger, leading to a decrease in the difference in near-field intensity between the two Au NPs. This stronger interaction further contributes to the homogenization of the near-field distribution on each Au NP within the coherence area. Consequently, the plasmon-nanocavity coupling in ATA not only enhances the overall near-field intensity but also promotes the spatial homogeneity of the near-field

intensity distribution, making ATA a promising substrate for achieving highly reproducible and spatially homogeneous SERS measurements.

2.4 Conclusions

In conclusion, the optimized SERS substrate, consist of a monolayer of Au NPs on a nanocavity formed in TiO_2/Au-film, demonstrates significant enhancements in the SERS signal of CV in comparison to Au NPs/TiO_2 structures without any cavities. This enhancement is achieved through the coupling between the LSPR in AuNPs and the FP nanocavity resonance in TiO_2/Au-film. The SERS signal of CV shows a linear increase with the excitation power as well as the logarithm of CV concentration within a certain range, indicating it eligible for quantitative detection.

The coupling between LSPR and FP nanocavity resonance leads to significant near-field enhancement and spatial homogeneity of the near-field distribution. The coherent coupling between the LSPR of each Au NP and the FP nanocavity results in smoothed near-field distributions on each Au NP within the coherence area. This spatial homogeneity is visually confirmed through SERS mapping, which demonstrates consistent enhancement over the entire surface of the ATA substrate. Furthermore, simulations provide evidence of the reduction in near-field deviation under plasmon-nanocavity coherent coupling conditions.

Overall, the plasmon-nanocavity coupling ATA structure holds great promise as a sensitive, reproducible, and spatially homogeneous SERS substrate for detecting a wide range of chemicals and biomolecules, which makes it qualified for use in the study the plasmon-nanocavity coupling effects on the plasmon-induced water oxidation reactions.

2.5 References

[1] E. C. Le Ru, E. Blackie, M. Meyer, P. G. Etchegoin, *J. Phys. Chem. C* **2007**, 111, 13794.

[2] P. Johansson, H. Xu, M. Käll, *Phys. Rev. B* **2005**, 72, 035427.

[3] K.-H. Su, S. Durant, J. M. Steele, Y. Xiong, C. Sun, X. Zhang, *J. Phys. Chem. B* **2006**, 110, 3964.

[4] W. B. Cai, B. Ren, X. Q. Li, C. X. She, F. M. Liu, X. W. Cai, Z. Q. Tian, *Surface Science* **1998**, 406, 9.

[5] A. J. Haes, C. L. Haynes, A. D. McFarland, G. C. Schatz, R. P. Van Duyne, S. Zou, *MRS Bull.* **2005**, 30, 368.

[6] P. G. Etchegoin, E. C. Le Ru, Phys. *Chem. Chem. Phys.* **2008**, 10, 6079.

[7] T. Jiang, G. Chen, X. Tian, S. Tang, J. Zhou, Y. Feng, H. Chen, *J. Am. Chem. Soc.* **2018**, 140, 15560.

[8] M. Kim, S. M. Ko, J.-M. Kim, J. Son, C. Lee, W.-K. Rhim, J.-M. *Nam, ACS Cent. Sci.* **2018**, 4, 277.

[9] K. N. Kanipe, P. P. F. Chidester, G. D. Stucky, M. Moskovits, *ACS Nano* **2016**, 10, 7566.

[10] L. Zhang, C. Guan, Y. Wang, J. Liao, *Nanoscale* **2016**, 8, 5928.

[11] N. Tognalli, A. Fainstein, E. Calvo, C. Bonazzola, L. Pietrasanta, M. Campoy-Quiles, P. Etchegoin, *The Journal of Chemical Physics* **2005**, 123, 044707.

[12] J. M. Caridad, S. Winters, D. McCloskey, G. S. Duesberg, J. F. Donegan, V. Krstić, *Sci Rep* **2017**, 7, 45548.

[13] J. B. Jackson, S. L. Westcott, L. R. Hirsch, J. L. West, N. J. Halas, *Applied Physics Letters* **2003**, 82, 257.

[14] Y. Yokota, K. Ueno, H. Misawa, *Small* **2011**, 7, 252.

[15] T. Zhang, Y. Sun, L. Hang, H. Li, G. Liu, X. Zhang, X. Lyu, W. Cai, Y. Li, *ACS Appl. Mater. Interfaces* **2018**, 10, 9792.

[16] X. Shi, K. Ueno, T. Oshikiri, Q. Sun, K. Sasaki, H. Misawa, *Nature Nanotech* **2018**, 13, 953.

[17] X. Shi, X. Li, T. Toda, T. Oshikiri, K. Ueno, K. Suzuki, K. Murakoshi, H. Misawa, *ACS Appl. Energy Mater.* **2020**, 3, 5675.

[18] Y. Cao, T. Oshikiri, X. Shi, K. Ueno, J. Li, H. Misawa, *ChemNanoMat* **2019**, 5, 1008.

[19] Y. Suganami, T. Oshikiri, X. Shi, H. Misawa, *Angew. Chem. Int. Ed.* **2021**, 60, 18438.

[20] Y.-E. Liu, X. Shi, T. Yokoyama, S. Inoue, Y. Sunaba, T. Oshikiri, Q. Sun, M. Tamura, H. Ishihara, K. Sasaki, H. Misawa, *ACS Nano* **2023**, 17, 8315.

[21] T. Watanabe, B. Pettinger, *Chemical Physics Letters* **1982**, 89, 501.

[22] L. Angeloni, G. Smulevich, M. P. Marzocchi, Journal of Raman Spectroscopy **1979**, 8, 305.

[23] S. Fateixa, H. I. S. Nogueira, T. Trindade, *ACS Omega* **2018**, 3, 4331.

[24] S. L. Kleinman, E. Ringe, N. Valley, K. L. Wustholz, E. Phillips, K. A. Scheidt, G. C. Schatz, R. P. Van Duyne, *J. Am. Chem. Soc.* **2011**, 133, 4115.

[25] P. B. Johnson, R. W. Christy, *Phys. Rev. B* **1972**, 6, 4370.

[26] J. R. DeVore, *J. Opt. Soc. Am.* **1951**, 41, 416.

[27] F. A. Harraz, A. A. Ismail, H. Bouzid, S. A. Al-Sayari, A. Al-Hajry, M. S. Al-Assiri, *Applied Surface Science* **2015**, 331, 241.

[28] K. Zhang, T. Zeng, X. Tan, W. Wu, Y. Tang, H. Zhang, *Applied Surface Science* 2015, 347, 569.

[29] A. Shrivastava, V. Gupta, *Chron Young Sci* **2011**, 2, 21.

[30] M. Y. Lv, H. Y. Teng, Z. Y. Chen, Y. M. Zhao, X. Zhang, L. Liu, Z. Wu, L. M. Liu, H. J. Xu, *Sensors and Actuators B: Chemical* **2015**, 209, 820.

[31] I. Izquierdo-Lorenzo, S. Sanchez-Cortes, J. V. Garcia-Ramos, *Langmuir* **2010**, 26, 14663.

Chapter 3 Effect of Plasmon-Nanocavity Coherent Coupling on Plasmon-Induced Water Oxidation

3.1 Introduction

Metal NP-supported semiconductors have been attracting a lot of attention due to the outstanding potential to improve the efficiency of photochemical water splitting under visible light irradiation based on the LSPR of metal NPs.[1-6] In chapter 2, an optimized ATA structure has been developed and shown to be a sensitive, reproducible, and spatially homogeneous SERS substrate. It has been reported by previous studies that the ATA structure, which demonstrates significant modal strong coupling between the LSPR of Au NPs and the FP nanocavities present in TiO_2/Au-film, has been successfully utilized for water splitting applications.[7-9] Additional research findings also indicate that the enhancement of hot-electron generation efficiency can be attributed to the quantum coherence observed between the LSPR and the nanocavity.[10] Therefore, understanding the generation and transformation of the electron-hole pairs is vital for comprehending the whole photochemical reaction processes. To systematically delve into the mechanisms behind the plasmon-induced water oxidation observed under strong coupling conditions, this chapter employed *in situ* electrochemical surface-enhanced Raman spectroscopy (EC-SERS) to investigate the intermediates of the plasmon-induced water oxidation.

EC-SERS stands as a powerful and innovative technique, enabling real-time observations of electrochemical reaction intermediates at the electrode surface. [11-14] The application of EC-SERS has been pivotal in providing valuable insights into the intricate photochemical processes. Recent research endeavors have centered on the study of intermediates involved in plasmon-induced water oxidation on Au-NDs/TiO_2 photoanodes, with particular emphasis on the influential role of the AuOOH intermediate.[15] This highly oxidized species plays a crucial role in the oxygen evolution reaction, making it essential to comprehend its formation and behavior for

the optimization of photoelectrochemical applications, especially in water oxidation processes.[16-17]

In this chapter, an optimized plasmon-nanocavity coupling structure, which consist of Au-Ag alloy NPs/TiO_2/Au-film (AATA), was used as the photoanode to investigate the intermediates involved in the water oxidation reaction by EC-SERS measurements. The main objective was to investigate the enhancement mechanism of the water oxidation under the fascinating strong coupling conditions provided by the AATA structure. Notably, the AATA photoanode possesses a resonance band that closely aligns with the wavelength of the Raman excitation laser, enabling efficient SERS signal enhancement. Additionally, the AATA structure exhibits ultrastrong coupling properties, attributed to the high oscillator strength of the Au-Ag alloy NPs present in the system.[18] The Au-Ag alloy NPs/TiO_2 (AAT) photoanode without Au-film was also fabricated to compare with the AATA photoanode. The EC-SERS spectra of water oxidation intermediates under various electrochemical potentials were observed. Furthermore, the onset electrochemical potentials of the EC-SERS signals corresponding to these intermediates was estimated. Additionally, a speculation regarding the potential enhancement mechanism of the water oxidation reaction in the AATA structure in strong coupling condition due to quantum coherence effects was raised. The interaction between the LSPR of the Au-Ag alloy NPs and the FP nanocavities in the TiO_2/Au-film could foster quantum coherence effects, ultimately impacting the water oxidation efficiency.

3.2 Experimental Section

3.2.1 Fabrication of Au-Ag alloy NPs/TiO_2/Au-film (AATA) Structure

As depicted in **Figure 3.1**, the fabrication process of the AATA structure involved the use of a silica glass substrate (SiO_2, 10 × 10 × 1 mm^3). To ensure a clean surface, the silica substrates were sequentially cleaned with acetone, methanol, and deionized

water in an ultrasonic bath for 5 minutes and then dried using pure N_2 flow. A layered structure, which consist of a 2-nm thick layer of titanium (Ti), a 100-nm thick layer of Au, and another 2-nm thick layer of Ti, was formed on the cleaned silica glass substrate using a Helicon sputtering system (ULVAC, MPS-4000C1/HC1). The resulting sequence of layers was Ti/Au/Ti on the silica glass substrate. Subsequently, a 180-nm thick film of TiO_2 was deposited using an atomic layer deposition system (Picosun, SUNALETM R series). For this step, $TiCl_4$ and H_2O were used as the precursors, and the deposition process was carried out at a temperature of 300 °C. To complete the AATA structure, a multilayer of metals consisting of Au and Ag films was sequentially evaporated onto the TiO_2 film using a vacuum evaporator with a deposition rate of 0.1 Å/s. The specific order of the layers in the multilayer was as follows: 1.8 nm Ag, 5.3 nm Au, 1.7 nm Ag, and 5.2 nm Au. Subsequently, the fabricated samples underwent annealing at 400 °C in a nitrogen (N_2) atmosphere for 24 hours, resulting in the formation of Au-Ag alloy NPs on the surface of the TiO_2 film. This annealing process was crucial for the appearance of the Au-Ag alloy NPs.

For the control group, a different structure known as the Au-Ag alloy NPs/TiO_2 structure (AAT) was fabricated. In this case, the process was similar, except that a layer of Au film was not included. Additionally, a high-durability transparent conductive film glass (TCO glass, 10 × 10 × 1.1 mm^3, GEOMATEC CO., LTD.) was used as the substrate instead of silica glass. The cleaning process and fabrication conditions of the TiO_2 film (180 nm) and Au-Ag alloy NPs were the same as those described above for the AATA structure.

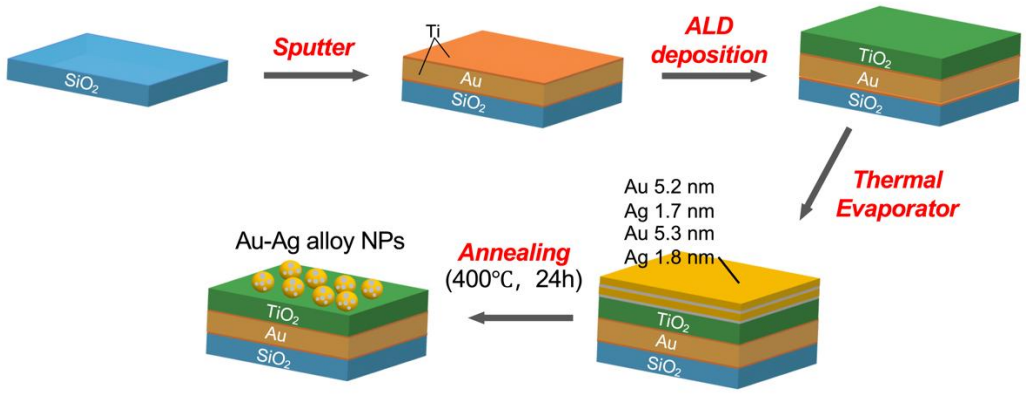

Figure 3.1 Schematic preparation of Au-Ag alloy NPs/TiO_2/Au-film (AATA) structure.

3.2.2 Characterizations

Transmittance (T) and reflectance (R) spectra were obtained using a photonic multichannel analyzer system (Hamamatsu Photonics, PMA C7473) coupled with an optical microscope (Olympus, BX-51). Absorption was calculated as 1-T-R.

Surface morphology was observed using field-emission scanning electron microscopy (JSM-6700FT (JEOL)) at an electron accelerating voltage of 15 kV, resulting in a maximum resolution of 1 nm.

3.2.3 Photoelectrochemical Measurements

Photoelectrochemical measurements were carried out using a three-electrode system on an electrochemical analyzer station (CHI660E), as shown in **Figure 3.2**. The obtained structure AATA and AAT are served as the working electrode (WE). As for the counter electrode (CE) and reference electrode (RE), a platinum wire and Ag/AgCl electrode were employed, respectively.

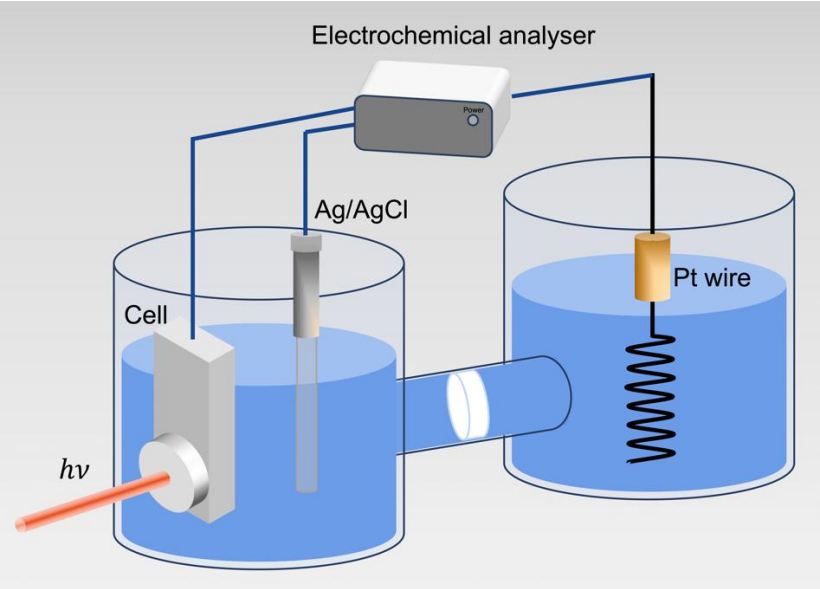

Figure 3.2 Schematic preparation of photoelectrochemical measurement system.

The WE used in the experiments was the AATA or AAT structure with an indium-gallium alloy (4:1 weight ratio) coated onto the backside equipped in a home-made Teflon holder (**Figure 3.3**). The supporting electrolyte used was a 0.1 mol/L NaF solution with a pH of 7. To eliminate dissolved oxygen, the NaF solution was bubbled with nitrogen gas for 1 hour before and during the measurements. For illumination, an 800 W xenon lamp served as the light source. Prior to conducting the photoelectrochemical and EC-SERS measurements, the AATA and AAT electrodes underwent a pretreatment step. They were irradiated with 620 nm light while applying a potential of 0.5 V (vs. Ag/AgCl) for 2 hours, promoting an anodic oxidation reaction to remove Ag and Ag oxide from the surface of the Au-Ag alloy NPs, as previously reported.

For the calculation of the incident photon-to-electron conversion efficiency (IPCE), a bias with +0.3 V vs. SCE was applied to measure i-t cures to calculate the photocurrent. Then, the IPCE is obtained by applying the following equation:

$$IPCE(\lambda) = \frac{1240 \times I\ (A/cm^2)}{\lambda(nm) \times P\ (W/cm^2)} \tag{3.1}$$

where I is the photocurrent density under the irradiation of monochromatic light, λ is the wavelength of the monochromatic incident light, and P is the light intensity.

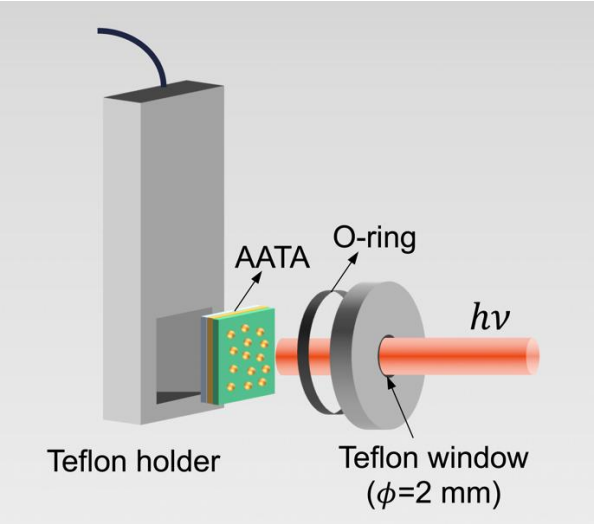

Figure 3.3 Schematic illustration of working electrode cell.

3.2.4 Electrochemical Surface-Enhanced Raman Spectroscopy (EC-SERS) Measurements

In situ EC-SERS measurements were conducted by a Raman microscope system (Renishaw, inVia Reflex) equipped with a 63× water immersion objective lens (HC APO L 63×/0.90 W U-V-I, Leica). A 785 nm laser served as the excitation source. Raman spectra were collected in the wavenumber range of 200−2000 cm^{-1} with a resolution of 1.5 cm^{-1}. Throughout this study, all SERS spectra were obtained with an acquisition time of 30 seconds and an accumulation of five. The electrochemical measurements were performed using a home-made three-electrode system, as shown in **Figure 3.4**. The AATA or AAT structure was employed as the WE, while platinum wires were used as the RE and CE. The electrolyte used in the experiments was a 0.1 mol/L NaF solution. The electrochemical experiments were controlled using an electrochemical analyzer station (CHI660E). During the EC-SERS measurements, the applied potential was varied from negative to positive in a regular sequence. To explore the isotopic effect, deuterium oxide (D_2O, 99.9 atom % D, Sigma–Aldrich) and water-^{18}O ($H_2{}^{18}O$, 97 atom % ^{18}O, Sigma–Aldrich) were used in separate

experiments.

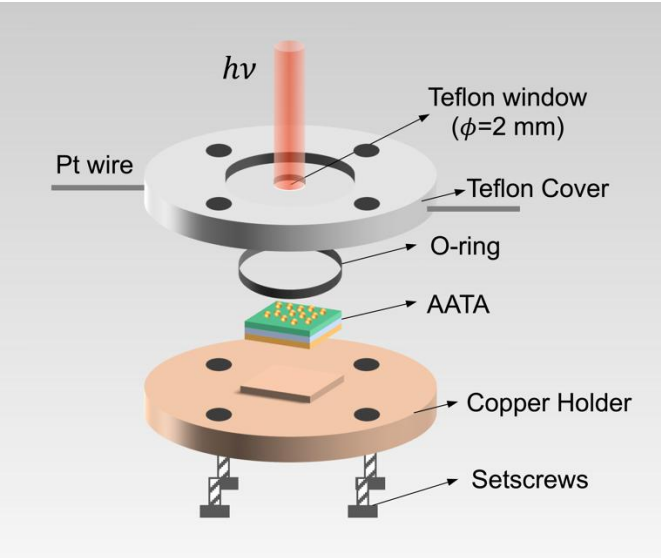

Figure 3.4 Schematic illustration of the home-made three-electrode system cell used for EC-SERS measurement.

3.2.5 Simulations

Finite-difference time domain (FDTD) simulations were conducted using Lumerical, Inc. software to analyze the far-field and near-field spectra and the near-field intensity distribution of both the AATA and AAT substrates. FDTD simulations were performed on a discrete and homogeneously spaced mesh with a size of 0.1 nm. The Specific FDTD simulation models were created to match the dimensions of the ATA and AT substrates. The optical properties of Au and Ag were derived from Johnson and Christy's data.[19] TiO_2 was considered a dielectric material with an average refractive index of n=2.4.[20]

3.3 Structural Optimization of AATA Structure

In chapter 2, we successfully developed a highly sensitive and spatially homogeneous SERS detection structure named ATA, comprising a 100-nm Au film, a

30 nm TiO_2 thin film, and small-sized Au NPs. This ATA structure without inlaid layer exhibited relatively weak coupling and the peak absorption in the wavelength range of 550 to 650 nm (as shown in **Figure 2.4**). In this chapter, the water oxidation intermediates under strong coupling conditions were invested. First of all, the resonance band should be modulated to match the Raman excitation wavelength. Here we conducted the EC-SERS measurements using 785 nm excitation, because that the Au will experience d-band excitation under 532 nm laser excitation, which is unsuitable for detecting plasmon-induced water oxidation. Additionally, it is of great importance to a high visible-range wavelength absorption and near-field enhancement that the coupling condition between the LSPR in the metal NPs and the FP nanocavity resonance is sufficiently strong. To optimize the coupling strength and the peak absorption wavelength of the structure used for investing water oxidation intermediates under strong coupling conditions, the wavelengths of the LSPR and the FP nanocavity should be manipulated to be close to each other and around 785 nm. The wavelength of plasmon resonance which is due to the collective oscillations of the electrons at the surface of the NPs, strongly depends on the size and shape of the NPs, the interparticle distance, and the dielectric property of the surrounding medium. In cases of the FP nanocavity resonance, the wavelength is regulated by the thickness of the TiO_2 film.

3.3.1 Au-Ag Ratio of the Au-Ag alloy NPs

Modulating the resonance band of the LSPR and nanocavity to 785 nm proved to be challenging due to the lower splitting energy of the ATA structure.[21] To overcome this limitation, we opted to employ Au-Ag alloy NPs with a higher oscillator strength, which allowed us to effectively shift the resonance band of the AATA structure to 785 nm.[22-26] Our group has previously reported that the AATA structure incorporating Au-Ag alloy NPs exhibits a larger splitting energy of 520 meV and achieves higher water oxidation efficiency compared to the ATA structure.[18] This improvement can be attributed to the exceptional properties of Au-Ag alloy NPs, including their high

oscillator strength, and enhanced hot-electron injection efficiency.[18] In this chapter, the resonance band was able to be tuned by introducing the Au-Ag alloy NPs to the AATA structure, and the photoelectrochemical performance was optimized, thus providing valuable insights into the water oxidation reaction under strong coupling conditions.

The wavelength of plasmon resonance which is due to the collective oscillations of the electrons at the surface of the Au-Ag alloy NPs, strongly depends on the component, size, shape, and the interparticle distance of the Au-Ag alloy NPs. In this part, the fabrication condition effect of the Au-Ag alloy NPs on the modal strong coupling conditions, the optical properties, and the photoelectrochemical performances are researched.

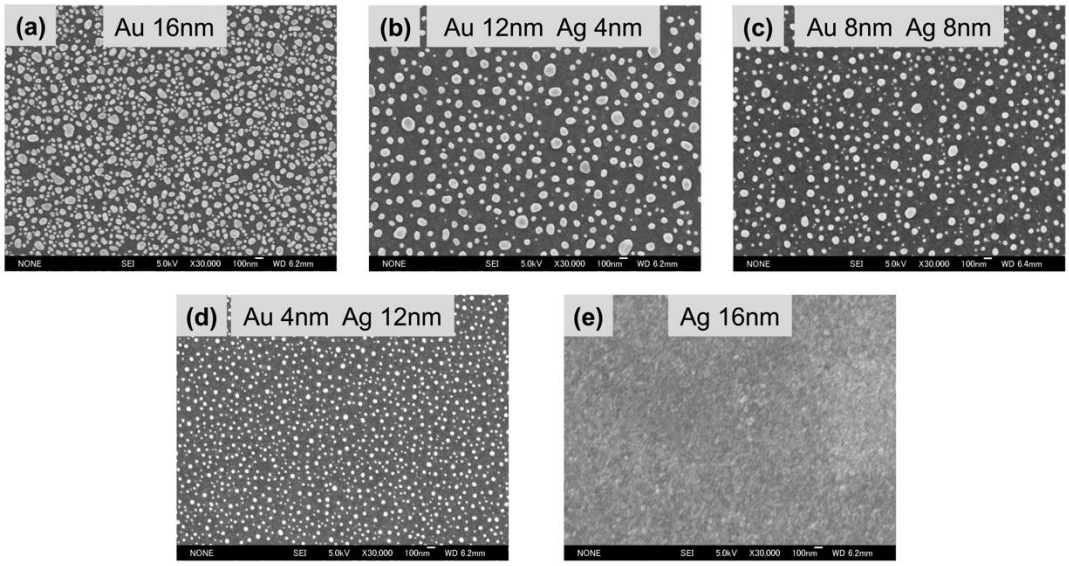

Figure 3.5 SEM images of Au-Ag alloy NPs made of Au and Ag film with different volume ratios. (a) Au 16 nm, (b) Au 12 nm, Ag 4 nm, (c) Au 8 nm, Ag 8 nm, (d) Au 4 nm, Ag 12 nm, (e) Ag 12 nm. The deposition thickness of the Au and Ag films before annealing are illustrated on the images.

The Au-Ag alloy NPs different Au-Ag ratios fabricated on the same TiO_2 films are shown in the **Figure 3.5**. The size distribution and area coverage of the NPs are very different even with the same total metal thickness. The size of the NPs decreases

gradually with decreasing the Au content. Nanoparticles can't form through annealing if Au content reduce to 0, only Ag content is present. The optical properties, and the photoelectrochemical performances of the AATA with different Au-Ag ratios were also investigated. The measured results are shown in **Figure 3.6**.

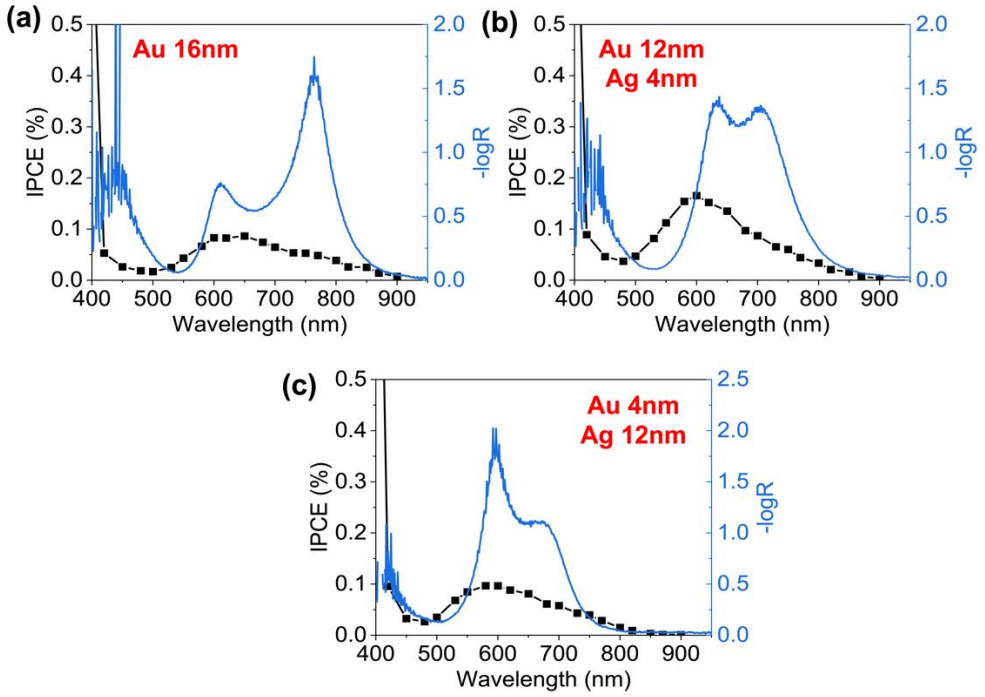

Figure 3.6 IPCE (black dots, left scales) and absorption spectra (blue lines, right scales) of AATA structures with different Au-Ag ratios. (a) Au 16 nm, (b) Au 12 nm, Ag 4 nm, (c) Au 4 nm, Ag 12 nm.

The results of the photoelectrochemical measurements are given in **Figure 3.6**. The IPCE action spectra of AATA electrode with different Au-Ag ratios shows two peaks at about 610 and 750 nm wavelength, which corresponds to the upper and lower branch of the absorption band. At 610 nm, the IPCE of AATA with only Au (deposited Au 16 nm) is ~0.09%, the Au-Ag ratio of 3:1 (deposited Au was 12 nm, Ag was 4 nm) is ~0.19%, and Au-Ag ratio of 1:3 (deposited Au was 4 nm, Ag was 12 nm) is ~0.10%. Those results indicated that the AATA with Au-Ag ratio of 3:1 exhibits higher IPCE.

3.3.2 Au-Ag film Thickness of the Au-Ag alloy NPs

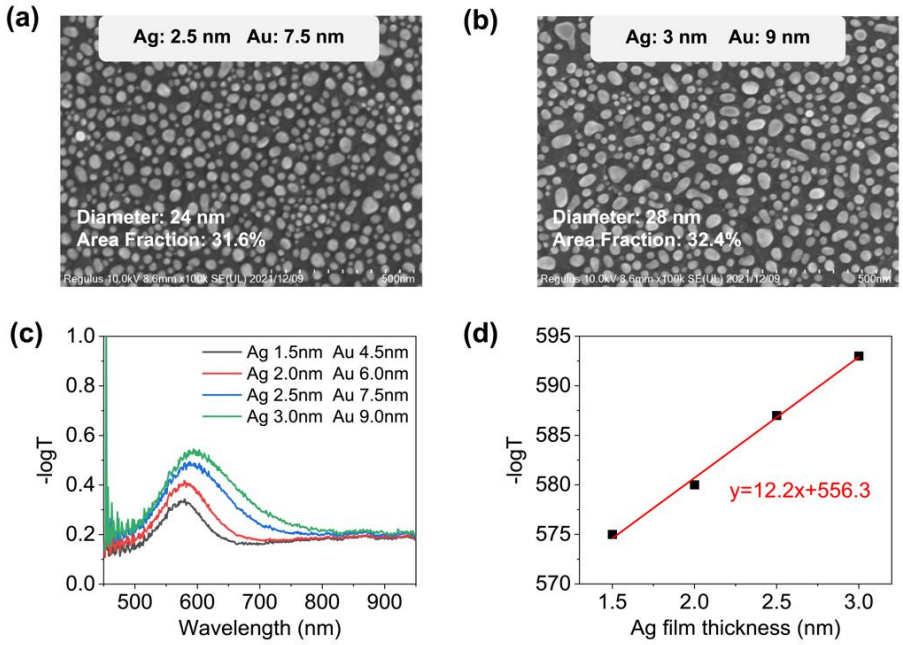

Figure 3.7 (a,b) SEM images of Au-Ag alloy NPs made of different thickness Au and Ag film. The calculated diameters and the area fractions are illustrated in the images. (c) The plasmon band, calculated by -log*T*, of Au-Ag alloy NPs made of different thickness Au and Ag film. (d) Plasmon band wavelength as a function of Ag thickness.

Figure 3.7a and b are the surface morphologies and size distributions of ATAA structures with different Au NPs size prepared with different Au and Ag thicknesses by thermal evaporation. The Au-Ag ratio used here are 3:1. It is clearly observed that a monolayer of Au NPs with a relatively large size is dispersed on the surface of TiO_2 and the size is certainly relevant to the Au/Ag thicknesses. As shown in **Figure 3.7a and b**, 24 nm and 28 nm Au-Ag alloy NP size corresponds to the Au/Ag film thickness of 7.5/2.5 nm and 9/3 nm, 4 n, respectively. The size of Au NPs can be regulated vis changing the thickness of the initial thermal evaporated Au and Ag film.

In order to investigate the optical properties of the fabricated Au-Ag alloy NPs with different sizes, the *T* is measured by PMA. The corresponding plasmon absorption is calculated as -log*T*. The plasmon absorption spectra of Au-Ag alloy NPs with different sizes are shown in **Figure 3.7c**. The plasmon band of Au-Ag alloy NPs

as a function of Ag film thickness are also plotted in **Figure 3.7d**. As expected, the plasmon absorption of Au-Ag alloy NPs exhibit red-shift and a slight increase as the size increases. In addition, since the particle size is one of the key factors affecting the optical properties of Au NPs, the absorption spectra of Au-Ag alloy NPs become wider as the Au NPs size increases.

3.4 Results and Discussions

3.4.1 Characterizations of AATA

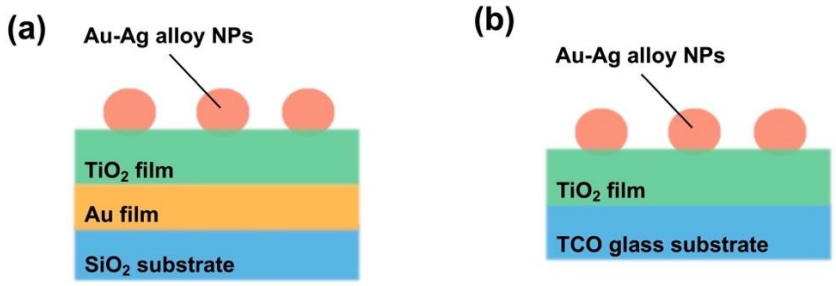

Figure 3.8 Schematic of the Au-Ag alloy NPs/TiO_2/Au-film (AATA) structure (a) and Au-Ag alloy NPs/TiO_2 (AAT) structure (b).

In this study, we successfully fabricated the Au-Ag alloy NPs/TiO_2/Au-film (AATA) structure on a SiO_2 glass for EC-SERS measurements as depicted in the schematic shown in **Figure 3.8a**. To achieve a FP nanocavity with second order in the visible light range, we deposited a 180-nm TiO_2 film on a Au film. This formation is enabled by the reflection phase change at the TiO_2/Au-film interface and the relatively high refractive index of TiO_2 (~2.4 at 600 nm). Subsequently, Au-Ag alloy NPs were fabricated on TiO_2/Au film through the annealing of an Au-Ag multilayer thin film. As a control sample, we also fabricated the Au-Ag alloy NPs/TiO_2 structure (AAT) without the FP nanocavity on high-durability transparent conductive film glass as shown in the **Figure 3.8b**.

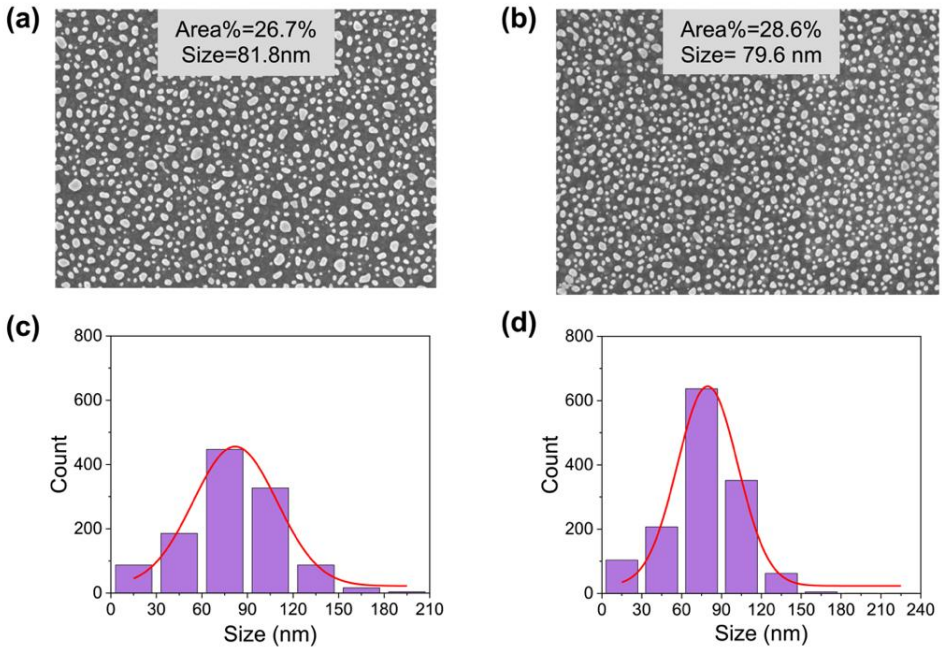

Figure 3.9 (a, b) SEM images of the Au-Ag alloy NPs on AATA (a) ad AAT (b) structures in the top-view. (c, d) Size distributions (histogram and Gaussian fitting) from the SEM images of the Au-Ag alloy NPs on the AATA (c) and AAT (d) structures.

Figure 3.9a and b provide the top-view SEM images of the AATA and AAT structures, where the Au-Ag alloy NPs average size was approximately 80 nm, as indicated in the histogram and the Gaussian fitting shown in **Figure 3.9c and d**.

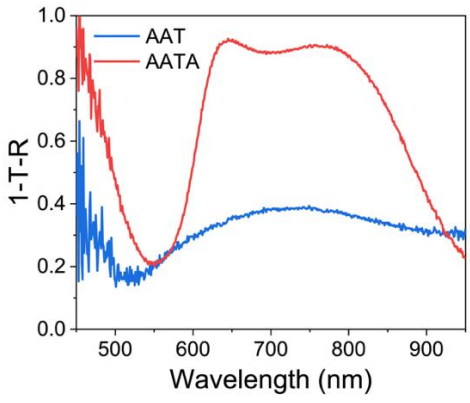

Figure 3.10 The absorption spectra of the AATA and AAT structures.

The absorption spectra of AATA and AAT without a cavity, as presented in **Figure 3.10**, were derived by calculating 1-T-R from the T and R values at different wavelengths. In the case of the AAT structure, a plasmon band was observed around 720 nm, exhibiting an absorption intensity of approximately 0.4. However, the AATA structure displayed distinctive dual bands, with an upper branch at 650 nm and a lower branch at 780 nm. This observation is a direct outcome of the strong coupling between the LSPR of the Au-Ag alloy NPs and the FP nanocavity within the TiO_2/Au film.

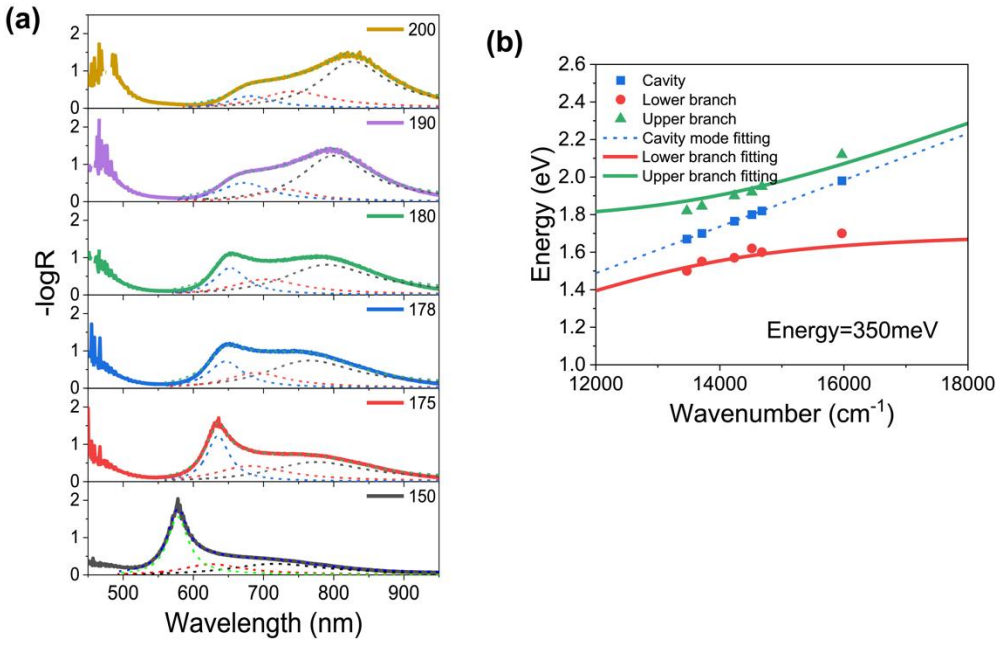

Figure 3.11 (a) Absorption spectra of the AATA structures with series of TiO_2 thicknesses which were calculated by -log(R). The cyan, navy, and green dushed curves indicate the Lorentz fitting of the three components. (b) Dispersion curves of hybrid modes in the AATA structures. The green and red curves represent the fitting of the upper and lower branches, respectively, using a coupled harmonic oscillator model. The energies of the coupling conditions were determined based on the absorption spectra in Panel (a). The blue dashed line shows the cavity mode of a TiO_2/Au film.

Figure 3.11 showcases the absorption spectra and dispersion curve of the AATA structures with 80 nm Au-Ag alloy NPs and varying TiO_2 thicknesses. The calculated

splitting energy was found to be 350 meV, satisfying the conditions for strong coupling. The dispersion curve demonstrated that the cavity mode of the TiO_2/Au film, with a TiO_2 thickness of 180 nm, closely matched the LSPR of the Au-Ag alloy NPs, thereby establishing strong coupling conditions.

3.4.2 Investigation of Water Oxidation Intermediates by EC-SERS Measurements

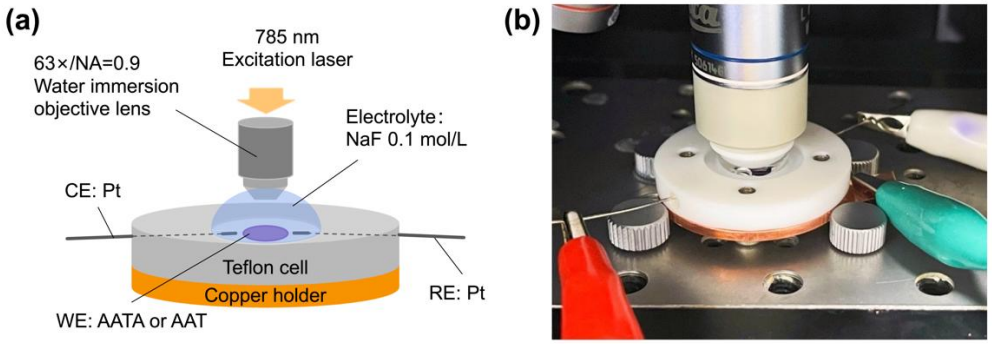

Figure 3.12 (a) Schematic of the photoelectrochemical cell utilized for the EC-SERS measurements. (b) Photograph of the photoelectrochemical cell.

Figure 3.12 illustrates the schematic of the EC-SERS measurement system. To conduct the EC-SERS measurements, a homemade three-electrode reaction cell was utilized, with the AATA or AAT structure serving as the WE and Pt wires acting as the CE and RE. Pt wire is commonly used as a counter and reference electrode due to its reported inertness.[27-31] The EC-SERS measurements were performed in a meticulously designed Teflon cell. The RE and CE were positioned in 1 mm-diameter holes. The use of Pt wire for both the counter and reference electrodes was ideal for this homemade EC-SERS measurement cell due to its advantages in terms of inertness, simplicity, convenience, and ease of operation. In the experiments, a 0.1 mol/L NaF solution was employed as the electrolyte, and it was pre-treated with N_2 gas bubbling for 1 hour to remove dissolved oxygen before testing. NaF does not participate in the chemical reactions, ensuring that water was the only electron donor during the

photoelectrochemical reaction in this system.

The EC-SERS measurements were carried out under a range of electrochemical potentials between -0.2 and 0.9 V vs. Pt, using a λ_{ex} = 785 nm excitation laser. Prior to conducting the EC-SERS measurements, the Ag and its oxide layer were removed from the surface of the Au-Ag alloy NPs through anodic oxidation reaction at an applied potential of 0.5 V vs. Ag/AgCl and light irradiation of 620 nm for 2 hours. This step was taken to eliminate any effects caused by the Ag oxidation reaction on the water oxidation, following the method reported in our previous study.[18]

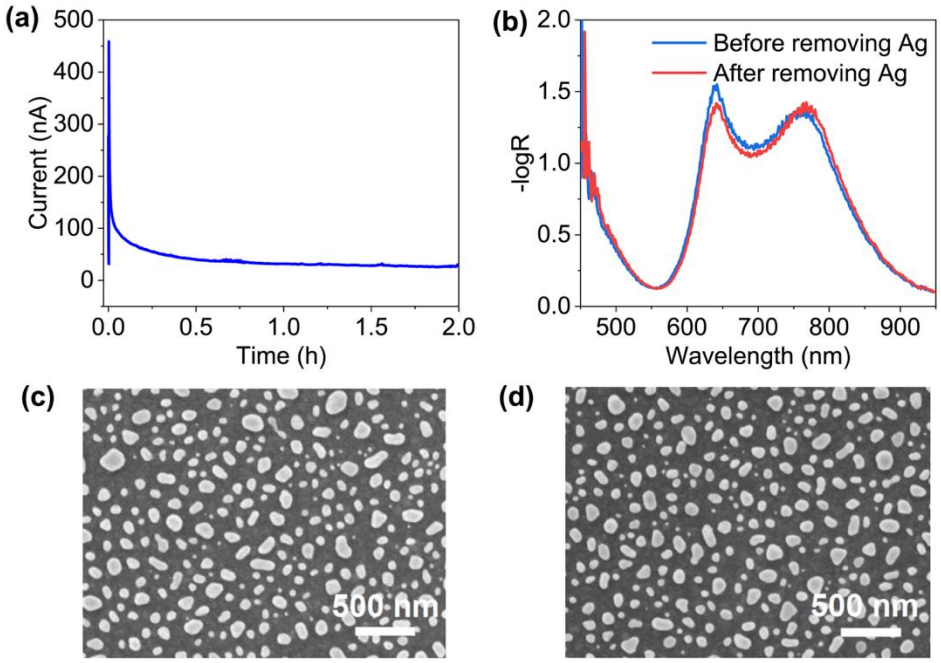

Figure 3.13 (a) I-t curve of the photoelectrochemical measurements during the Ag-removing reaction process. (b) Absorption spectra of AATA structure before and after removing the Ag on the surface of Au-Ag alloy NPs. (c, d) SEM images of Au-Ag alloy NPs on the AATA electrode before (c) and after (d) removing the Ag on the surface of Au-Ag alloy NPs.

The effectiveness of the Ag removal was confirmed by the nearly constant photocurrent observed in the I-t curve after 2 hours (**Figure 3.13a**), indicating the successful completion of the oxidative elution of Ag on the surface and the establishment of a stable water oxidation reaction. Moreover, the comparable

absorption spectra (**Figure 3.13b**) and the particle size of the Au-Ag alloy NPs (**Figure 3.13c, d**) of AATA before and after Ag removal suggest that the Au in the Au-Ag alloy NPs remained unaffected by the Ag removal process. This is consistent with the findings that Ag atoms within the Au-Ag alloy NPs, where the proportion of Ag is less than 30%, are not exposed to the outside during electrochemical Ag and Ag oxide removal, thus stabilizing the Au-Ag alloy NPs against oxidation reactions.

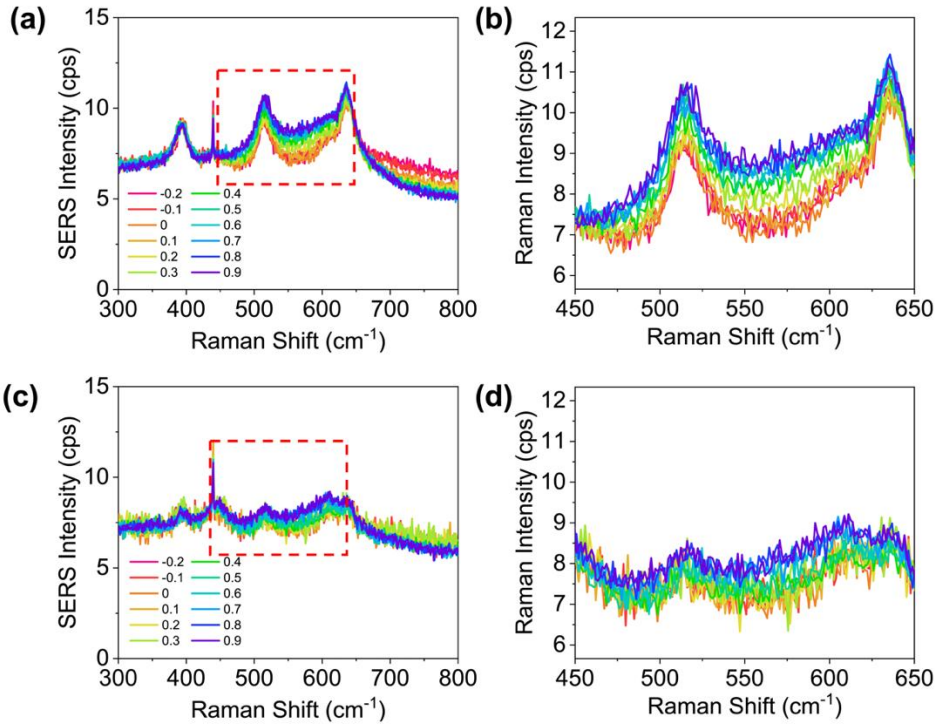

Figure 3.14 (a) Raman spectra collected on the AATA and AAT electrodes under applied potentials ranging from -0.2 to 0.9 V vs. Pt. For the AATA electrode, the excitation laser used had a wavelength of 785 nm and a power of 3 μW, while for the AAT electrode, the excitation laser had the same wavelength but a higher power of 30 μW.

EC-SERS measurements were conducted on the AATA and AAT electrodes under applied potentials ranging from -0.2 to 0.9 V vs. Pt, allowing us to obtain potential-dependent SERS spectra. As shown in **Figure 3.14**, the SERS spectra obtained from the EC-SERS measurements on both AATA and AAT electrodes exhibited characteristic Raman features of TiO_2, which were clearly observed. To

maintain the background continuum of the SERS spectra at a consistent level, the power of the excitation laser used on the AATA electrode was set to be 10 times lower than that used on the AAT electrode, specifically 3 μW and 30 μW for AATA and AAT, respectively. The potentials were applied sequentially from -0.2 to 0.9 V vs. Pt, with a step size of 0.1 V. Following each EC-SERS measurement at a specific potential, an electrochemical potential of -0.2 V vs. Pt was applied for 3 minutes to ensure the removal of any potential oxidation intermediates that might have been absorbed on the surface. The collected spectra from both AATA and AAT electrodes exhibited distinct Raman peaks characteristic of TiO_2, and the detailed assignments of these Raman peaks can be found in **Table 3.1**.[32]

Table 3.1. Assignments of Raman peaks.

Raman shift (cm^{-1})	Observed Raman shift	Assignment
198 (Anatase)	196	(Eg) O-Ti-O bending
398 (Anatase)	395	(B1g) O-Ti-O bending
448 (Rutile)	443	(Eg) O-Ti-O bending
515 (Anatase)	514	(A1g, B1g) Ti-O bond stretching
612 (Rutile)	610	(A1g) Ti-O bond stretching
640 (Anatase)	636	(Eg) Ti-O bond stretching
~700 (Rutile)	690	Combination featrue appeared only in small crystallite sizes*

As the potential was varied from negative to positive, a distinct broad band at approximately 500~600 cm^{-1} emerged in the Raman spectra (**Figure 3.14**). To mitigate the interference from TiO_2 SERS signals and focus on the spectral changes of the intermediate SERS signals related to water oxidation, differential SERS spectra at various potentials were utilized. These spectra were obtained by subtracting the reference spectrum measured at -0.2 V vs. Pt from the spectra recorded at the series of potentials on both AATA and AAT electrodes.

To demonstrate the stability of the SERS signals on the AATA and AAT electrodes,

the EC-SERS measurements were performed three times each on AATA and AAT electrodes under the same condition to collect the Raman spectra.

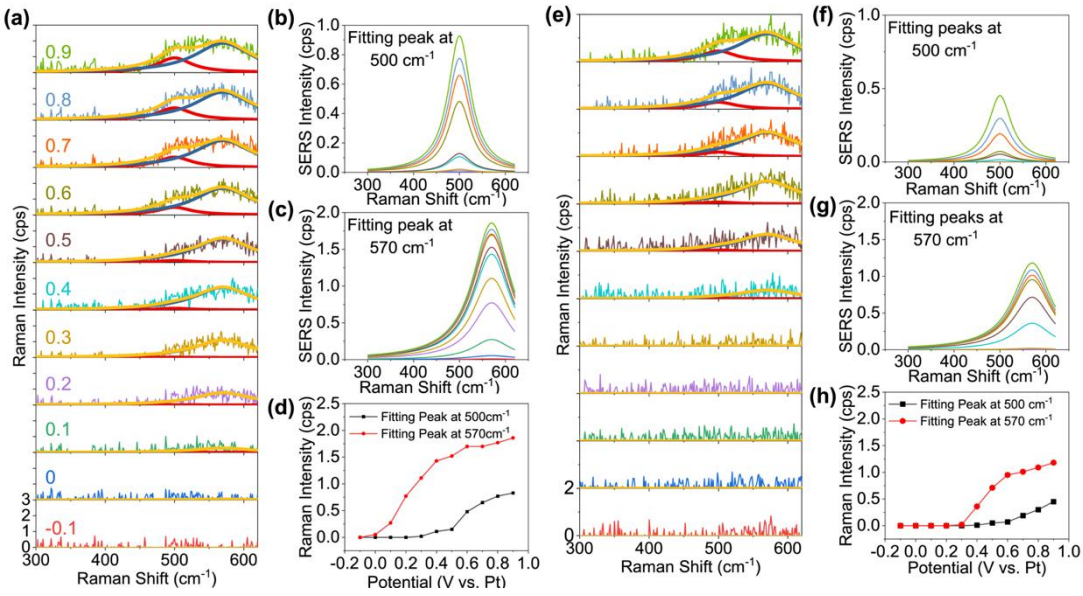

Figure 3.15 (a) Differential Raman spectra of AATA at electrochemical potentials from -0.1 to 0.9 V vs. Pt with a step of 0.1 V vs. Pt calculated from the Raman spectra in Figure 3.11a. The power of the excitation laser was 3 μW. (b, c) The Lorentz fitting spectra of Raman peak at 500 and 570 cm^{-1}, respectively, in the differential Raman spectra of AATA. (d) Potential-dependent Raman intensity of AATA calculated from (b) and (c). (e) Differential Raman spectra of AAT at electrochemical potentials from -0.1 to 0.9 V vs. Pt with a step of 0.1 V vs. Pt calculated from the Raman spectra in Figure 3.11c. The power of the excitation laser was 30 μW. (f, g) The Lorentz fitting spectra of Raman peak at 500 and 570 cm^{-1}, respectively, in the differential Raman spectra of AAT. (h) Potential-dependent Raman intensity of AATA calculated from (f) and (g).

Figure 3.15a and e exhibit the differential SERS spectra collected on AATA and AAT at series of potentials ranging from -0.1 to 0.9 V vs. Pt with a step size of 0.1 V. The differential SERS spectra acquired on AATA exhibited a broad signal centered at 570 cm^{-1} and a shoulder band around 500 cm^{-1} as the potential was swept from negative to positive values. Prior research has documented that the Raman bands at 460 and 572 cm^{-1} correspond to the $Au_4*(OH)_2$ hydrate and gold oxyhydroxide AuOOH, respectively, which are essential intermediates in water oxidation processes.

Since the Ag and its oxide layer on the surface of the Au-Ag alloy NPs were removed before the electrochemical measurements, the electron acceptor in the photoelectrochemical water oxidation reaction is the Au present on the surface of the Au-Ag alloy NPs. Therefore, it is plausible to attribute the observed broad bands at 500 and 570 cm^{-1} to Au oxidation intermediates.

The band centered at 570 cm^{-1} corresponds to the Au-O vibration of the gold oxyhydroxide AuOOH, which constitutes the main intermediate in plasmon-induced water oxidation under neutral conditions. Additionally, the SERS signal at approximately 500 cm^{-1} is associated with ν(Au-OH), which can be attributed to the $Au_4*(OH)_2$ hydrate formed when OH^- species adsorb on the Au surface during electrochemical water oxidation on Au. The slight shifts in the SERS peaks compared to the reported signals are likely due to the presence of Au-Ag alloy NPs. Although the Ag on the surface of the Au-Ag alloy was removed, the Ag atoms situated one or several atomic layers below the surface of the Au-Ag alloy might influence the vibration of the Au-O and Au-OH stretching modes, leading to Raman band shifts.

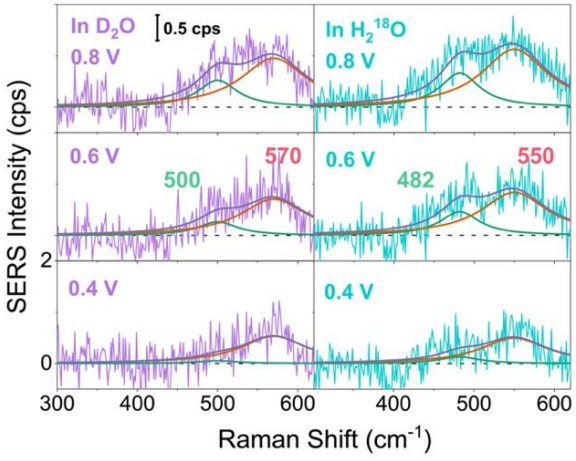

Figure 3.16 (a) The isotope effect observed in the differential SERS spectra collected on AATA at applied potentials of 0.4, 0.6, and 0.8 V vs. Pt in an electrolyte solution containing 0.1 mol/L NaF. The spectra are shown for both D_2O (purple lines) and $H_2{}^{18}O$ (blue lines). Additionally, multipeak Lorentzian fittings of the SERS signals were also applied and superimposed on the spectra.

To gain further insight into the chemical identity of the species associated with the

Raman bands at 500 and 570 cm^{-1}, EC-SERS measurements were conducted in 0.1 mol/L NaF solutions using D_2O- and ^{18}O-enriched (98%) water. **Figure 3.16** displays the EC-SERS spectra for water oxidation on the AATA electrode in D_2O and ^{18}O water at potentials of 0.4, 0.6, and 0.8 V vs. Pt. As anticipated, the Raman bands at 570 and 500 cm^{-1}, attributed to the ν(Au-O) and ν(Au-OH) vibrations, respectively, exhibited lower frequencies when using ^{18}O water due to the isotope effect. The isotope frequency shifts were approximately 3.5% and 3.6% for the signals ascribed to ν(Au-O) at 570 cm^{-1} and ν(Au-OH) at 500 cm^{-1}, respectively. However, no significant shift in these two bands was observed when using D_2O. The isotopic effects of oxygen-18 provided evidence that the Raman bands at 570 and 500 cm^{-1} correspond to the stretching vibrations of the ν(Au-O) and ν(Au-OH) vibrations, respectively.

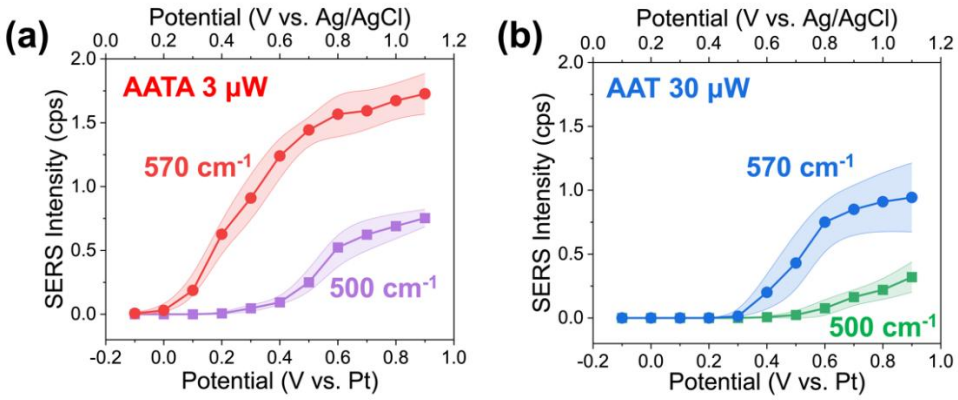

Figure 3.17 Potential-dependent SERS intensity of ν(Au-O) at 570 cm^{-1} (solid dots) and ν(Au-OH) at 500 cm^{-1} (solid squares) for both AATA (a) and AAT (b) electrodes. The EC-SERS measurements were conducted three times under the same experimental conditions, and the colored areas represent the error bars from these measurements. The excitation laser intensities used for AATA and AAT were 3 and 30 μW, respectively.

For quantitative analysis of the SERS signals, we employed two Lorentzian peaks centered at 500 and 570 cm^{-1} to fit the differential SERS spectra, representing ν(Au-OH) and ν(Au-O) vibrations, respectively. **Figure 3.17** present the

potential-dependent differential SERS peak intensities for the AATA and AAT electrodes, illustrating the effect of the electrochemical potential on the ν(Au-OH) and ν(Au-O) bands. The data were obtained from three repetitions of the EC-SERS measurements under the same experimental conditions, providing the mean intensity values and error bars. Remarkably, the SERS intensities of the ν(Au-OH) and ν(Au-O) bands on the AATA electrode were approximately 2 times higher than those on the AAT electrode, despite the excitation laser power being 10 times lower on AATA. This substantial enhancement in the SERS intensity on AATA can be attributed to the exceptional near-field enhancement resulting from the strong coupling between the LSPR of the Au-Ag alloy NPs and the nanocavity in the TiO_2/Au-film.

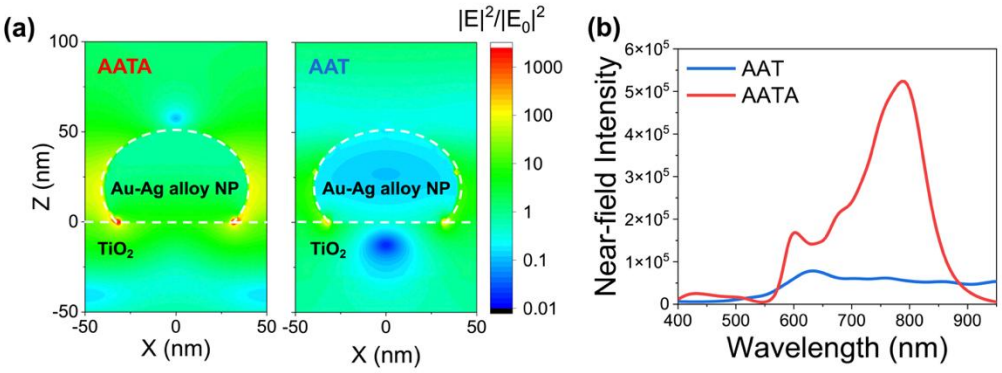

Figure 3.18 (a) The cross-sectional near-field distribution on the AATA and AAT structures calculated by finite-difference time-domain (FDTD) simulations. (b) Integrated near-field enhancement on the AATA and AAT substrates (obtained by integrating the 1.0 nm region at the surface of the substrates).

Figure 3.18 exhibits the cross-section near-field distribution close to the Au-Ag alloy NPs on both the AATA and AAT structures, which was calculated using the FDTD method. The regions with maximum near-field intensity, commonly referred to as "hot spots", are observed at the interfacial boundary corner between the NPs and TiO_2. Importantly, the near-field enhancement of AATA is significantly more pronounced than that of AAT.

The SERS signal associated with the ν(Au-O) vibration at 570 cm^{-1} was observed

at an applied potential of approximately 0.1 V vs. Pt for the AATA electrode. Upon tuning the potential in the positive direction within the range of 0 to 0.5 V vs. Pt, the intensity of the SERS signal increased and eventually reached a saturation point at higher potentials. Furthermore, the SERS signal corresponding to the ν(Au-OH) vibration at 500 cm^{-1} was detected at around 0.5 V vs. Pt and exhibited a gradual enhancement with increasing positive potentials.

In contrast, for the AAT electrode, the SERS signal of the ν(Au-O) at 570 cm^{-1} became noticeable only after reaching a potential of 0.4 V vs. Pt, which was considerably more positive than the onset potential observed on the AATA electrode. Similarly, the SERS signal associated with the ν(Au-OH) vibration at 500 cm^{-1} on the AAT electrode appeared at approximately 0.5~0.6 V vs. Pt, closely resembling the onset potential observed on the AATA electrode. In this study, the onset potential of the Raman bands was defined as the electrochemical potential at which the SERS intensity exceeded 0.1 cps. **Figure 3.17** illustrate that the ν(Au-O) vibration at 570 cm^{-1} exhibited an onset potential of 0.1 V vs. Pt on the AATA electrode, while on the AAT electrode, the onset potential was 0.4 V vs. Pt. The more negative onset potential of the SERS signal of the ν(Au-O) vibration on AATA compared to AAT indicates that efficient electron/hole separation occurs on the AATA electrode. A comprehensive analysis of this observation will be provided in the subsequent sections.

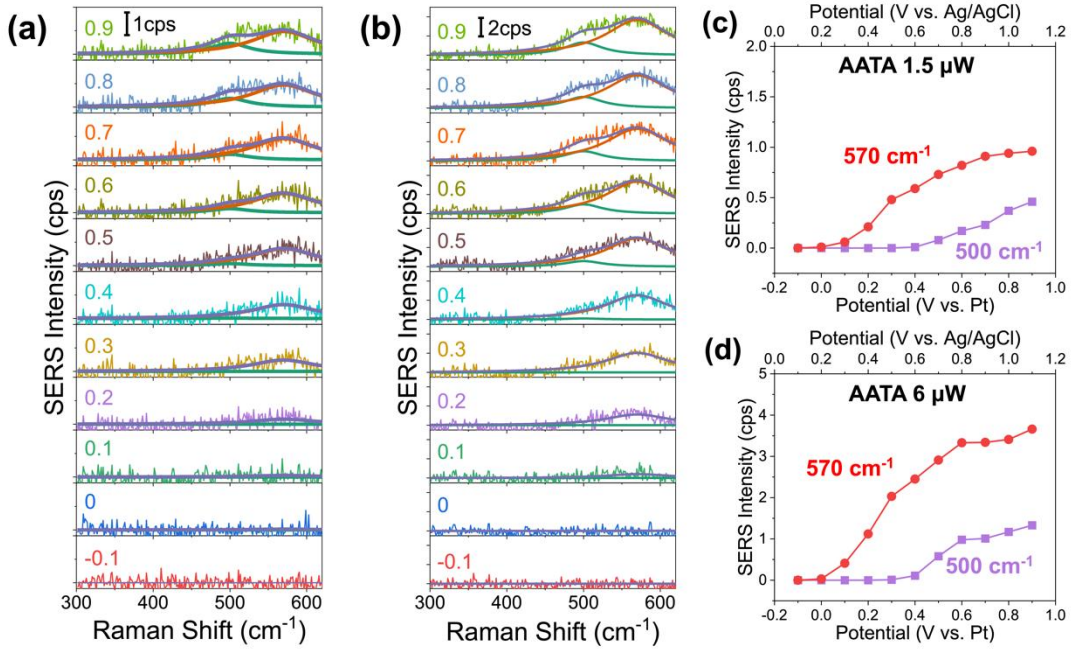

Figure 3.19 (a, b) Differential Raman spectra of AATA under excitation laser power of 1.5 (a) and 6 μW (b) at electrochemical potentials from -0.1 to 0.9 V vs. Pt with a step of 0.1 V vs. Pt. (c, d) Potential-dependent SERS intensities of peak at 570 cm^{-1} (red dots) and 500 cm^{-1} (purple squares) on AATA electrode under irradiation of 1.5 and 6 μW laser.

To account for the variation in laser powers used in the previous experiments, we conducted further investigations on the onset potentials of the SERS signals related to ν(Au-O) and ν(Au-OH) on the AATA electrode at different excitation laser powers. Accordingly, EC-SERS measurements were performed on AATA using excitation laser intensities of 1.5 and 6 μW. **Figure 3.19a and b** displays the differential SERS spectra obtained on the AATA electrode under various applied electrochemical potentials ranging from -0.2 to 0.9 V vs. Pt. **Figure 3.19c and d** depict the potential-dependent SERS intensity of ν(Au-O) at 570 cm^{-1} and ν(Au-OH) at 500 cm^{-1} on the AATA electrode, covering a range of electrochemical potentials from -0.1 to 0.9 V vs. Pt. Despite the increase in SERS intensity for both ν(Au-O) and ν(Au-OH) as the excitation laser power was raised, the onset potentials of ν(Au-O) and ν(Au-OH) remained consistent at 0.1 and 0.5~0.6 V vs. Pt, respectively.

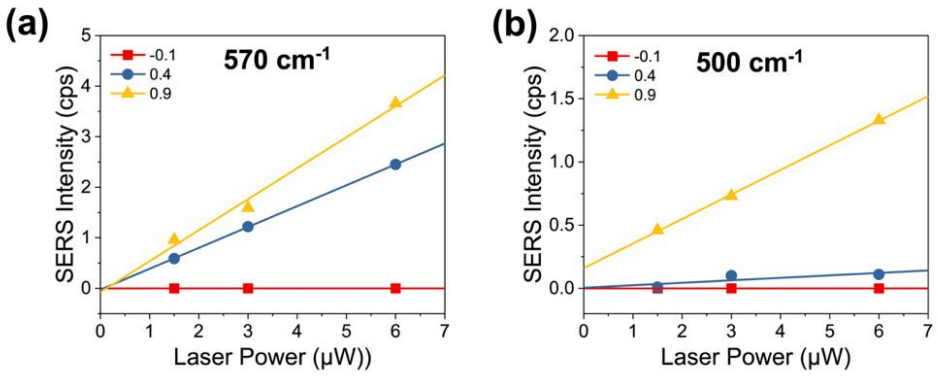

Figure 3.20 (a, b) Laser power-dependent SERS intensities of ν(Au-O) at 570 cm^{-1} and ν(Au-OH) at 500 cm^{-1} on the AATA electrode. The electrochemical potentials of -0.1, 0.4 and 0.9 V vs. Pt are shown by red squires, blue circles, and yellow triangles. The solid lines are the linear fittings of the SERS intensity.

Figure 3.20 displays the SERS intensity at different laser powers along with the corresponding linear fitting lines. The linear fitting indicated that no SERS signals for ν(Au-O) at 570 cm^{-1} were detected when the laser power was 0, signifying that plasmon-induced water oxidation did not occur in the absence of light irradiation. In contrast, the SERS signal of ν(Au-OH) at 500 cm^{-1} was present at an applied electrochemical potential of 0.9 V vs. Pt, even with the laser power set to 0. This finding suggests that ν(Au-OH) was produced by electrochemical water oxidation at a positive applied potential but not by photoinduced water oxidation.

3.4.3 Photoelectrochemical Performance of AATA

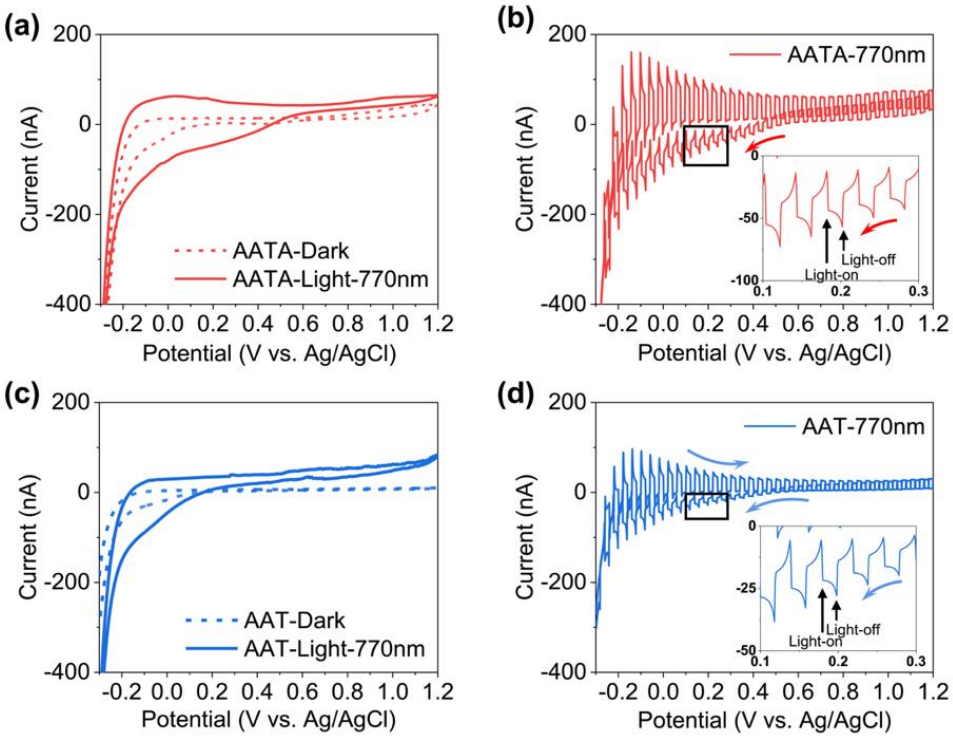

Figure 3.21 (a) CV curves of the AATA photoelectrode obtained under dark conditions and under 770 ± 7.5 nm light irradiation. (b) Chopping CV curves of the AATA photoelectrode under 770 ± 7.5 nm light irradiation (chopping every 2 seconds, within the range between -0.3 and 1.2 V vs. Ag/AgCl). (c) CV curves of the AAT photoelectrode obtained under dark conditions and under 770 ± 7.5 nm light irradiation. (d) Chopping CV curves of the AAT photoelectrode under 770 ± 7.5 nm light irradiation (chopping every 2 seconds, within the range between -0.3 and 1.2 V vs. Ag/AgCl). In all cases, the electrolyte used was a 0.1 mol/L NaF solution, and the scan rate was 0.01 V/s.

Figure 3.21 illustrates the cyclic voltammetry (CV) curves of the AATA and AAT photoelectrodes under dark conditions (black lines) and under continuous or chopped light irradiation with a wavelength of 770 ± 7.5 nm (AATA in red, AAT in blue). It is important to note that Au oxidation might occur under light irradiation, as evidenced by the comparison of the CV spectra in the dark and under light irradiation shown in **Figure 3.21**. At an applied potential of -0.2 V vs. Pt, the reduction of oxidized Au

took place. Consequently, the SERS spectra recorded at -0.2 V vs. Pt were employed as the reference spectra, as no Au oxidation intermediates were expected at this applied potential.

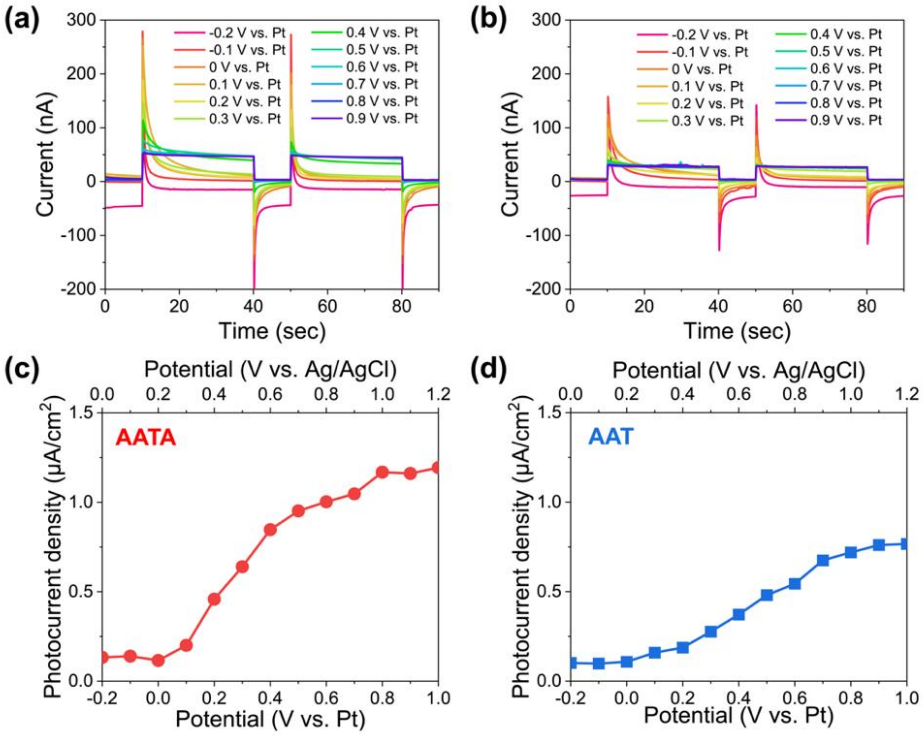

Figure 3.22 (a, b) Current-time (I-t) curves recorded on the AATA (a) and AAT (b) electrodes with series of applied potentials under NIR light (770 ± 7.5 nm) irradiation. The intensity of the light was 1.2 mW. (c, d) Potential-dependent photocurrent density of the AATA (c) and AAT (d) electrodes under NIR light (770 ± 7.5 nm) irradiation. The intensity of the light was 1.2 mW.

The photoelectrochemical measurements were conducted using a three-electrode system with AATA or AAT as the working electrode (WE), a Ag/AgCl electrode as the reference electrode (RE), and a 0.1 mol/L NaF solution as the supporting electrolyte. **Figure 3.22a and b** illustrated the time-dependent current (I-t) curves obtained with the AATA and AAT electrodes. The photocurrent values were determined by calculating the difference between the light-on current and the light-off current. **Figure 3.22c and d** show the potential-dependent photocurrent density of the AATA and AAT electrodes under 770 ± 7.5 nm light irradiation. To provide a clearer

perspective, we converted the potential unit from “V vs. Pt” to “V vs. Ag/AgCl”, which is a more commonly used reference electrode. After measuring the I-V curves using Pt and Ag/AgCl as reference electrodes, respectively, we observed that the electrochemical potential using Pt as the reference electrode exhibited an approximately 0.2 V negative shift compared to that using Ag/AgCl as the reference electrode under the same measurement conditions. To convert the electrochemical potential from “V vs. Pt” to “V vs. Ag/AgCl”, we applied the following formula:

$$\mathrm{E(vs.\,Ag/AgCl)} = \mathrm{E(vs.\,Pt)} + 0.2\ \mathrm{V} \tag{3.2}$$

where $\mathrm{E(vs.\,Pt)}$ is the electrochemical potential measured with Pt as the reference electrode, and $\mathrm{E(vs.\,Ag/AgCl)}$ is the corresponding potential when using Ag/AgCl as the reference electrode. This conversion accounts for the approximately 0.2 V negative shift observed between the two reference electrodes in the same measurement conditions.

It can be seen from the **Figure 3.22c and d**, the onset potentials of the photocurrent observed on the AATA and AAT electrodes were approximately 0.3 V vs. Ag/AgCl (equivalent to 0.1 V vs. Pt) and 0.5 V vs. Ag/AgCl (equivalent to 0.3 V vs. Pt), respectively. These values are consistent with the onset potentials of the SERS signals associated with the ν(Au-O) vibration.

3.4.4 Mechanism of Plasmon-Nanocavity Coupling Enhancement Effect

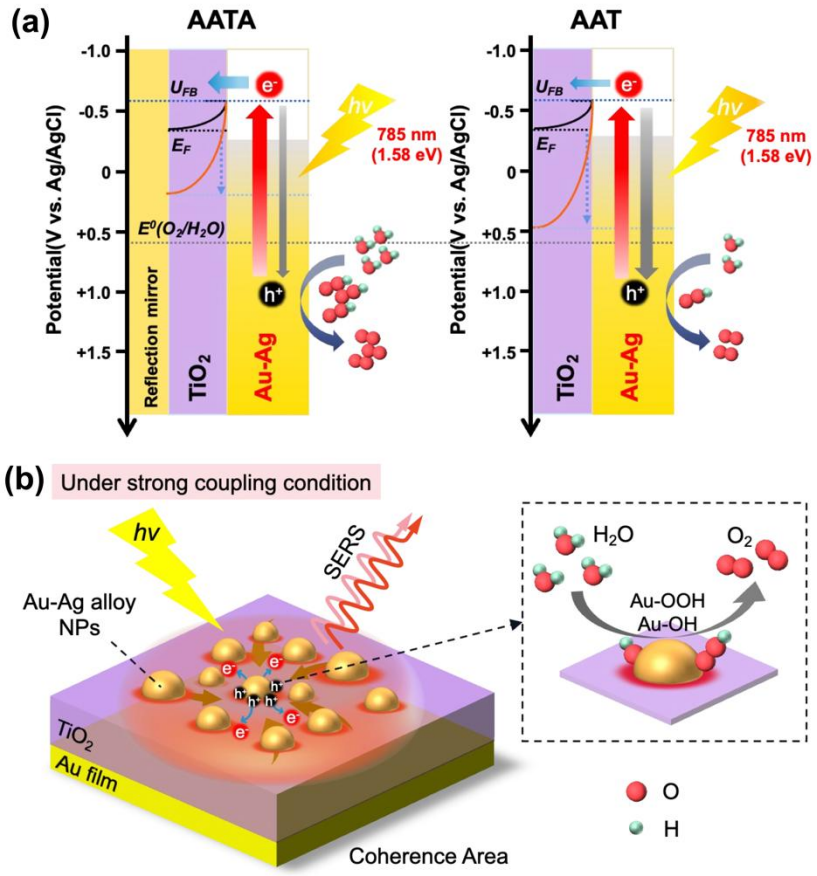

Figure 3.23 (a) Energy diagram illustrating the AATA and AAT electrodes in a pH 7 electrolyte under LSPR excitation from a 785 nm laser. In this diagram, e^- represents electrons, and h^+ indicates holes. U_{FB} denotes the flat band potential of the TiO_2 film, which is calculated to be -0.58 V vs. Ag/AgCl. E_F corresponds to the Fermi level. $E^0(O_2/H_2O)$ represents the oxidation potential of water, which is calculated to be +0.62 V vs. Ag/AgCl under neutral conditions (pH=7).[21] (b) Schematic representation of the plasmon-induced water oxidation mechanism occurred on the AATA electrode under the strong coupling condition.

Figure 3.23a illustrates the energy diagram of the AATA and AAT electrodes during photoexcited water oxidation. When exposed to light, the photoexcited hot electrons acquire sufficient energy to transfer over the interfacial Schottky barrier and enter the conduction band of TiO_2, while the remaining holes are captured at the

surface states near the interfacial boundary between the Au-Ag alloy NPs and TiO_2. At applied potentials more negative than 0.1 V vs. Pt for AATA and 0.4 V vs. Pt for AAT, electron-hole recombination prevails, resulting in only a slight photocurrent and no observable EC-SERS signal from the Au-O vibration. Conversely, at applied potentials more positive than 0.1 V vs. Pt for AATA and 0.4 V vs. Pt for AAT, effective charge separation occurs, and the holes exhibit an extended lifetime for water molecule oxidation and oxygen evolution. Notably, the EC-SERS and photocurrent measurements indicate that the water oxidation efficiency on the AATA electrode is significantly higher than that on the AAT electrode.

The superior water oxidation efficiency observed on the AATA electrode can be attributed to the strong coupling between the LSPR of the Au-Ag NPs and the nanocavity mode in the TiO_2 layer, as depicted in the schematic of **Figure 3.23b**. Under this strong coupling condition, quantum coherence between the Au-Ag alloy NPs is induced through the nanocavity, as previously reported in our earlier study. The quantum coherence leads to the formation of a coherence area where energy is coherently shared. When certain Au-Ag NPs with faster damping characteristics is present within this coherence area, the generation of electron-hole pairs at those specific NPs is promoted. Consequently, more holes accumulate at the reaction sites of these faster damping Au-Ag NPs. As the water oxidation is a four-electron chemical reaction, the accumulation of additional holes will contribute to a considerable enhancement of the water oxidation process.

Furthermore, the AATA structure exhibits a much stronger near-field intensity compared to AAT, resulting from the strong coupling between the LSPR and FP nanocavity mode. This enhanced near-field intensity and increased hole density facilitate efficient electron transfer and SERS enhancement. As a result, the onset potential of ν(Au-O) on the AATA electrode is assumed to be more negative than that on the AAT electrode. Overall, the combined effects of quantum coherence, enhanced near-field intensity, and increased hole density contribute to the exceptional water oxidation performance of the AATA electrode.

As the applied potential increases, the Fermi level undergoes a downshift to a

more positive potential, resulting in a continuous injection of hot electrons into the conduction band of TiO_2. Consequently, the height of the interfacial Schottky barrier increases, making it more challenging for the electrons to transfer over the Schottky barrier and reach the conduction band of TiO_2 under a more positive applied potential. However, at the same time, the charge separation efficiency improves with increasing applied potential, leading to enhanced water oxidation. This trade-off between electron transfer and charge separation efficiencies causes the trend of EC-SERS intensity to saturate when the applied potential exceeds approximately +0.7 V vs. Ag/AgCl, as depicted in **Figure 3.17a and b**.

Moreover, as the potential increases to around 0.5~0.6 V vs. Pt, electrochemical oxidation of water starts occurring at the interface of the Au-Ag alloy NP. In the first step of this potential-induced oxidation, OH^- is reversibly absorbed from the space charge layer region onto the surface of the Au-Ag alloy NP, resulting in the formation of the $Au_4*(OH)_2$ hydrate. This leads to distinct SERS signals of the ν(Au-OH) vibration at 500 cm^{-1}. The potential-induced oxidation depends only on the electrochemical potential, which causes the same onset potential for the ν(Au-OH) vibration on both the AATA and AAT electrodes. However, the EC-SERS intensity trend is noticeably different between the two electrodes due to the influence of strong coupling and enhanced near-field intensity in the AATA structure, as discussed earlier.

3.5 Conclusions

In conclusion, in this chapter the optimized plasmon-nanocavity strong coupling structure, which consist of a monolayer of Au-Ag alloy NPs and a TiO_2/Au film nanocavity, was used as the photoelectrode to investigate the impact of plasmon-nanocavity strong coupling on the plasmon-induced water oxidation reaction by means of *in situ* EC-SERS measurements. The SERS intensities of ν(Au-O) and ν(Au-OH), which represent the reaction intermediates of water oxidation, were systematically examined over a wide range of electrochemical potentials. Compared to the AAT structure without any FP nanocavities, the AATA photoelectrode

demonstrated a higher SERS intensity during *in situ* EC-SERS measurements, primarily due to its significantly enhanced near-field intensity.

More importantly, the SERS signals of ν(Au-O) related to AuOOH, the intermediate of plasmon-induced water oxidation on the AATA photoelectrode exhibited a more negative onset potential compared to the AAT, indicating more efficient charge separation on the AATA structure, which facilitates the water oxidation reaction. This enhanced water oxidation efficiency on AATA is likely attributed to the quantum coherence between the Au-Ag alloy NPs through the nanocavity, leading to the accumulation of a large number of holes. Furthermore, the onset potentials of ν(Au-OH) related to $Au_4*(OH)_2$, one of the intermediates of potential-induced water oxidation, showed nearly identical values on both the AATA and AAT electrodes.

Based on our *in situ* EC-SERS measurements, we concluded that plasmon-induced water oxidation is facilitated by the quantum coherence effect under LSPR-nanocavity strong coupling. This study provides valuable insights into the development of efficient plasmon-induced photochemical reactions, contributing to advancements in renewable energy technologies. By harnessing the potential of strong coupling between plasmons and nanocavities, we can pave the way for the efficient utilization of renewable energy sources and foster progress in sustainable energy applications.

3.6 References

[1] Y. Tian, T. Tatsuma, *J. Am. Chem. Soc.* **2005**, 127, 7632.

[2] D. Gogoi, A. Namdeo, A. K. Golder, N. R. Peela, *International Journal of Hydrogen Energy* **2020**, 45, 2729.

[3] W. Ye, R. Long, H. Huang, Y. Xiong, *J. Mater. Chem. C* **2017**, 5, 1008.

[4] Y. Tian, T. Tatsuma, *Chem. Commun.* **2004**, 1810.

[5] Z. Zhang, L. Zhang, M. N. Hedhili, H. Zhang, P. Wang, *Nano Lett.* **2013**, 13, 14.

[6] S. Linic, P. Christopher, D. B. Ingram, *Nature Mater* **2011**, 10, 911.

[7] X. Shi, K. Ueno, T. Oshikiri, Q. Sun, K. Sasaki, H. Misawa, *Nature Nanotech* **2018**, 13, 953.

[8] Y. Cao, T. Oshikiri, X. Shi, K. Ueno, J. Li, H. Misawa, *ChemNanoMat* **2019**, 5, 1008.

[9] X. Zang, X. Shi, T. Oshikiri, K. Ueno, Y. Sunaba, K. Sasaki, H. Misawa, *J. Phys. Chem. C* **2021**, 125, 19880.

[10] Y.-E. Liu, X. Shi, T. Yokoyama, S. Inoue, Y. Sunaba, T. Oshikiri, Q. Sun, M. Tamura, H. Ishihara, K. Sasaki, H. Misawa, *ACS Nano* **2023**, 17, 8315.

[11] D.-Y. Wu, J.-F. Li, B. Ren, Z.-Q. Tian, *Chem. Soc. Rev.* **2008**, 37, 1025.

[12] X. Li, H. Minamimoto, S. Yasuda, K. Murakoshi, in ACS Symposium Series, ed. by Yukihiro Ozaki, George C. Schatz, Duncan Graham, Tamitake Itoh, *American Chemical Society, Washington, DC*, **2016**, Vol. 1245, pp. 163–180.

[13] X. Li, H. Minamimoto, K. Murakoshi, *Spectrochimica Acta Part A: Molecular and Biomolecular Spectroscopy* **2018**, 197, 244.

[14] Y. Wang, H. Minamimoto, R. Zhou, K. Murakoshi, *J. Phys. Chem. C* **2021**, 125, 1754.

[15] X. Shi, X. Li, T. Toda, T. Oshikiri, K. Ueno, K. Suzuki, K. Murakoshi, H. Misawa, ACS Appl. *Energy Mater.* **2020**, 3, 5675.

[16] K. Suzuki, X. Li, Y. Wang, F. Nagasawa, K. Murakoshi, *ACS Energy Lett.* **2020**, 5, 1252.

[17] O. Diaz-Morales, F. Calle-Vallejo, C. De Munck, M. T. M. Koper, *Chem. Sci.* **2013**, 4, 2334.

[18] Y. Suganami, T. Oshikiri, X. Shi, H. Misawa, *Angew. Chem. Int. Ed.* **2021**, 60, 18438.

[19] P. B. Johnson, R. W. Christy, *Phys. Rev. B* **1972**, 6, 4370.

[20] J. R. DeVore, *J. Opt. Soc. Am.* **1951**, 41, 416.

[21] R. Thomas, A. Thomas, S. Pullanchery, L. Joseph, S. M. Somasundaran, R. S. Swathi, S. K. Gray, K. G. Thomas, *ACS Nano* **2018**, 12, 402.

[22] Y. Ohko, T. Tatsuma, T. Fujii, K. Naoi, C. Niwa, Y. Kubota, A. Fujishima, *Nature Mater* **2003**, 2, 29.

[23] S. Link, M. A. El-Sayed, *J. Phys. Chem. B* **1999**, 103, 8410.

[24] M. Valenti, A. Venugopal, D. Tordera, M. P. Jonsson, G. Biskos, A. Schmidt-Ott, W. A. Smith, *ACS Photonics* **2017**, 4, 1146.

[25] C. Gao, Y. Hu, M. Wang, M. Chi, Y. Yin, *J. Am. Chem. Soc.* **2014**, 136, 7474.

[26] D. Fologea, B. Ledden, D. S. McNabb, J. Li, *Applied Physics Letters* **2007**, 91, 053901.

[27] J. Lee, N. Jäckel, D. Kim, M. Widmaier, S. Sathyamoorthi, P. Srimuk, C. Kim, S. Fleischmann, M. Zeiger, V. Presser, *Electrochimica Acta* **2016**, 222, 1800.

[28] B. K. K. Kasem, S. Jones, *platin met rev* **2008**, 52, 100.

[29] J. Solla-Gullón, A. Aldaz, J. Clavilier, *Electrochimica Acta* **2013**, 87, 669.

[30] M. Tian, C. Cousins, D. Beauchemin, Y. Furuya, A. Ohma, G. Jerkiewicz, *ACS Catal.* **2016**, 6, 5108.

[31] G. Jerkiewicz, *ACS Catal.* **2022**, 12, 2661.

[32] T. Ohsaka, F. Izumi, Y. Fujiki, *J. Raman Spectrosc.* **1978**, 7, 321.

Chapter 4 Conclusions and Future Perspectives

4.1 Conclusions

This thesis is primarily focused on the optimization and investigation of a modal coupling structure, which involves the resonance between the LSPR in mental NPs and the FP nanocavity mode in TiO_2/Au-film. The LSPR-nanocavity coupling-induced near-field distribution enhancement and homogenization as well as further structural adjustment for improved photoelectrochemical activities were investigated.

In Chapter 2, the effect of plasmon-nanocavity coupling on the near-field distribution was investigated by measuring the SERS response on the optimized SERS substrate, which consist of a monolayer of Au NPs on a nanocavity formed in TiO_2/Au-film. The SERS intensity CV molecular measured on the plasmon-nanocavity coupling ATA structures exhibited an 11-fold enhancement compared to that on the AT substrate without nanocavity, showcasing a remarkable SERS enhancement effect arising from the coupling between the LSPR of Au NPs and the cavity resonance. SERS signals of CV molecules with series of concentrations and a range of excitation laser powers on ATA and AT are measured, which shows a linear increase with the excitation power as well as the logarithm of CV concentration within a certain range. This phenomenon indicates that it is eligible for quantitative detection. Expect for the significant near-field enhancement, the spatial homogeneity of the near-field distribution under plasmon-nanocavity coherent coupling conditions has also been investigated by the SERS mapping and the FDTD and FEM simulations.

In Chapter 3, the plasmon-nanocavity strong coupling structure was further optimized by regulating the component, size, and shape of the metal NPs, used as the photoelectrode for investigating the impact of the strong coupling condition on the plasmon-induced water oxidation reaction by means of *in situ* EC-SERS

measurements. The Au-Ag alloy NPs was employed in the plasmon-nanocavity strong coupling structure because of its higher oscillator strength. The SERS intensities of ν(Au-O) and ν(Au-OH), which represent the reaction intermediates of water oxidation, were systematically examined over a wide range of electrochemical potentials. Expect for the higher SERS intensity on the AATA, the SERS signals of ν(Au-O) related to AuOOH, the intermediate of plasmon-induced water oxidation on the AATA photoelectrode exhibited a more negative onset potential compared to the AAT without cavity, indicating more efficient charge separation on the AATA structure, which facilitates the water oxidation reaction. Based on our *in situ* EC-SERS measurements, it was concluded that plasmon-induced water oxidation is facilitated by the quantum coherence effect under LSPR-nanocavity strong coupling.

4.2 Future Perspectives

Based on results obtained in this thesis, a plasmon-nanocavity coupling SERS-active structure, which holds great promise as a sensitive, reproducible, and spatially homogeneous substrate for detecting a wide range of chemicals and biomolecules, was fabricated. Moreover, the structure and performance of this plasmon-nanocavity coupling SERS-active structure were further optimized and applied to the photoelectrochemical detections for investigating the impact of plasmon-nanocavity strong coupling on the plasmon-induced water oxidation reaction. According to the mechanisms of plasmon-induced water oxidation reaction occurred on the plasmon-nanocavity coupling SERS-active structure, it has been concluded that plasmon-induced water oxidation is facilitated by the quantum coherence effect under LSPR-nanocavity strong coupling. The results of those studies provide valuable insights into the effects of the plasmon-nanocavity coupling condition on the development of efficient plasmon-induced photochemical reactions, which will certainly be of much help in advancing the renewable energy technologies.

According to the achievements of this thesis mentioned above, the future works are shown as below:

(1) The plasmon-nanocavity coupling SERS-active structure will be further improved for achieving ultra-sensitive and specific detection capabilities and developed into quantitative detection systems for trace or single-molecule substances.

(2) The strong coupling structure examined in this study exhibits remarkable potential for enhancing photocatalytic processes. Future research should focus on the development of advanced photocatalytic systems that harness the plasmon-induced charge separation for more efficient water splitting and carbon dioxide reduction. This could significantly contribute to sustainable energy solutions and environmental remediation efforts.

(3) The synthesis of tailored nanomaterials within the strong coupling framework presents an area ripe for exploration. Investigating the use of different materials, including metals and semiconductors, can lead to the creation of structures with custom-designed optical and electronic properties, opening up new avenues for diverse applications.

Abbreviations

ATA	Au NPs/TiO_2/Au-film
AT	Au NPs/TiO_2
AATA	Au-Ag alloy NPs/TiO_2/Au-film
AAT	Au-Ag alloy NPs/TiO_2
SPR	Surface plasmon resonance
SPPs	Surface plasmon polaritons
LSPR	Localized surface plasmon resonance
SERS	Surface-enhanced Raman resonance
EC-SER	Electrochemical surface-enhanced Raman resonance
PEC	Photoelectrochemical
NP	Nanoparticle
FP nanocavity	Fabry-Pérot nanocavity
EB	electron beam
IPCE	Incident photon-to-electron conversion efficiency
CV	Crystal violet (in chapter 2)
	Cyclic voltammetry curve (in chapter 3)
FDTD	Finite-difference time domain simulation
FEM	Finite element method simulation
RSD	Relative standard deviation
WE	Working electrode
CE	Counter electrode
RE	Reference electrode

Publication List

1. **X. Q. Zang**, X. Shi, T. Oshikiri, K. Ueno, Y. Sunaba, K. Sasaki, and H. Misawa, "Highly Sensitive and Spatially Homogeneous Surface-Enhanced Raman Scattering Substrate under Plasmon−Nanocavity Coupling" *J. Phys. Chem. C,* **2021**, 125, 19880−19886.
2. **X. Q. Zang**, X. Shi, Y. Suganami, Y. Liu, T. Oshikiri, and H. Misawa, "Investigation of Enhanced Water Oxidation under Plasmon−Nanocavity Strong Coupling Using In Situ Electrochemical Surface-Enhanced Raman Spectroscopy" *J. Phys. Chem. C*, **2023**, 127, 31, 15087–15095.